2-14-2014

Day-Ahead Solar Resource Prediction Method Using Weather Forecasts for Peak Shaving

Wesley Greenwood

Wesley Greenwood

Candidate

Mechacnical Engineering

Department

This thesis is approved, and it is acceptable in quality and form for publication:

Approved by the Thesis Committee:

Andrea Mammoli , Chairperson

Olga Lavrova

Francesco Sorrentino

Day-Ahead Solar Resource Prediction Method Using Weather Forecasts for Peak Shaving

by

Wesley Greenwood

B.S., Mechanical Engineering, University of New Mexico, 2011

THESIS

Submitted in Partial Fulfillment of the
Requirements for the Degree of

Master of Science
Mechanical Engineering

The University of New Mexico

Albuquerque, New Mexico

December, 2013

Dedication

I dedicate the time and work devoted to the research presented in this thesis to my parents and sister. Their patience and support make the hard work bearable and the celebrations shared.

Acknowledgments

I would like to extend a special thanks to my professors, colleagues and friends Dr. Andrea Mammoli, Dr. Olga Lavrova, Brian Arrellano, Steve Willard and Feng Cheng. They all taught and guided me throughout my experience with the Prosperity Energy Storage Project of which I was lucky to be a part. The friends and knowledge I gained were well worth the hard work.

Day-Ahead Solar Resource Prediction Method Using Weather Forecasts for Peak Shaving

by

Wesley Greenwood

B.S., Mechanical Engineering, University of New Mexico, 2011

M.S., Mechanical Engineering, University of New Mexico, 2013

Abstract

Due to recent concerns about energy sustainability, solar power is becoming more prevalent in distributed power generation. There are still obstacles which need to be addressed before solar power can be provided at the level of reliability that utilities require. Some of these issues can be mitigated with strategic use of energy storage. In the case of load shifting, energy storage can be used to supply solar energy during a time of day when utility customer's demand is highest, thus providing partial peak load burden relief or peak shaving. Because solar resource availability is intermittent due to clouds and other atmospheric factors, charge/discharge planning must take weather into consideration. Many inter-day and intra-day solar resource prediction methods have been developed to aid in firm (high-reliability) resource establishment and peak-shaving through various methods and data sources with different levels of complexity. The purpose of this study was to investigate the use of readily-available, day-ahead National Weather Service (NWS) forecasts to develop a PV resource prediction. Using past day-ahead NWS weather forecasts and historical

performance data from the Prosperity Energy Storage Project near Mesa del Sol in Albuquerque, New Mexico, several correlations were created based on regression analysis and optimized for minimal Root Mean Square (RMS) error for daily insolation prediction. Though some other methods such as the National Digital Forecast Database (NDFD) and Global Forecast System (GFS) exhibit greater accuracy, this method could prove to be a relatively simple means of planning the use of energy storage for peak-shaving or arbitrage. Additionally, given appropriate considerations for prediction uncertainty one could establish a firm resource to meet customer demand.

Contents

List of Figures

List of Figures

List of Tables

List of Tables

Chapter 1

Introduction

As concerns for finite-supply fossil fuels and greenhouse gas emissions grow, renewable energy is becoming an increasingly important resource for distributed energy which is commercial and residential electricity from its source located in proximity to the customer. However, before renewables can gain acceptance and be used to their potential, technology must be mature enough to provide the affordable, firm resource that utility companies demand. Here, the term "firm" stems from firm demand (utility customer electricity need) which is "the portion of demand [electricity] that a power supplier is obligated to provide" and firm transmission service which is "the highest quality (priority) service offered to customers under a filed rate schedule that anticipates no planned interruption" [1]. A firm resource is, therefore, a power source whether it is fossil fuel or solar that is required to fulfil utility obligations and is available at all times needed without interruption. To utility companies, violating these obligations means serious repercussions such as fines.

1.1 Motivation and Project Background

The need to mitigate the problems caused by increased penetration of renewables in distributed energy provided the motivation for the Prosperity Energy Storage Project (shown in figure 1.1) near Mesa del Sol in Albuquerque, NM which provided the resources to perform the work presented in this thesis. This project is funded in part by the U.S. Depart of Energy through the American Recovery and Reinvestment Act (ARRA) along with several utility companies from around the world to research many concerns for utility-scale PV energy production with energy storage.

Figure 1.1: Prosperity Energy Storage Project site and battery energy storage equipment.

Having gone on-line in September 2011, it has 500 kW of power generation and 1 MWh of energy storage. Additionally, the storage has 500 kW of response providing the goal capability to perform simultaneous smoothing and shifting, the latter of which is the focus of the study described in this paper. All performance data are measured and recorded using a supervisory control and data acquisition (SCADA) system allowing data analysis. The objective of the several analyses conducted by the participants of the project is to research and document optimal operating practices to provide reliable, quality power.

The originators of this project recognized the need to investigate the challenges for the changing electricity transmission system. Figure 1.2 shows how the existing electricity grid is organized. Centralized power generation such as nuclear and fossil fuel pants are typically located removed from urban areas where the bulk of population, and therefore electricity demand, exists. The power is then sent at high voltage to substations and finally feeders located closer in proximity to the customer.

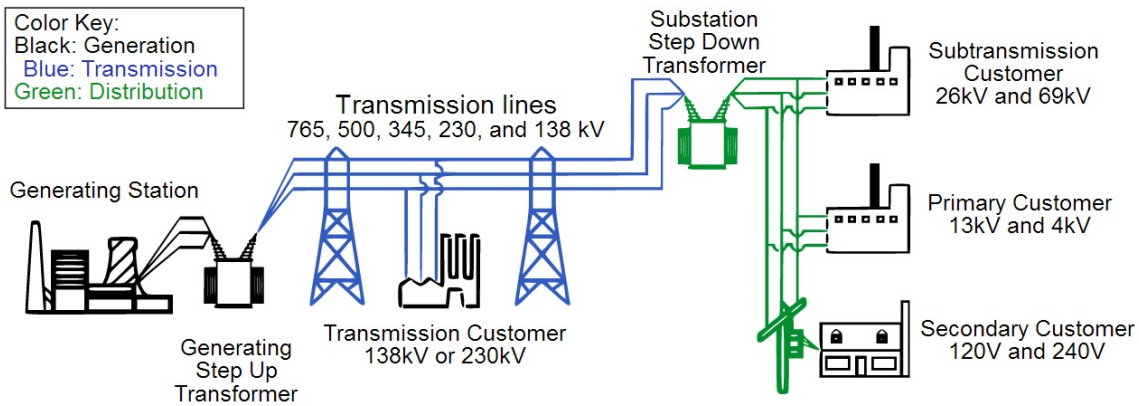

Figure 1.2: Current electricity distribution schematic showing separation of generation and customer [2].

The future electricity grid, however, will have increased local generation from renewables such as wind and solar as shown in figure 1.3. Note that even though wind generation is unlikely in urban areas, it represents the possibility for many

forms of distributed generation. Renewable resources, in particular, are variable depending on the presence of wind, solar radiation and so on. This irregular power availability and quality is cause for concern for both centralized power generation and local utility companies who manage transmission.

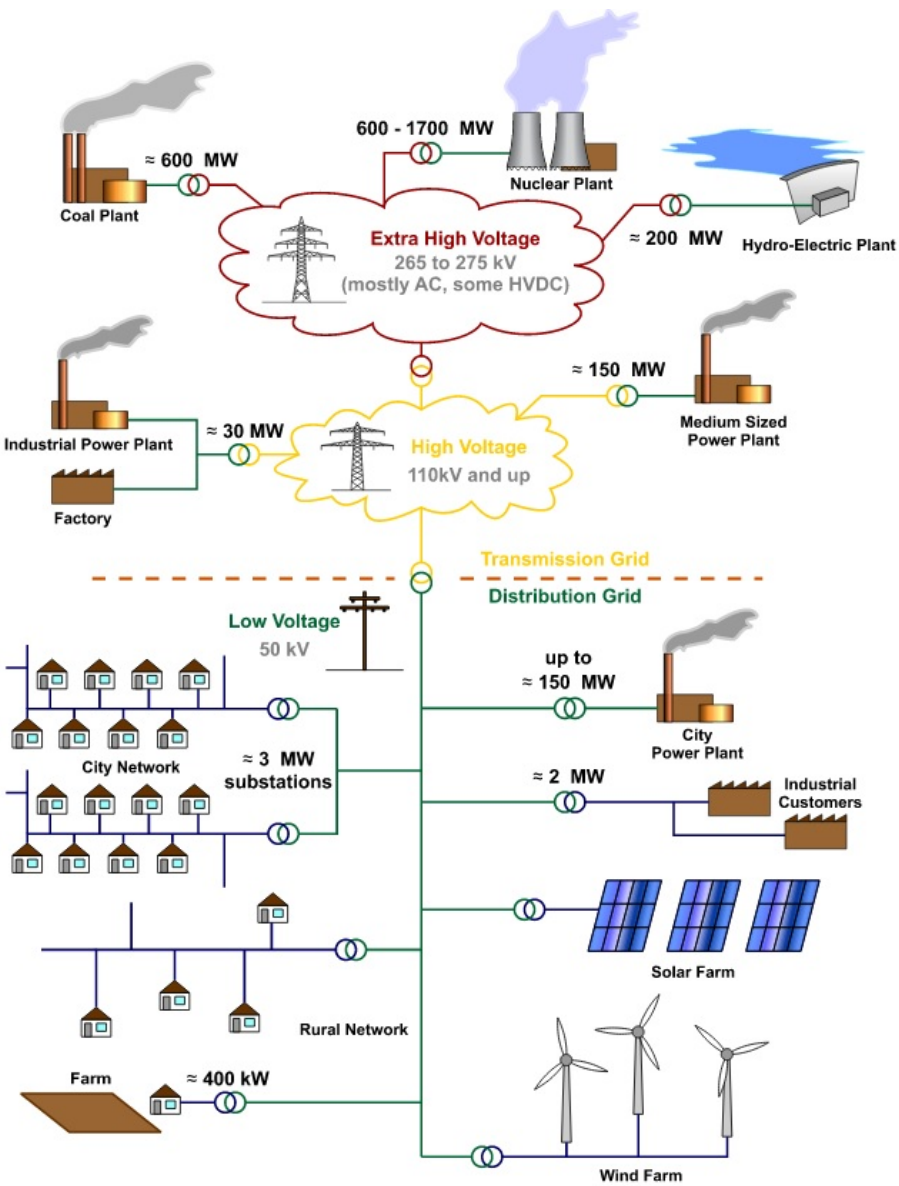

Figure 1.3: Future electricity distribution schematic showing various means of local electricity generation [3].

1.2 Peak Shaving

One way of fulfilling firm power obligations is peak shaving, which is the concept of utilizing local generation or energy storage to relieve peak-load burden on the electrical utility. Peak shaving provides relief by meeting customer demand which prevents a local feeder from overloading. This makes electricity distribution more reliable by reducing wear on equipment and preventing the feeder from tripping due to overload. This is also related to load levelling which means keeping the customer-required power availability profile as flat as possible to resemble base load operation conditions. The concepts of load levelling and peak shaving are illustrated in figure 1.4.

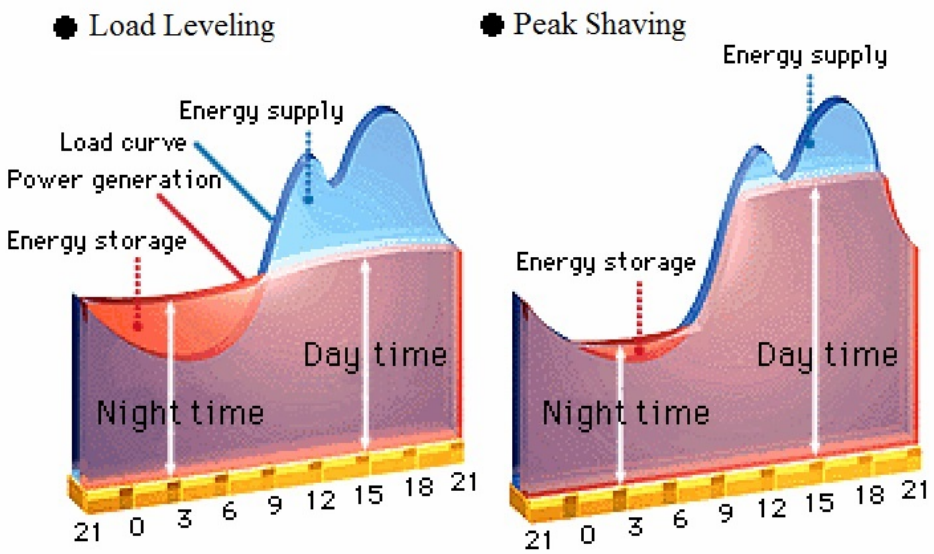

Figure 1.4: Illustration depicting concept of load levelling and peak shaving; Note attempt to match resource to customer need [4].

Base load is typically a constant, firm power supply from a source such as nuclear or coal plants which provide a steady supply of electricity at all times. This sort of power is highly valued by utilities for its surety of availability and economic operation

which produces significant capitol for relatively low fuel cost. Alternatively, should a sudden rise in demand occur, fast-response resources such as gas turbines are called upon which add cost. Base load is also usually the cheapest form of energy/power. However, base load resources can only operate at constant power.

Peak shaving can be planned for, but complexity is added because both customer load profiles and renewable resources vary from day to day. Load profiles on a distribution feeder for typical hot weather and cold weather conditions are shown in figure 1.5.

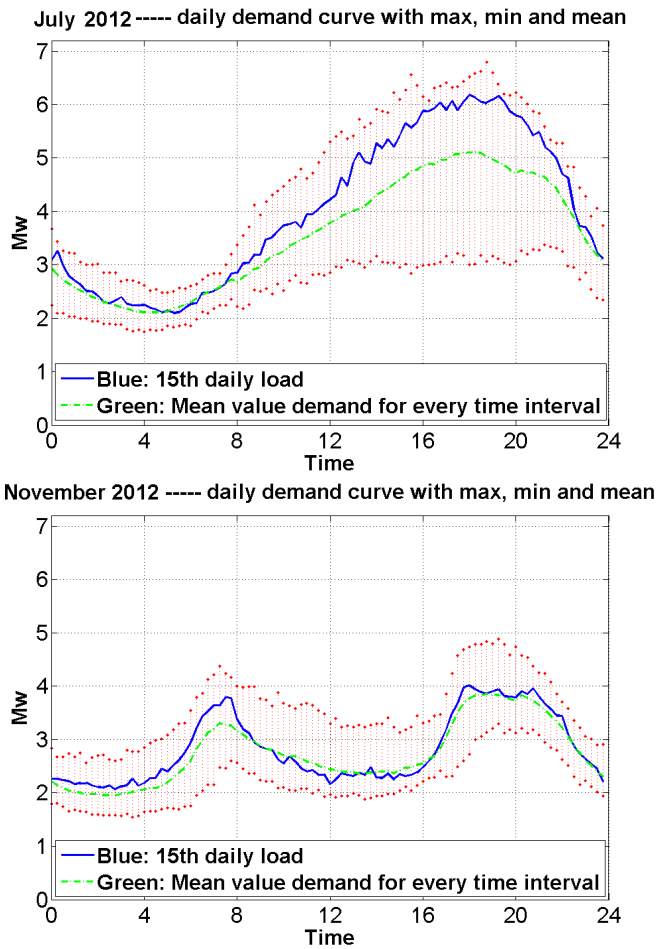

Figure 1.5: Varying electricity demand profiles for different months of the year showing different peak demand times of day due to factors such as air conditioning in summer months.

Similarly, figure 1.6 shows two types of load profiles alongside clear and cloudy day irradiance profiles. To shift the temporally mismatched renewable resources to satisfy utility customer load profiles, predictions must be made for future load and resource.

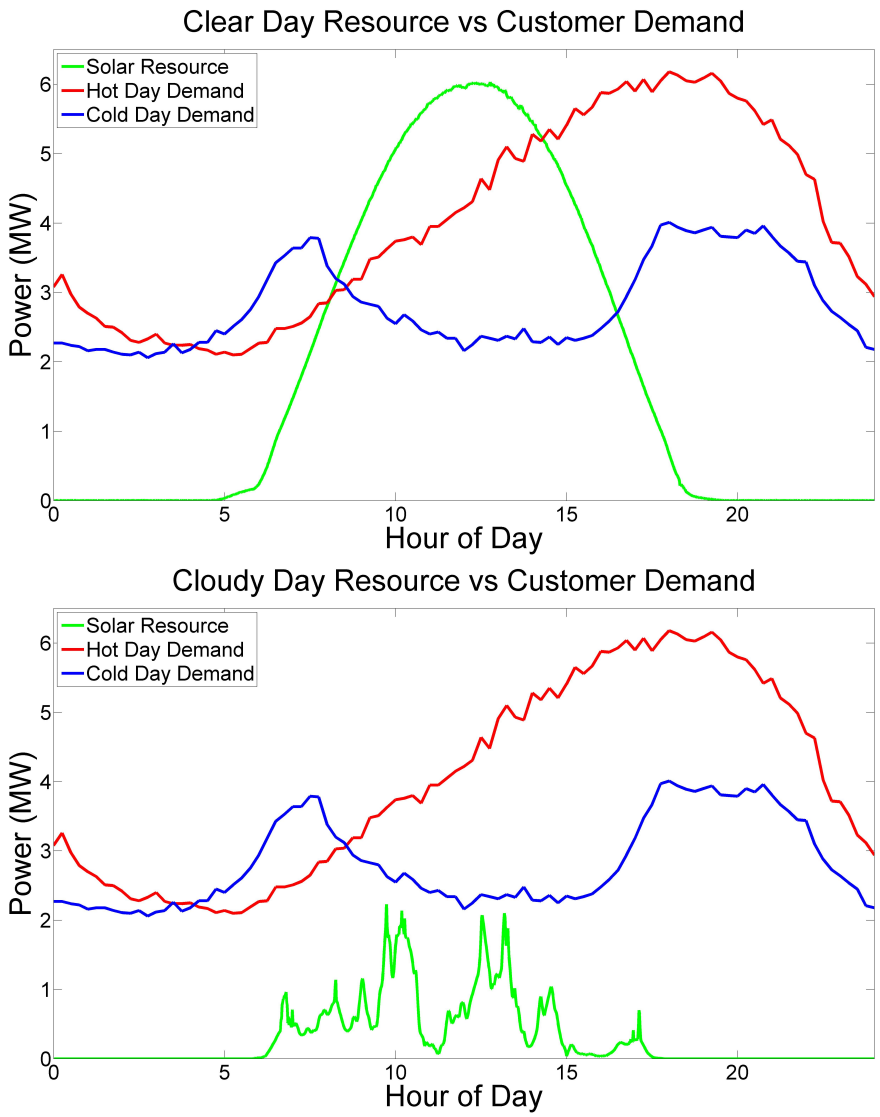

Figure 1.6: Example of solar resource alongside customer demand profiles showing temporal mismatch; also depicts effects of cloud-driven variability.

1.3 Energy Storage

There are various options for energy storage in an electric power system. Selecting an option requires consideration of the end use, the cost, reliability etc.. Technologically feasible options are:

- Battery energy storage (BESS)
- Thermal storage (TES)
- Compressed air (CAES)
- Flywheels
- Capacitors & ultra-capacitors
- Pumped hydro energy storage (PHES)
- Hydrogen production

Energy density and cost varies greatly between these options. For example, the range of energy storage capacities and power outputs are plotted against each other in figure 1.7. For a peak shaving application, one would look for an option to the right of the diagonal dotted line representing one hour of dispatchable power. Appropriate sizing would depend on the amount of energy and power level needed for peak shaving.

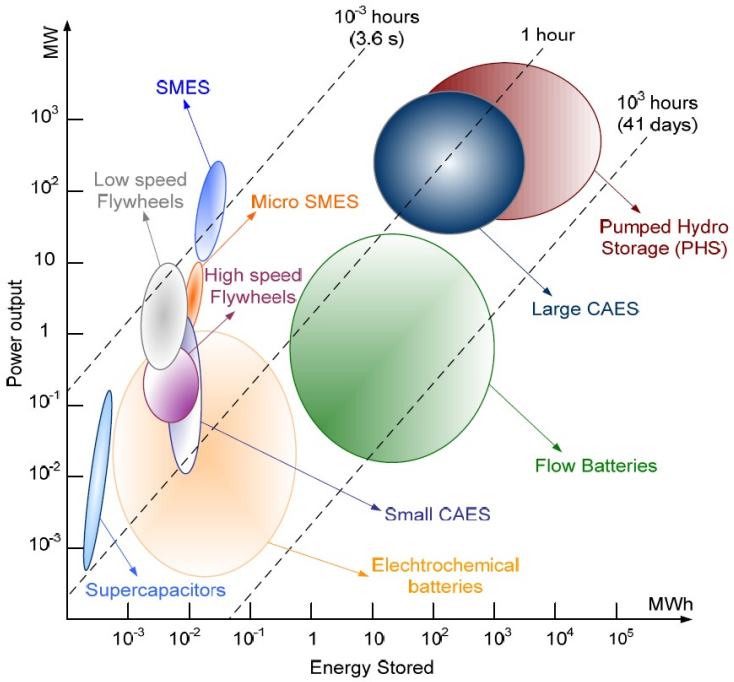

Figure 1.7: Power output and energy storage capacity characteristics of various energy storage options [5]. Large circles show high scalability.

Battery Energy Storage

In the case of the Prosperity Energy Storage Project, advanced lead acid batteries were chosen to provide the goal 1 MWh at 250 kW for 4 hours of peak shaving [6]. In combination with PV generation, battery energy storage can be useful not only for peak shaving but for smoothing [7]. This topic will be covered later in the "Intermittency/Variability" section of this thesis. Additionally, lead-acid batteries are a mature technology, and in terms of cost per performance they are inexpensive relative to other forms of storage as shown in figure 1.8.

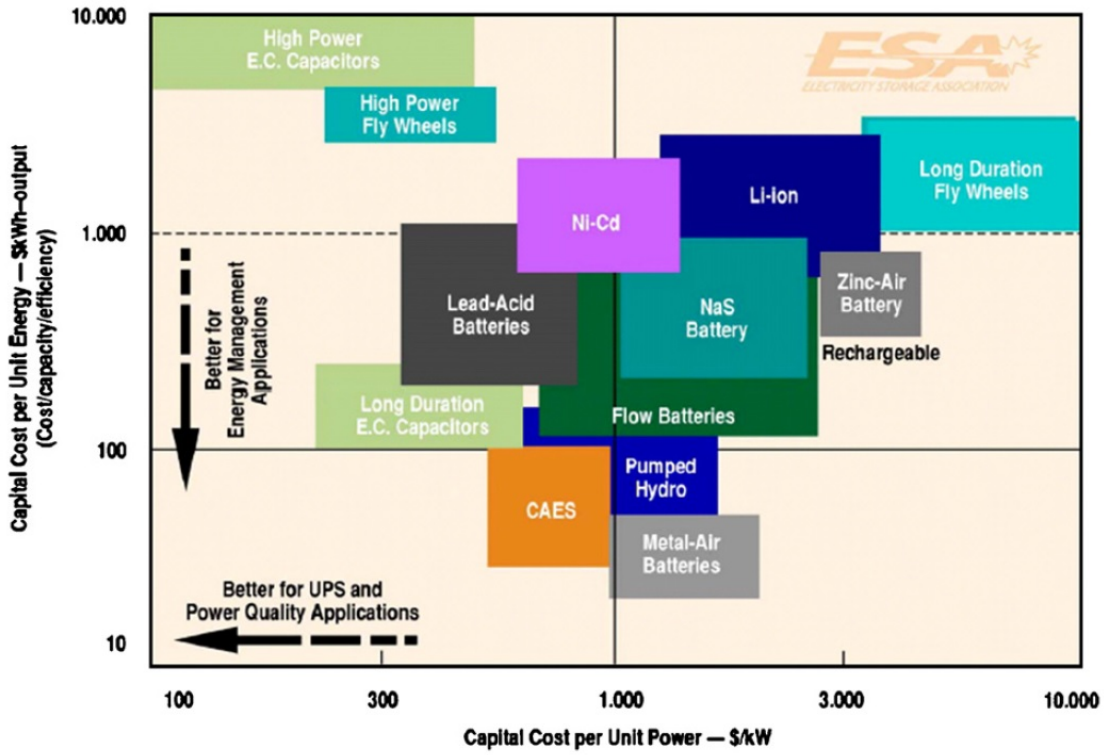

Figure 1.8: Cost per unit power versus cost per unit energy capacity for various energy storage options [8].

Batteries also have the added benefit of being scalable. Some energy storage technologies, such as pumped hydro, have a degree of minimum investment before they are economically feasible. Battery storage, however, can be designed with the appropriate number of units to obtain the desired capacity making them applicable for residential and utility-scale generation.

Another type of battery storage which was originally considered for the Prosperity Energy Storage Project was a flow battery system. These systems function by passing oppositely charged electrolyte fluids through a fuel cell to create an electrical charge. The technology has many advantages including high scalability to large systems, full discharge/recharge without degradation, decreasing cost per unit energy storage

capacity with increased size,relatively high round-trip efficiency (80-90% for larger systems). The only limiting factor on storage capacity is the electrolyte storage tanks, but the energy density is fairly low (35-50 Wh/kg for 2nd generation electrolytes) and presents challenges for storage space.

Several other batteries exist with varying advantages. For example, lithium ion batteries have a much higher energy density compared to lead acid and are generally much lighter making them attractive for electric vehicles. Unfortunately, due to battery chemistry lithium ion batteries have a short shelf life and capacity decays between 6%-40% in the first year regardless of charge/discharge cycles. When considering battery energy storage for a particular application it is important to know which characteristics best fit generation and other needs.

Thermal (TES)

With heating, ventilation and air-conditioning (HVAC) accounting for about 40-50% of the primary energy budget, thermal energy storage provides an excellent means of offsetting peak load. Particularly where thermal energy would otherwise not be utilized or disposed of in cooling towers, certain thermal energy storage applications can provide up to 90% of heating and 33-43% of cooling requirements as found for the University of New Mexico (UNM) solar-assisted HVAC system [9]. Though the resource prediction method reviewed in this paper focuses on PV electric energy, it could potentially be integrated with solar thermal as in the case with UNM or for thermal storage using an electric chiller for cold energy storage. One thing to remember when considering thermal energy storage is that it is uni-directional. This means it can discharged when determined by the user but will charge only when renewable resource is available. It is also limited to thermal energy and cannot provide electricity without secondary processes.

Compressed Air (CAES)

Compressed air energy storage (CAES) involves using off-peak or excess grid power to compress air in a containment vessel (typically an underground cavern) and then using the pressure to drive a turbine during peak hours [10]. Particularly with the use of geologic formations such as salt caverns, CAES is one of the more economically feasible energy storage technologies. Examples of different means of producing the underground storage cavity for CAES are shown in figure 1.9.

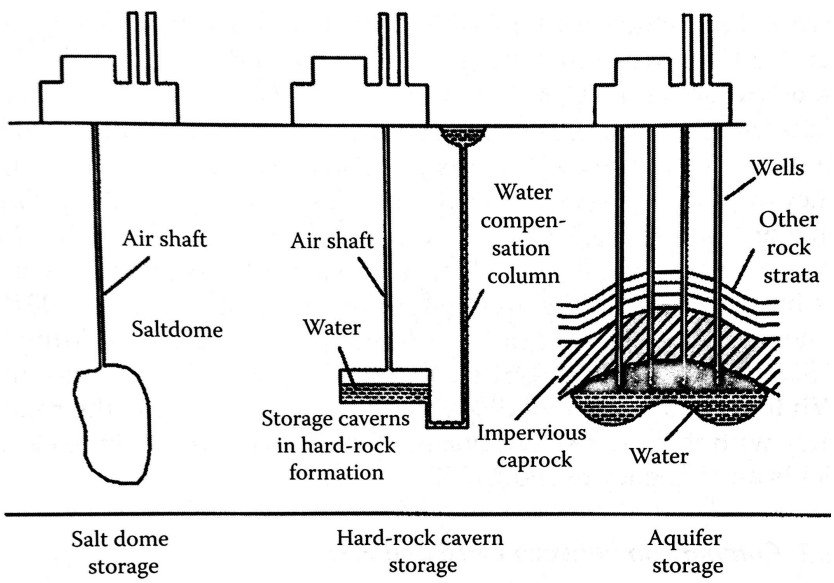

Figure 1.9: Examples of underground storage cavities for CAES [11].

Design and applications of CAES systems offer considerable flexibility in terms of size and location. Depending on design, a CAES plant can be used to optimally provide either smoothing or peak shaving support as shown in figure 1.7. Round trip energy storage efficiency is also fair. In certain applications of CAES such as with a hybrid generation/storage system using a natural gas turbine, round trip efficiency is about 88% [11].

Flywheels

Flywheels are a way of storing mechanical kinetic energy in a spinning cylindrical mass and have long been used for short term energy storage. Modern designs use magnetically levitated bearings which significantly reduce bearing wear providing a longer system life and increased storage efficiency [11]. They can also be kept in a vacuum which removes air drag further increasing efficiency.

Flywheels have many advantages including relatively low maintenance and long life span of about 20 years. Because flywheels unavoidably dissipate energy with time, they are purely for short term energy storage, but as can be seen in figure 1.7 they have the ability to provide quick bursts of power. One facility in Culham, Oxfordshire in the United Kingdom has a large system, shown in figure 1.10, capable of providing short bursts of power up to 0.4 GW [12].

Figure 1.10: 1 MWh storage capacity flywheel in Culham, UK [13].

This low-speed, high-mass flywheel in Culham has a fairly low energy density of 1 Wh/kg, but high-speed flywheels made from composites such as carbon fiber can have energy densities up to 100 Wh/kg [12].

Ultra-capacitors

Ultra-capacitors (or super-capacitors) are used to store small amounts of energy for quick charge and discharge for smoothing output voltage variations. These devices must be capable of many cycles and usually need to charge at the same rate as they can discharge which is in contrast to conventional lead-acid batteries which must charge roughly five times slower [12]. These devices have been used for utility power smoothing which is not the primary interest of this paper, but they do have potential for shifting. When used in tandem with conventional long-term battery energy storage, they can be used to relieve peak power needs. They are also ideal for voltage regulation in vehicles and are favored for regenerative braking [11, 12].

Pumped Hydro

Energy can also be stored as gravitational potential energy in an elevated mass. Pumped hydroelectric energy storage (PHES) is a mature technology with early examples in Switzerland and Italy from the 1890's. During times of excess power, water is pumped to an elevated reservoir for storage. When power is needed for peak shaving or otherwise the water is then allowed to flow down through a turbine to generate electricity or to simply generate mechanical work. A diagram of an existing PHES facility is shown in figure 1.11. With current turbine technology, PHES can have an 80%-85% round-trip efficiency [11].

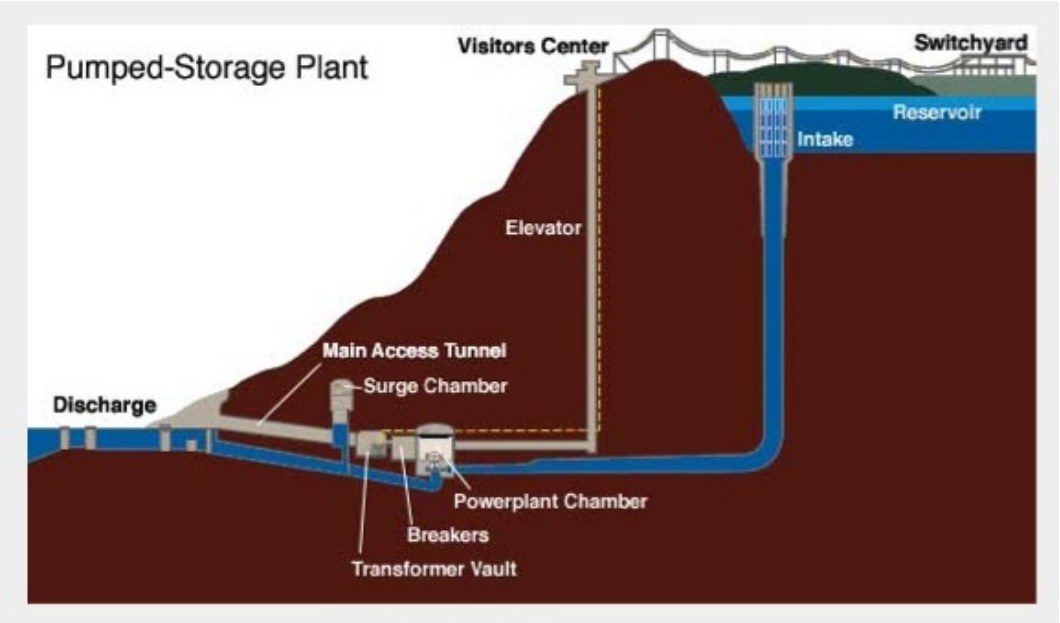

Figure 1.11: Diagram of pumped hydroelectric energy storage at Raccoon Mountain [14].

An added benefit of PHES is that it is scalable and applicable wherever water resource is not in short supply. In one study, PHES is implemented for a stand-alone PV system in a remote village in Greece as a sole electricity source [15]. This provided more reliable power production for remote areas where grid expansion was either technically or economically not feasible.

Another advantage is that a pump works on electricity regardless of source so PHES can be applied to other means of variable power generation such as wind. Using a model, it has been shown that combining PHES with wind power generation can provide firm power [16]. Figure 1.12 shows the modelled summed outputs of wind and PHES sources in a system in Oaxaca, Mexico forming firm power.

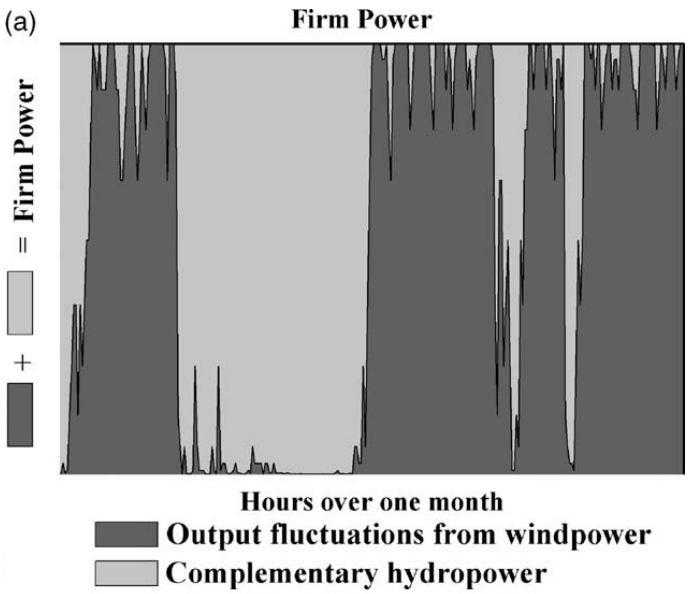

Figure 1.12: Firm power as sum of wind power and PHES for one month [16].

Furthermore, PHES has been applied to existing wind power systems, like in Denmark. A particular Danish wind farm sells much of its generated power to neighboring countries, some of which have hydroelectric power. These countries can reduce their hydroelectric resource consumption to take advantage of the available wind power allowing them to use and sell their PHES electricity back to the Danes at a higher profit during periods of low wind and high demand [12].

Hydrogen Production

One challenge for energy storage is its application for transportation. With increasing fossil fuel costs and ever decreasing limited resource, hydrogen is often proposed as a potential replacement combustion fuel source. Hydrogen can be produced using a few different methods with varying economic efficiency, but the greatest limitation for hydrogen for transportation is storage. Gaseous hydrogen has a low specific density so it must be either compressed or cryogenically liquefied for practical transportation,

though liquefying hydrogen introduces safety concerns making it impractical [11]. Hydrogen energy storage can also be useful for electric vehicle because hydrogen is needed for fuel cells.

1.4 Intermittency/Variability

Many of the challenges facing the advancement of renewable energy technologies stem from the fact that, with very few exceptions, renewable resources are inconsistent. For example, wind fluctuates with weather patterns, solar power is interrupted by clouds and other atmospheric conditions, bio-fuels can change depending upon crop yield and so on. Solar power, specifically, is affected by varying frequencies of intermittency. Figure 1.13 shows the potential periodic irradiance fluctuation and some suggested means of mitigating the intermittency.

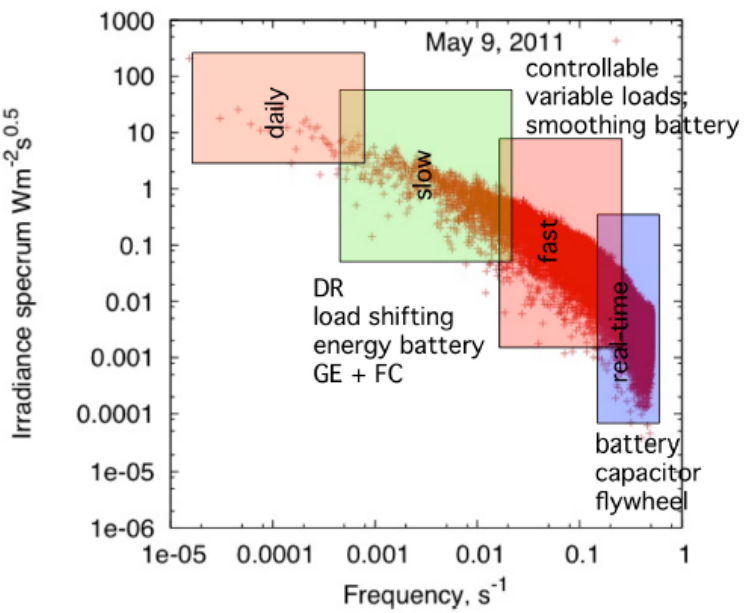

Figure 1.13: Frequency characteristics of solar radiation for a cloudy day causing intermittency.

High-frequency Intermittency

The high frequency portion of the plot (labelled "real-time") depicts the nearly instantaneous changes in power output which can cause instability on the power grid. Current research is investigating the use of on-site storage like the fast-response ultra-capacitor batteries at Prosperity to "smooth" the intermittent output due to scattered clouds [7]. Other means of power smoothing include technologies which appear high in power output in figure 1.7 and preferably lower in capital cost per unit power in figure 1.8. To utilize storage for smoothing, one typically applies some sort of real-time control [17]. An example of control involves using historical power data with severe power fluctuations, and possibly a short-term prediction, to form a desired (smoother) power output profile. The electric storage can then be commanded to charge or dispatch accordingly to output improved power quality onto the grid.

The amount that high frequency intermittency affects grid power is highly dependant on array size and dispersion of local PV power production within communities [18]. High frequency variability tends to affect smaller arrays more than large ones because large utility-scale arrays cover more area causing the ramp to be smoothed. However, many dispersed small PV systems are less variable than a large PV system due to the overall larger footprint for the dispersed systems.

Low-frequency Intermittency

The low frequency portion of the plot (hours to a day) represents the resource variability solved by load shifting. Day-ahead weather forecasts have the potential for predicting these sorts of fluctuations. There is also fluctuation in demand from day to day. As stated before, load can be anticipated, but there is always the possibility for severe and rare surges in demand which the utility must accommodate.

The performance of the methods discussed in this paper is optimized for the data to which it was calibrated. However, it is important to understand that solar resource is also variable form year to year and month to month. This level of variability lies further left in figure 1.13. In figure 1.14, the inter-annual coefficient of variance (COV) for each month in the continental United States shows how a region's monthly resource can vary from one year to the next [19]. The COV, also known as the relative standard deviation, expresses the likelihood of data falling within the resulting value range around the mean. These results give one a means of understanding how potential PV array energy production might vary as well as the accuracy of any day-ahead resource forecast.

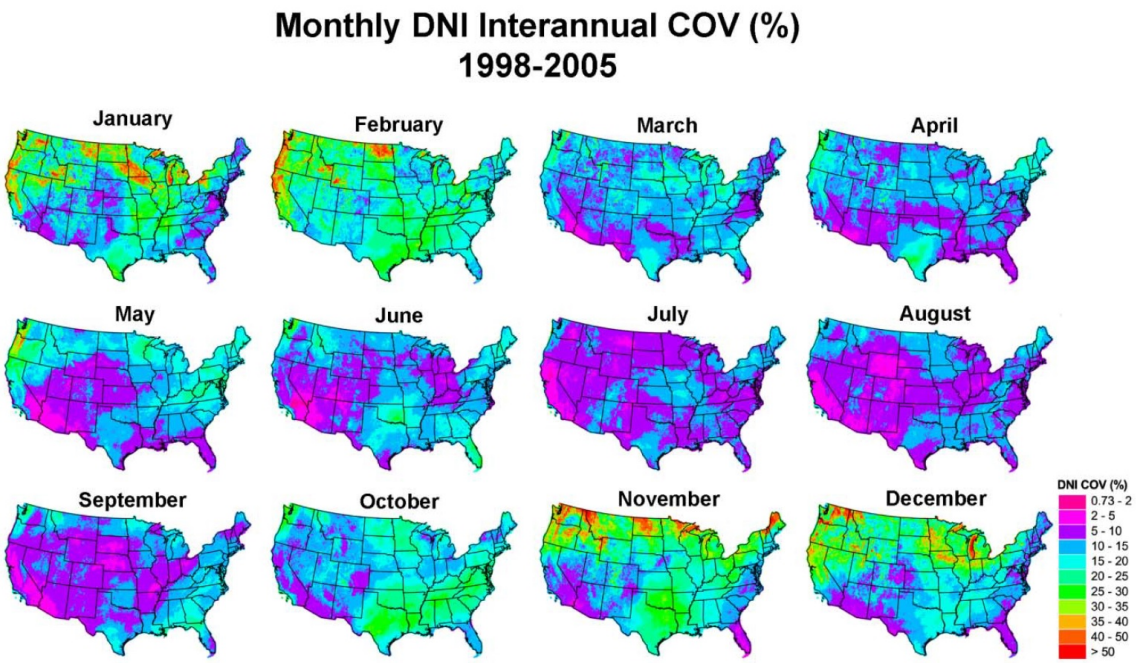

Figure 1.14: Monthly DNI inter-annual COV continental US showing year-to-year variation of solar radiation [19].

1.5 Sample Methods

Because firming and peak shaving have been challenges in renewable energy for quite some time, several methods exist for predicting resources so there can be planning for storage. For day-ahead solar resource prediction, input data must in some way characterize the clouds which may obstruct the sun from the solar array. These data can include weather forecasts, satellite imagery, or solely a site's historical resource data. Figure 1.15 shows the temporal and spatial applicability of numerical weather prediction for irradiance forecasting *(Note: STPP = Solar thermal Power Plant)* [20].

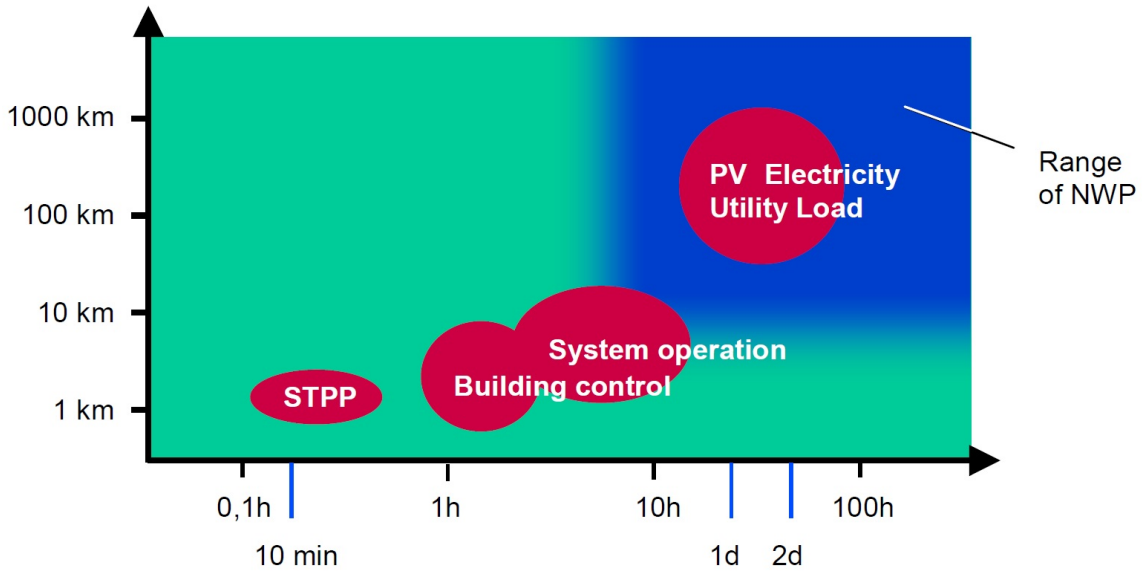

Figure 1.15: Temporal and Spatial requirements for applications of irradiance forecasts utilizing numerical weather prediction; indicates application is limited to load shifting/planning [20].

Regression Models

Regression models seek correlations between dependent variables and independent variables based on an underlying function or curve fit. By defining a fitting relation,

one typically estimates a least squares error (or other error metric) to determine prediction performance [21]. This method has been attractive for forecasting, but it can yield false performance results or "illusion of predictability" if introducing too many degrees of freedom or unrelated data [22, 23]. In other words, one could find a correlation between any two or more sets of data without any true connection existing leading to unrepeatable results.

One of the earliest attempts at irradiance prediction used model output statistics (MOS) [24] to create regression models between irradiance measurements and weather forecasts available at the time for predictions one to two days in advance [25]. In the years after this early work, little advancement was done in irradiance forecasting and similar variations presented little to no new value [26].

More recently, a prediction method has been developed and has undergone preliminary testing using the NWS's National Digital Forecast Database (NDFD) [27]. The NDFD is a new tool in which local and regional NWS offices collaborate to collect weather forecast data at a spatial resolution of 0.05° latitude and longitude in the United States. This method closely resembles the ones presented in this paper with the exception that this study's methods develop optimized coefficients and incorporate multiple forecast parameters.

Other Input Variables

Cloud cover is just one of many atmospheric conditions which may impede radiation from the Earth's surface. Water vapor, aerosols, ozone fluctuations and other atmospheric constituents affect irradiance as well. Clouds obstruct far more irradiance than these effects, but there have been methods which include these parameters to improve clear-condition resource prediction. This would benefit concentrating solar power plants which require direct irradiance unlike PV power which can utilize

diffuse irradiance scattered by particles in the atmosphere.

The AFSOL (Aerosol-based Forecasts of Solar Irradiance for Energy Applications) method included these parameters along with ground albedo measurements and found a reduction in DNI relative root mean square error (rRMSE) from 31% to 19% versus a published method using solely NWP inputs [28]. The method did not perform as well as *Meteostat-7* which is a satellite-derived terrestrial irradiance prediction method.

Cloud Vectoring

Another way of predicting future radiation resource involves using time series images of the sky to project cloud motion. A predicted cloud path can then be used to develop an estimation of radiation anticipated. Recent studies have shown this technique to be applicable to short term irradiance prediction for use with power quality regulation to mitigate ramps. Recently, the University of California San Diego has developed custom ground imagery devices to obtain sequential sky images along with a "clear sky library" to estimate future irradiance changes based on cloud characteristics [50]. Cloud vectoring is also capable of day-ahead resource prediction as with the *Solar Anywhere* prediction. *Solar Anywhere* is a commercial product offering coarse historical radiation data and sells increased spatial resolution historical and predicted data. Its predictions are based upon cloud motion derived from time-series images taken from geostationary satellites [32].

Artificial Neural Networks (ANN)

Artificial neural networks (ANN) are a means of developing predictions by using self-learning computer software to recognize patterns in training data consisting of available inputs and known outputs. ANN's have the advantage of being capable of

coping with noisy and incomplete data or non-linear problems. ANN's are considered to have more potential for renewable energy resource forecasting than clearness index correlations [29, 30].

One method utilized available weather forecasts as inputs and recorded daily insolation, precipitation and minimum and maximum temperature as outputs for training to develop a daily radiation prediction [31]. This method, developed for four sites in south-eastern United States, experienced daily insolation RMSE values ranging from 0.81 to 1.01 kWh/m^2 (total summer clear day insolation in Albuquerque is approximately 8 kWh/m^2). It is also claimed that the method could be used to estimate radiation when only temperature and precipitation measurements are available allowing one to save the added cost of irradiance sensors and data acquisition.

Persistence

The simplest means of resource forecasting is a persistence forecast. This method assumes that the next day's resource will closely resemble the current day's resource and therefore says it will be the same. A persistence forecast can serve as a benchmark for evaluating other forecasts but is highly dependant on location and climate [32]. Table 1.1 shows persistence in comparison to the *Solar Anywhere* forecast developed by *Clean Power Research* [33].

Table 1.1: Annual RMSE (W/m^2) for *Solar Anywhere* satellite-based irradiance prediction versus persistence method [32].

Desert Rock, NV		Boulder, CO		Goodwin Creek, MS	
Forecast	Persistence	Forecast	Persistence	Forecast	Persistence
139	122	189	187	164	191

One could draw the basic conclusion from these numbers that either persistence performs better in drier climates such as Nevada than wetter ones like Mississippi

or that the forecast performs best in wetter climates. However, looking back at figure 1.14, it is likely the region's temporal variability is affecting the consistency of day-to-day weather and making persistence vary in performance.

1.6 Clear Sky Irradiance Models

In many cases, it is necessary to model solar radiation numerically. This is not to be confused with producing historical radiation data based on historical data for other characteristics such as satellite and ground-based sky imagery [34]. In this sense, irradiance modelling means the creating a clear-sky irradiance data set for a site based on known behavior of solar geometry.

For a regression model solar resource prediction method, theoretical clear-sky irradiance data is necessary to establish a baseline from which a clear-sky index can be subtracted. Clear-sky irradiance is specific to each site's location, orientation and installed equipment (e.g. fixed versus tracking arrays) and can be calculated using a number of different methods.

Solar Geometry

Clear-sky irradiance data at any temporal resolution can be found, perhaps most simply, using well-known algebraic equations defining the moving geometry of the sun with respect to the Earth. Many texts define these relationships along with expressions defining the contributions of secondary effects, such as diffuse irradiance, air mass attenuation and local to solar time adjustments based on location with respect to the local time zone's standard meridian [35]. Because this method of creating clear-sky irradiance data provides the opportunity to learn valuable fundamentals in understanding solar resources, it was selected for this study. The theory behind this

method will be covered in further detail later in this paper in Chapter 2: Clear-Sky Irradiance Model.

Bird Clear Sky Model

There are some resources available on-line to easily calculate clear-sky direct and diffuse insolation data using these relationships as well. The Bird Clear Sky Model is shown to yield results within ± 10% of radiative transfer codes [34, 36]. This model, with few changes, provides the basis for clear-sky data for METSTAT Solar Model (Meteorological-Statistical) which, in turn, is used in NREL's National Solar Radiation Database (NSRDB) to provide hourly solar radiation data [37]. NREL also offers a free spreadsheet using the Bird Model and user-defined inputs to provide the year's hourly clear-sky insolation values for easy calculation and data export [38].

Refinements & Turbidity

Other clear sky models have been introduced with refinements to particular aspects either in order to reduce the complexity of calculation or to aid in the determination of new outputs in addition to irradiance. In particular, recent efforts have been made to improve upon defining turbidity which is the quantification of cloudiness or haziness in a fluid (in this case the Earth's atmosphere). Turbidity is the factor which determines the amount of attenuation within the atmosphere due to aerosols, water vapor and other atmospheric constituents.

Since its publication in 1922, the Linke turbidity coefficient has been widely used in solar radiation applications, but has the disadvantage of being highly dependant on air mass. Over the course of a day, the sun's radiation passes through varying thickness of atmosphere from a minimum at solar noon to a maximum when the sun is at the horizon. Ineichen and Perez [39] sought to eliminate this disadvantage

by introducing two altitude dependant coefficients to the formulation of the Linke turbidity coefficient. Figure 1.16 shows the global clear sky index versus air mass for an existing method on the left next to the same method with a reformulated turbidity coefficient on the right. Note that the decrease in clear sky index at high air mass values disappears indicating the removal of air mass dependence.

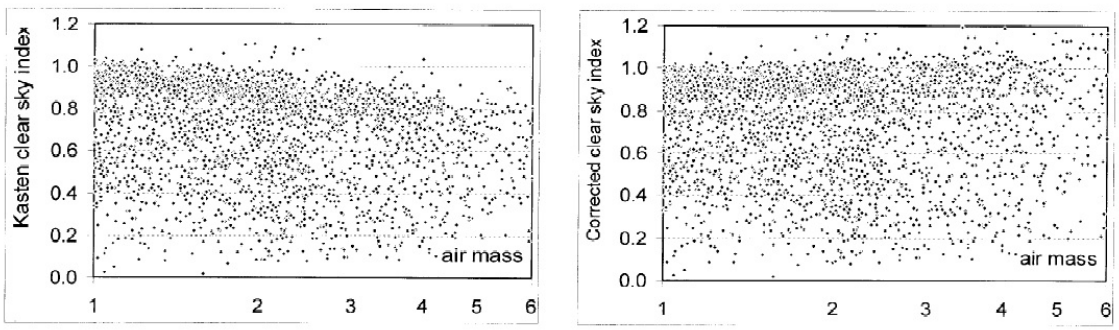

Figure 1.16: Global clear sky index versus air mass. Note decrease in left plot with increased air mass [39].

Attenuation can be an important factor to consider particularly for PV where diffuse irradiance can produce useful energy. These and other refinements, however, seek to improve upon the accuracy by relatively small amounts and are most significantly found at times near sunrise and sundown when the air mass is highest. For the purposes of this study, though attenuation was accounted for, more advanced methods were not used in favor of simpler ones.

1.7 PV Measurements/Uncertainty

Accurate measurements are necessary to collect actual resource data so prediction methods can be evaluated. Additionally, sites can be assessed economically for potential array installation. Measurement alone has many challenges depending on

application such as instrumentation, maintenance, correlation to solar power generation performance and data recording.

1.7.1 Instruments

Instruments which are designed to measure any form of solar radiation are known as radiometers, the two most common of which are pyranometers and pyrheliometers. Each work on different mechanisms and can be applied flexibly to obtain measurements for global horizontal irradiance (GHI), direct normal irradiance (DNI), diffuse horizontal irradiance (DHI) or plane of array (POA) irradiance of either the entire or select band of incident solar spectrum [40].

Thermoelectric Sensors

Black and white, or thermoelectric, pyranometers work by translating a difference in temperature experienced by a disc of alternating black and white colored wedges as seen in figure 1.17 into an irradiance value. The temperatures are measured with thermocouples which produce a corresponding voltage allowing irradiance calculation. Because the temperatures of the wedges are dependant on all wavelengths, this measurement covers the entire solar spectrum [40]. This also requires that black (i.e. the coating) is black at all wavelengths and similarly with white. One should note that this sort of device has a degree of thermal inertia. This causes lost visibility of quick changes in solar flux at smaller sampling rates because the wedges require longer sustained radiation changes to change temperature [34]. Though this may be acceptable for some types of analysis, it would not be appropriate for calculating or mitigating instantaneous ramp rates.

Figure 1.17: Black and White Pyranometer; thermoelectric type sensor [41].

Similarly, pyrheliometers also function using a thermoelectric detector but measure strictly DNI. This is done by shielding the sensor with a long, narrow tube and keeping it in-line with the sun throughout the day. This requires automated tracking to maintain alignment with the relatively small $5.7° - 6.0°$ aperture angle. An equipment diagram for a sample pyrheliometer is shown in figure 1.18. These measurements are of particular value to applications requiring only direct normal irradiance such as concentrating solar [34]. Though this device also experiences the lag in abrupt changes in solar flux, it is negligible since this would undoubtedly be due to clouds which would completely eliminate concentrating solar resource.

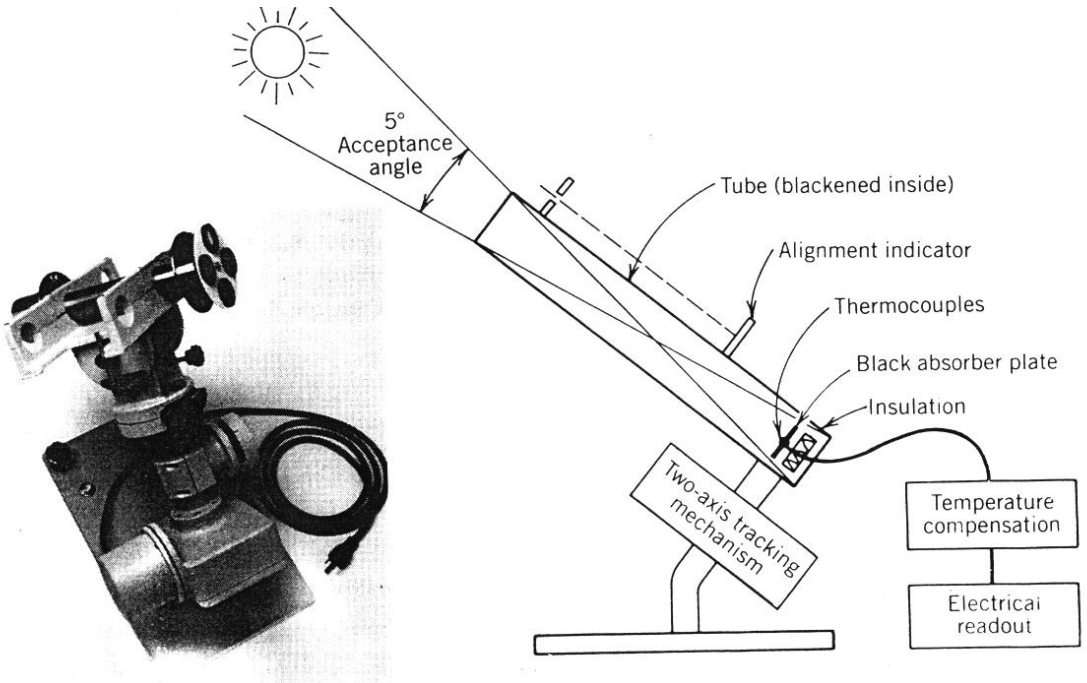

Figure 1.18: Pyrheliometer schematic depicting operating requirements for direct beam irradiance data collection [42].

Photoelectric Sensors

Photoelectric pyranometers which use cadmium sulfide photocells or silicon photo-diodes are an alternate, inexpensive means of measuring irradiance. They typically only respond to the visible and near infrared regions of the solar spectrum so do not give an accurate estimate of resource for concentrating solar but are normally perfectly suited for PV power which has a selective resource spectrum. They also have a much faster response to change. Where thermoelectric instruments have a 1-5 second response time due to thermal lag, photoelectric detectors respond within microseconds [34]. This makes these sort of sensors ideal for instantaneous ramp rate analysis and mitigation. In the case of the Prosperity Site, Campbell Scientific L1200X photo-diode pyranometers are used to allow use for such analyses.

Both photoelectric and thermoelectric pyranometers have the ability to measure global horizontal irradiance (GHI), direct normal irradiance (DNI) and plane of array (POA) irradiance depending on equipment set-up. For example, to measure diffuse irradiance, a shadowband could be placed directly between the sensor and the sun to allow only the light scattered by the atmosphere and surroundings to reach the detector. A comparison of applications for these instruments along with set-up descriptions can be seen in table 1.2.

Table 1.2: Various radiation measurements devices, measurement types, field of view (FOV) and installation characteristics [34].

Radiometer Type	Measurement	FOV (full angle)	Installation
Pyrheliometer	DNI	$5.7° - 6.0°$	Mounted on automatic solar tracker for alignment with the solar disk
Pyranometer	GHI	$2\ \pi$ steradians	Mounted on stable horizontal surface free of local obstructions
	DHI	$2\ \pi$ steradians	Mounted on automatic solar tracker fitted with shading mechanism or on a manually adjusted shadowband platform for blocking DNI from detector surface
	POA	$2\ \pi$ steradians	Mounted in the POA of the flat plate solar collector

Obtaining these measurements and understanding their meaning isn't enough. These instruments must be maintained through calibration to ensure accuracy. Likewise, if a user is expecting a realistic determination of resource behavior for a potential or existing solar power generation site, the instrument and generation equipment set-up must be understood.

1.7.2 Uncertainty

Calibration

Despite high-standards manufacturing techniques, each radiometer contains a unique deviation in the relationship between output voltage and the interpreted irradiance. This relationship, defined as Rs (μV/Wm^{-2}), must be periodically determined using a measurement reference which, for the highest standards, must be traceable to the World Radiometric Reference (WRR) [34]. The WRR provides a standardization of irradiance measurement with the use of absolute cavity radiometers within an accuracy of 0.3% to ensure worldwide measurement homogeneity to within 0.1% precision [43].

Signal noise and correlation with model

Beyond the relationship between voltage and irradiance there are other sources of uncertainty in irradiance measurement. Once measurement data are obtained, there is still a possibility that the data could be noisy depending on the "radiometer design, hardware installation, data acquisition method, measurement system O&M, calibration method and frequency, and possible real-time or posteriori corrections" [34]. For example, surrounding electronics, television or radio broadcast towers, and other communications devices can emit electromagnetic radiation causing the transferring measurement signal to become disturbed. Understanding the types and values for uncertainties from all sources, one can then use the Guide to the Expression of Uncertainty in Measurement (GUM) method as defined by the World Meteorological Organization (WMO) to find combined and expanded uncertainties and is currently the accepted method for irradiance measurements [34].

1.7.3 Correlation

Sensor field or weighted average

For use in analysis, considerations must be taken of the data that are being used. Photoelectric sensors provide substantial detail of variability, but this is a worst-case scenario because they are point measurements and do not directly translate to energy received. Clouds causing high-frequency intermittency take time to travel over a PV array causing power ramps to be smoothed depending on array footprint. It is known that time averaged irradiance from a multiple sensor field is a better measurement of experienced array power. This, however, requires the added cost of installing and maintaining multiple sensors.

In a particular analysis, a comparison of several sensor field interpolation schemes and a simple low pass filter of a single sensor determined that data from a single sensor could be used to interpret experienced power [44]. The cumulative probability distribution function for ramp rates is shown in figure 1.19 where the multi-sensor data ramp rates are shown in blue and the unaltered single sensor is shown in black. The red and green dotted lines represent ramp rates calculated using the single sensor data with a 150 second and 180 second average creating a closer correlation to the sensor field. This means that, providing the low pass filter time constant is properly calibrated, instrumentation investment can be reduced.

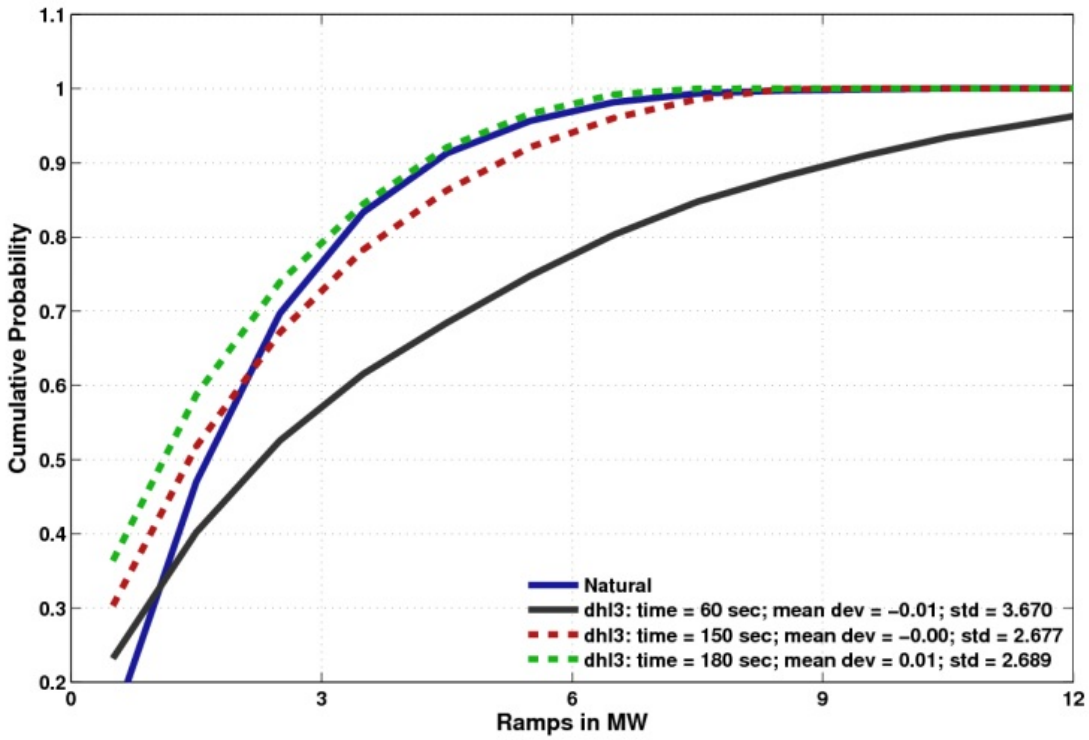

Figure 1.19: Probability distribution of ramp rates for multi-sensor network and single sensor [44]

Degradation

PV arrays can have intended performance lifetimes beyond twenty years during which PV cells are subjected to damaging sunlight and thermal cycling causing an on average 0.5%/year decrease in efficiency [45]. Providing measurement instrument calibration takes place at an appropriately high frequency, the change in correlation between measurements and experienced power should stay relatively constant.

Soiling

Array performance can also vary due to cleanliness causing deviations in the correlation between measurements and received power. Dust and other particulates can become caked on modules blocking light from reaching PV cells and causing a decrease in overall efficiency. It is difficult to quantify the losses experienced due to soiling because effects can vary greatly even between nearby sites [46]. In a particular study, the rate of efficiency losses due to soiling were found to be on average an order of magnitude larger than those experienced due to degradation [47]. It was also determined that had there been one cleaning halfway through the time period analysed there would be an average of 0.81% more annual energy with some sites seeing as much as a 4% increase.

1.8 Input Data

Numerical Weather Prediction

Because many existing irradiance prediction methods, including the one presented in this thesis, utilize weather forecast data, it is important to understand the many weather forecasts available. Modern weather predictions typically rely on numerical weather prediction (NWP) consisting of advanced fluid dynamics algorithms to model the multi-phase turbulent mixing occurring within the Earth's boundary layer [48]. Among the different NWP models there is variation in spatial and temporal resolution, output parameters, and forecast horizon (availability ahead of time). Specifications are shown in table 1.3 for three models which underwent comparison.

Table 1.3: Spatial resolutions, temporal resolutions and forecast horizons for three NWP forecasts [49]

	NAM	GFS	ECMWF
Spatial resolution	0.11° (12.2 km^2)	0.5° (55.6 km^2)	0.25° (27.8 km^2)
Radiative transfer model	GFDL-SW	RRTM-SW	McRad
Output temporal resolution/forecast horizon	1 h/36 h; 3 h/84 h	3 h/ 180 h	3 h/14 h; 6 h/240 h

These operational NWP models which include short-wave solar radiation forecasts (equivalent to GHI) within the continental United States are the North American Mesoscale Model (NAM), Global Forecast System (GFS) and European Centre for Medium-Range Weather Forecasts (ECMWF). An example of a GHI forecast made available by NAM is shown in figure 1.20.

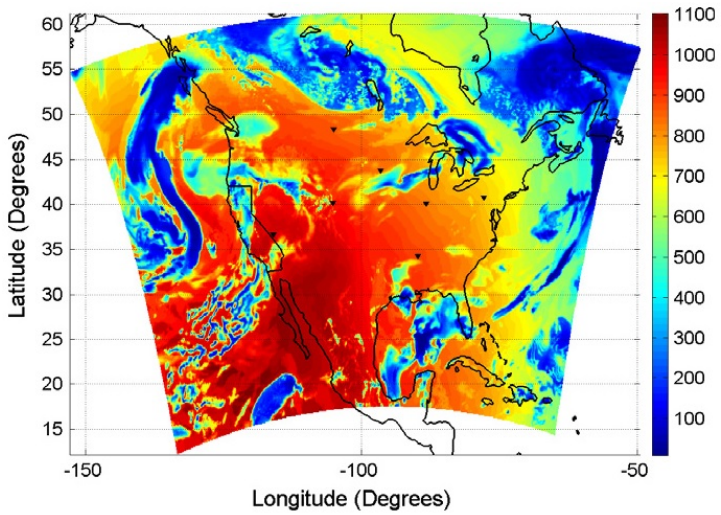

Figure 1.20: NAM GHI forecast (W/m^2) for April 10, 2010 at 2000 UTC [49]

Each of these models make considerations for varying effects due to different gases such as water vapor, ozone, oxygen, carbon dioxide, methane, and nitrous oxide. Additionally, the ECMWF considers aerosols and various CFCs. This is

highly dependant on the radiative transfer model used by each forecast.

These methods are an effective means of forecasting future solar resource. The advantage to the method presented in this paper is level of investment. The methods discussed above are commercial services which charge for irradiance forecasts and high spatial resolution historical radiation data. Depending on the size of a particular solar power generation site, one might not be able to justify the cost.

Ground imagery

Ground imagery is a recent area of investigation for developing very short-term (seconds to minutes) irradiance forecasts to aid in intermittency mitigation. By comparing periodically captured images of the sky, a characterization and path for existing clouds can be determined and used to predict using cloud vectoring or an ANN. Figure 1.21 shows an example of a total sky imager together with cloud motion vectoring [50]

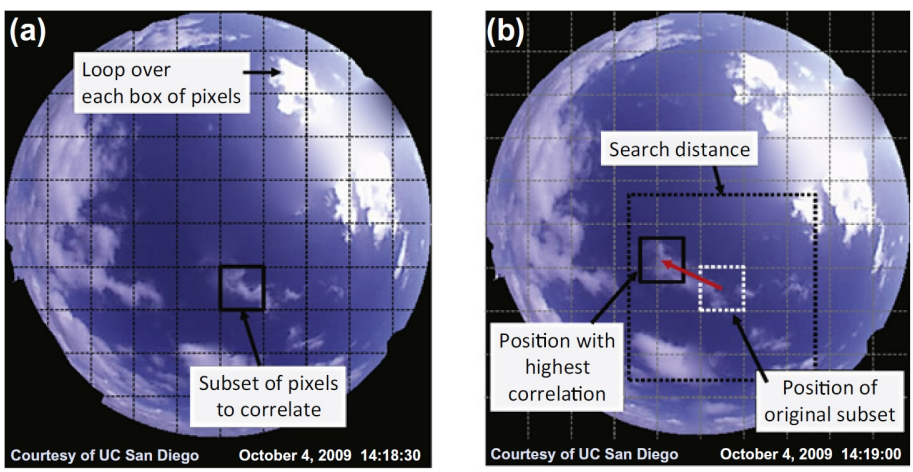

Figure 1.21: Sequential images used for cloud vectoring [50]

Using these images, clouds are identified and then tracked by pattern recognition to predict disturbances. Current results admit that prediction performance is lim-

ited by equipment shortcomings, but improvements are expected with upgrades to instruments.

Cloud Classification

One of the biggest challenges for high-precision irradiance prediction is cloud classification. Different clouds behave differently with respect to solar radiation absorption and attenuation. NWP, with its current spatial and temporal resolutions, is very limited for distinguishing between varying cloud types. Figure 1.22 shows nine cloud types located according to their respective visible optical depths and cloud-top pressures as calculated from five year's data [51].

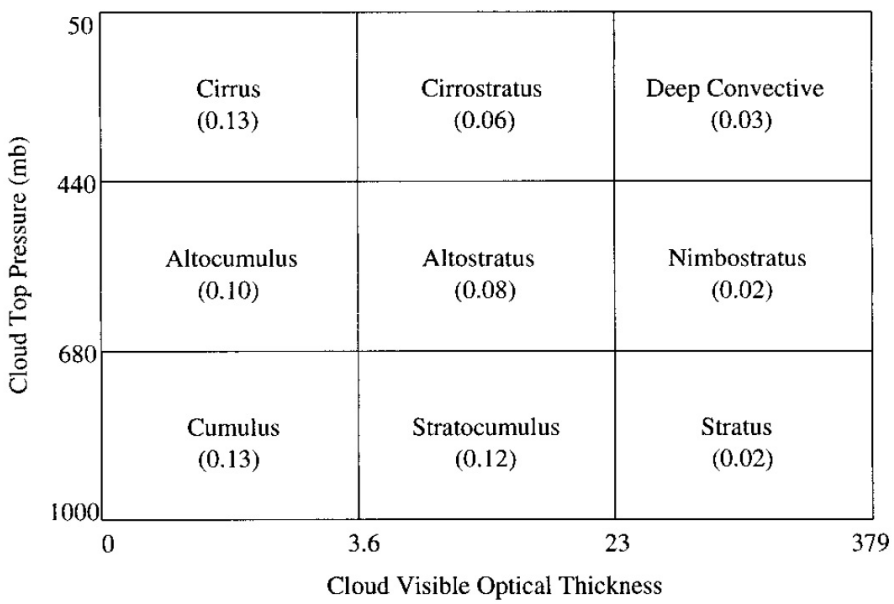

Figure 1.22: Cloud types and cloud fractions in terms of cloud top pressure and visible optical depth [51]

These cloud classifications, however, are not used in the method presented in this thesis and are currently not posted by agencies such as the National Weather Service.

Instead a cloud fraction was assigned to cloud forecasts obtained. This process will be discussed further in Section 3.1.

1.9 Method Presented Here

With these factors in mind, the prediction method described here pursues a correlation between publicly-available day-ahead NWS percent cloud cover and relative humidity forecasts and historical sensor field irradiance data through regression analysis. These forecast parameters are applied as a clear-sky index to clear-sky irradiance data calculated using known equations for solar geometry. Several correlation types are investigated and coefficients are optimized to minimize RMSE error with respect to the averaged sensor field historical data. Though the motivation for this study was to develop a simple, inexpensive resource prediction method for utility-scale PV power generation with battery energy storage, the method was formed to be applicable to other fixed-plate solar generation with varied means of energy storage.

Chapter 2

Clear-Sky Irradiance Model

2.1 Solar Geometry

Before any prediction can be made, a baseline for clear-sky irradiance must be established. Many models exist to describe solar resource based on solar geometry which models the sun's orientation with respect to ground-based collectors, a diagram of which is shown in figure 2.1. In the present case, the model described by Duffie & Beckmann was used to calculate one-minute temporal resolution clear-sky irradiance data throughout the year [35].

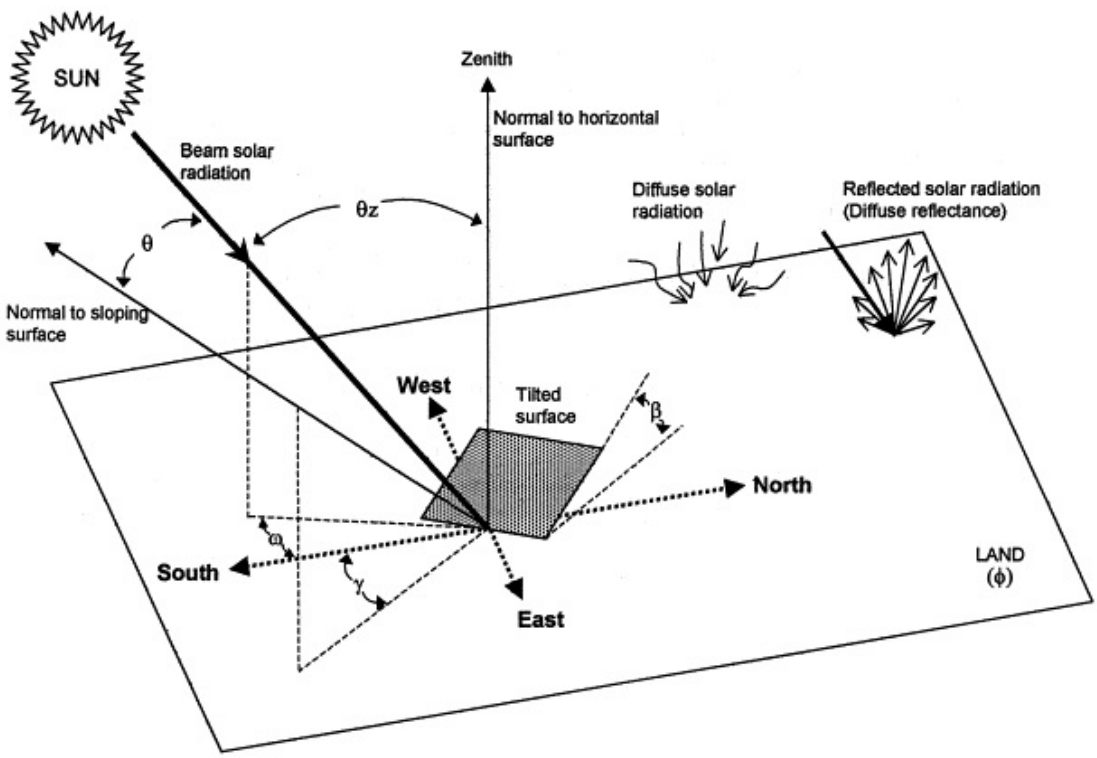

Figure 2.1: Solar geometry diagram defining conditions dictating the Sun's orientation with respect to ground-based collectors [35].

The parameters shown change constantly throughout the day, varying the amount of clear-sky radiation reaching the earth's surface. Additionally, the daily radiation profile changes throughout the year due to the tilt of the earth's axis with respect to the sun during its yearly orbit. Terrestrial irradiance is composed of two components, direct beam and diffuse, the latter of which is useful for fixed plate PV power generation and depends on atmospheric attenuation and reflection off of surroundings. Particularly, direct beam radiation depends on collector orientation. The variables describing the orientation of the sun with respect to fixed plate collectors are shown in table 2.1.

Table 2.1: Table of nomenclature defining solar geometry in figure 2.1 used to calculate clear-sky irradiance [35].

Variable	Description
ϕ	**Latitude**, the angular location north or south of the equator, north positive, $-90° \leq \phi \leq 90°$
δ	**Declination**, the angular position of the sun at solar noon with respect to the plane of the equator, north positive, $-23.45° \leq \delta \leq 23.45°$
β	**Slope**, the angle between the plane of the surface in question and the horizontal; typically acute angles for fixed plate collectors, $0° \leq \beta \leq 90°$
γ	**Surface azimuth angle**, the deviation of the projection on the horizontal plane normal to the surface from the local meridian, with zero due south, east negative, and west positive, $-180° \leq \gamma \leq 180°$
ω	**Hour angle**, the angular displacement of the sun east or west of the local meridian due to rotation of the earth on its axis at 15° per hour; morning negative, afternoon positive
θ	**Angle of incidence**, the angle between the beam radiation on a surface and the normal to the surface, $0° \leq \theta \leq 90°$
Additional angles describing position of sun in sky:	
θ_z	**Zenith angle**, the angle between the vertical and the line to the sun
α_z	**Solar altitude angle**, the angle between the horizontal and the line to the sun, complement of zenith angle
γ_s	**Solar azimuth angle**, the angular displacement from south of the projection of beam radiation on the horizontal plane; east of south negative, west of south positive

2.2 Extraterrestrial Radiation

The first step to developing an estimate of solar radiation on the earth's surface is to estimate the extraterrestrial radiation before it passes through the atmosphere. This is dependant on the distance between the earth and the sun at a particular point in it's elliptical orbit. An adjustment from our calendar day-numbering to solar days in shown in equation 2.1, where B is the solar day-number and n is the calendar day-number. This allows one to keep conventional calendar day-numbering for final irradiance estimates.

$$B_n = (n-1)\,\frac{360}{365} \tag{2.1}$$

Next, the solar day-number is used to determine the radiation immediately outside the earth's atmosphere on the n^{th} calendar day, $I_{o,n}$, as shown in equation 2.2. The solar constant, I_{sc}, is the radiation emitted by the sun over all wavelengths and varies among studies, but is accepted to be 1367 W/m^2 in the model used.

$$\begin{aligned} I_{o,n} = I_{sc}\,(1.000110 + 0.034221\,cos\,B_n + 0.001280\,sin\,B_n \\ +0.000719\,cos\,2B_n + 0.000077\,sin\,2B_n) \end{aligned} \tag{2.2}$$

2.3 Solar Time Correction

Solar geometry also requires using solar time meaning the sun is highest exactly at noon. Within time-zones, solar time belonging to a single longitude, known as a standard meridian, is adopted by surrounding areas for time-keeping causing solar noon to vary from local noon. To adjust for this deviation, one first uses the equation of time (in minutes) shown in equation 2.3.

$$\begin{aligned} E_n = 229.2\,(0.000075 + 0.001868\,cos\,B_n - 0.032077\,sin\,B_n \\ -0.014615\,cos\,2B_n - 0.04089\,sin\,2B_n) \end{aligned} \tag{2.3}$$

This parameter is then used to find the n^{th} calendar day's correction value from local to solar time using equation 2.4. Here, the longitude of the time-zone's standard meridian is denoted by L_{st} and the longitude of the location where irradiance is to be estimated is denoted by L_{loc}.

$$t_{adj,n} = Solar\,time - standard\,time = 4\,(L_{st} - L_{loc}) + E_n \tag{2.4}$$

2.4 Incident Beam Radiation

So far, the equations described have addressed daily changes in earth's position and the location's daily corrections for time. The following equations quantify the orientation of the sun with respect to a flat-plate collector in order to determine the angle of incidence of direct beam irradiance. The last parameter which is treated as constant for each n^{th} calendar day is declination which is calculated using equation 2.5.

$$\delta_n = 23.45\,sin\left(360\,\frac{284+n}{365}\right) \tag{2.5}$$

To determine the angle of rotation of the earth depending on time, hour angle ω, the model utilizes equation 2.6. Inputting local time, one will produce the current hour angle which changes 15°/hour with the earth's 24-hour rotation. Note that all following equations for calculating direct beam radiation can be used to determine radiation estimates at any temporal resolution.

$$\omega = 15\left(\frac{t_{loc} + t_{adj,n}}{60} - 12\right) \tag{2.6}$$

Next, the model requires the solar azimuth angle, γ_s, which is determined by a relationship between the hour angle, ω, and the sunset hour angle, $\omega_{ew,n}$. The sunset hour angle is the angle when the sun is due west or east on the n^{th} day and is found using equation 2.7.

$$cos\,\omega_{ew,n} = tan\,\delta_n / tan\,\phi \tag{2.7}$$

The relationship between these two angles determines a set of positive-negative sign changes along with another parameter referred to as the pseudo solar azimuth, γ'_s, as shown in equations 2.8a - 2.8d.

$$sin\gamma'_s = \frac{sin\omega cos\delta_n}{sin\theta_z} \tag{2.8a}$$

$$C_1 = \begin{cases} 1 & \text{if } |\omega| < \omega_{ew} \text{ or } |\omega_{ew,n}| < 1 \\ -1 & \text{otherwise} \end{cases} \tag{2.8b}$$

$$C_2 = \begin{cases} 1 & \text{if } \phi(\phi - \delta_n) \geq 0 \\ -1 & \text{otherwise} \end{cases} \tag{2.8c}$$

$$C_3 = \begin{cases} 1 & \text{if } |\omega| \geq 0 \\ -1 & \text{otherwise} \end{cases} \tag{2.8d}$$

The case for C_1 considers when $\omega_{ew,n}$ is greater than one meaning the sun is never due west or east of the location in question. The signs and pseudo solar azimuth are then input into equation 2.9 to yield the instantaneous solar azimuth.

$$\gamma_s = C_1 C_2 \gamma'_s + C_3 \left(\frac{1 - C_1 C_2}{2} \right) 180 \tag{2.9}$$

The zenith angle, θ_z, which represents the angle between the vertical and the line to the sun is then found using equation 2.10. Its value throughout the day is dependant on only the hour angle since altitude, ϕ, and declination, δ_n, are constant for any particular day.

$$cos\,\theta_z = cos\,\phi\,cos\,\delta_n\,cos\,\omega\;+\;sin\,\phi\,sin\,\delta_n \tag{2.10}$$

Finally, the angle of incidence for beam radiation upon a tilted surface is shown in equation 2.11. Note that for horizontal surfaces the angle of incidence is equal to the zenith angle because both the surface azimuth and tilt angles are zero and cancel terms out. This value is essentially the dot product providing the component of beam radiation normal to the surface.

$$\begin{aligned} cos\,\theta = {} & sin\,\delta_n\,sin\,\phi\,cos\,\beta \\ & -sin\,\delta_n\,cos\,\phi\,sin\,\beta\,cos\,\gamma \\ & +cos\,\delta_n\,cos\,\phi\,cos\,\beta\,cos\,\omega \\ & +cos\,\delta_n\,sin\,\phi\,sin\,\beta\,cos\,\gamma\,cos\,\omega \\ & +cos\,\delta_n\,sin\,\beta\,sin\,\gamma\,sin\,\omega \end{aligned} \tag{2.11}$$

2.5 Atmospheric Transmittance

With the parameters discussed up to this point, extraterrestrial radiation and orientation for beam radiation are characterized. Lastly, it is necessary to model the clear-sky atmospheric effects on radiation transmittance caused by absorption and scattering of light. Particles in the atmosphere segregate extraterrestrial radiation into two terrestrial radiation components: direct beam, I_b, and diffuse, I_d. Direct beam radiation is a function of the extraterrestrial radiation and angle of incidence discussed previously along with the beam transmittance, τ_b, found using equations 2.12a - 2.12d where the location's altitude is denoted by A.

$$\tau_b = a_0 + a_1\, exp\left(\frac{-k}{cos\,\theta_z}\right) \tag{2.12a}$$

$$a_0^* = 0.4237 - 0.00821\,(6 - A)^2 \tag{2.12b}$$

$$a_1^* = 0.5055 - 0.00595\,(6.5 - A)^2 \tag{2.12c}$$

$$k^* = 0.2711 - 0.01858\,(2.5 - A)^2 \tag{2.12d}$$

The constants a_0^*, a_1^* and k^* are for a standard atmosphere with 5 km visibility. These values are then multiplied by a correction factor depending on the location's climate type such that $a_0 = r_0\, a_0^*$, $a_1 = r_1\, a_1^*$ and $k = r_k\, k^*$. The various correction factors for climate types are shown in table 2.2.

Table 2.2: Correction factors for climate types affecting atmospheric transmittance of radiation.

Climate Type	r_0	r_1	r_k
Tropical	0.95	0.98	1.02
Mid-latitude summer	0.97	0.99	1.02
Subarctic summer	0.99	0.99	1.01
Mid-latitude winter	1.03	1.01	1.00

Unlike direct beam radiation which depends on angle of incidence, the diffuse radiation is dependant only on the extraterrestrial radiation and diffuse radiation transmittance because it approaches a collector from all directions which the flat plate collector is facing. Note that for concentrating solar applications, diffuse radiation cannot be used since it cannot be focused to a single point. The diffuse transmittance is a function of the beam transmittance found using the empirical relationship shown in equation 2.13.

$$\tau_d = \frac{I_d}{I_o} = 0.271 - 0.294\,\tau_b \tag{2.13}$$

Finally, the total irradiance available is found by adding the direct beam and diffuse components as shown in equation 2.14. This represents the instantaneous irradiance in power per unit area on a tilted surface.

$$I_{ClearSky} = I_{o,n}\,\tau_b\,cos\,\theta + I_{o,n}\,\tau_d \tag{2.14}$$

2.6 Site-Specific Parameters

This model requires site-specific conditions to determine the clear-sky irradiance at any given time during the day. Since this method is being tested using data collected from the Prosperity Site, the array's design and location were defined as shown in table 2.3. Additionally, contributions of secondary effects, such as diffuse irradiance, air mass attenuation and local to solar time adjustments based on location with respect to the local time zone's standard meridian were also considered.

Table 2.3: Prosperity Energy Storage Project Site Specifications for Clear-Sky Irradiance Model.

Characteristic	Variable	Value
Latitude	ϕ	35° North
Longitude	L_{loc}	106.6° West
Local Standard Meridian	L_{st}	105° West
Elevation	A	1609.344 m
Array tilt angle	β	25°
Panel azimuth	γ	0° from due South
Climate type	-	Mid-latitude summer

With these site-specific conditions, the theoretical one-minute temporal resolution clear-sky irradiance was calculated for the entire year as shown in figure 2.2. The profile shows two points of maximum potential resource which is to be expected because it is established that one should position a solar module at a tilt angle

of either ($|latitude| - 15°$) or ($|latitude| + 15°$) depending whether the user desires summer or winter optimum performance, respectively [40]. This dual-maximum resource was intentional for the Prosperity Site design to provide a relatively more level day-to-day power profile.

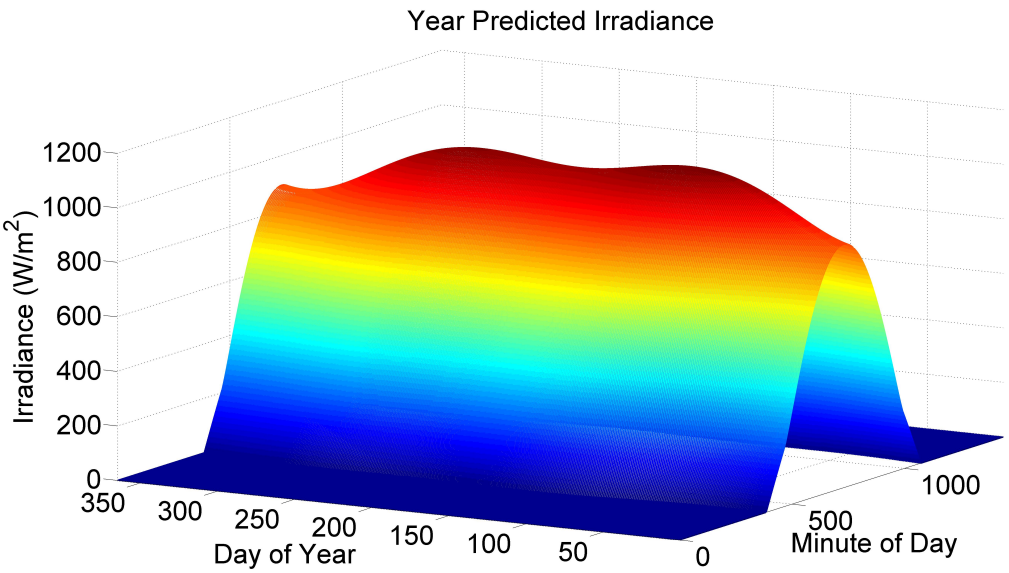

Figure 2.2: Yearly clear-sky theoretical irradiance profile for the Prosperity Site array location and orientation.

2.7 Model to Historic Data Comparison

Furthermore, to test the model's accuracy, theoretical clear-sky predictions were plotted against historical data from days with visually clear sky conditions. Figure 2.3 shows a particular day demonstrating the model's typical performance for matching with historical data.

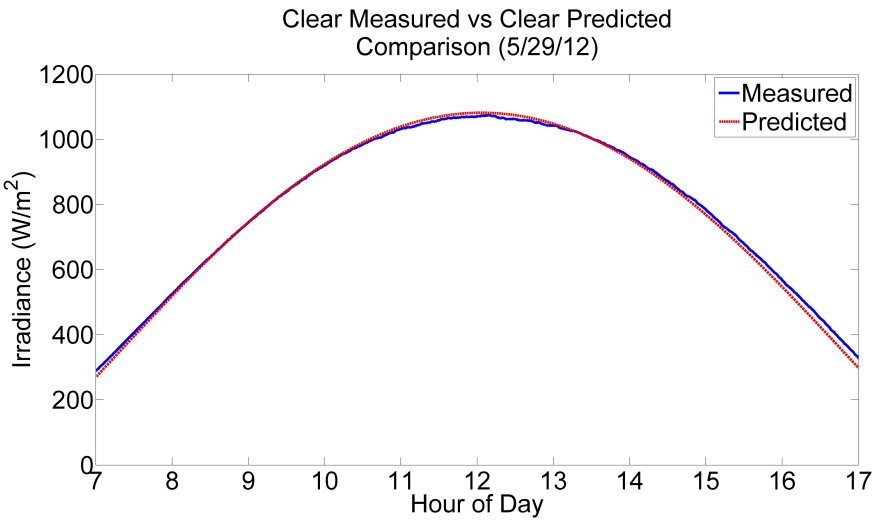

Figure 2.3: Clear day's irradiance (5/29/2012) vs clear day prediction showing accuracy of clear sky irradiance model.

To show this method is accurate independent of day, figure 2.4 shows another model irradiance profile. While there is some variation, this model's performance is comparable to other models and may attribute inaccuracies to varying atmospheric conditions such as dust, moisture, aerosols and so on.

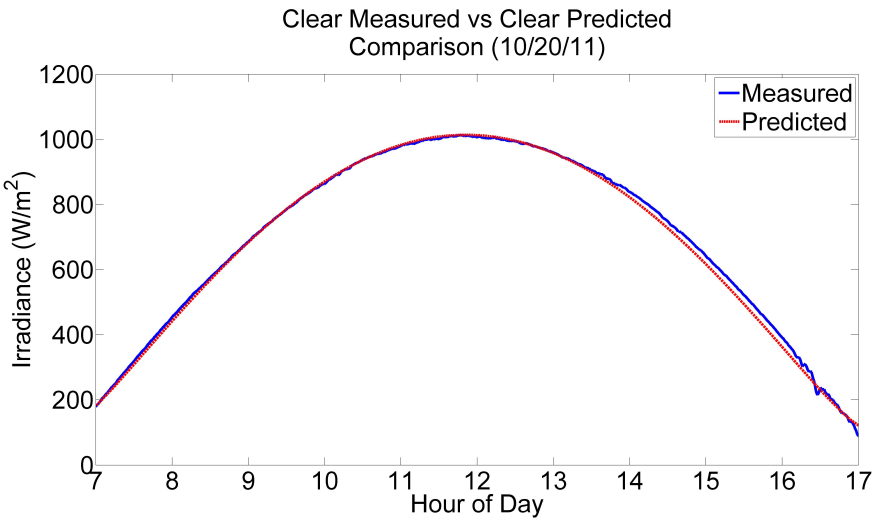

Figure 2.4: Clear Day's Irradiance (10/20/2011) vs Clear Day Prediction; in reference to figure 2.3 shows accuracy independent of day.

Chapter 3

Methods and Evaluation

3.1 National Weather Service Forecasts

In this study, to predict next day solar resource, National Weather Service (NWS) forecast data were used as a way of predicting a loss of irradiance due to cloud cover, and therefore daily insolation. NWS forecasts are obtained using Numerical Weather Prediction (NWP) by the National Oceanic and Atmospheric Administration (NOAA) and made available at 3 hour, 6 hour and 12 hour intervals. In the case for the forecasts used in this study, the 3 hour interval forecasts are available up to 60 hours ahead.

In the interest of exploring the applicability to day-ahead planning for peak shaving, the forecasts posted the evening prior to the day in question were sought. Among other forecasted values, the weather forecasts considered are shown in table 3.1 with their respective values.

Table 3.1: Forecast parameters available from the National Weather Service.

Parameter	Value
Temperature	Degrees Fahrenheit
Dew point	Degrees Fahrenheit
Relative Humidity	$0\% - 100\%$
Wind Direction	N, E, S, W, NE, SE, SW, or NW
Wind Speed	miles per hour (MPH)
Cloud Cover	CL, FW, SC, B1, B2, or OV

Note in table 3.2 that the cloud cover forecast values have a unique cloud characterization code. These codes correspond to an associated range of sky cover percentages to provide a general idea of visibility usually for aviation. To quantify these values for the prediction method, the codes were assigned a single percent value specifically in this study. The cloud cover codes, their NOAA defined values and the values assigned for this study are shown in table 3.2.

Table 3.2: Cloud cover code meanings, percent ranges and assigned single values.

Code	Meaning	NOAA Expression	NOAA %CC Range	%CC
CL	Clear	Sunny or Clear	$0\% \leq \%CC \leq 5\%$	0
FW	Fair Weather	Sunny or Mostly Clear	$5\% < \%CC \leq 25\%$	20
SC	Scattered Clouds	Mostly Sunny or Partly Cloudy	$20\% < \%CC \leq 50\%$	40
B1	Broken Type 1	Partly Cloudy or Mostly Cloudy	$50\% < \%CC \leq 69\%$	60
B2	Broken Type 2	Mostly Cloudy or Considerable Cloudiness	$69\% < \%CC \leq 87\%$	80
OV	Overcast	Cloudy or Overcast	$87\% < \%CC \leq 100\%$	100

Along with cloud cover, some correlations tested here also use relative humidity This forecast parameter was used in this study as opposed to others because it was

deduced that temperature, dew point and relative humidity are interrelated through psychrometrics [52]. Relative humidity is also an easily quantifiable measurement of how much moisture is in the atmosphere contributing to direct normal irradiance (DNI) attenuation.

3.1.1 Forecast Interpolation

Because the forecasts from the NWS are available at a 3 hour resolution, it is necessary to interpolate the forecasts to apply them to the one-minute temporal resolution clear-sky irradiance. This was done using either linear interpolation or cubic spline interpolation during this study using MATLAB's *interp1* function. It was ultimately concluded, however, that linear interpolation was most appropriate due to its simplicity and stability despite the spline interpolation's initial appeal to simulate the gradual approach and retreat of storm fronts or cloud banks. Additionally, spline interpolation has the tendency to create large spikes under certain data conditions creating percentages which are negative or greater than 100% as shown in figure 3.1.

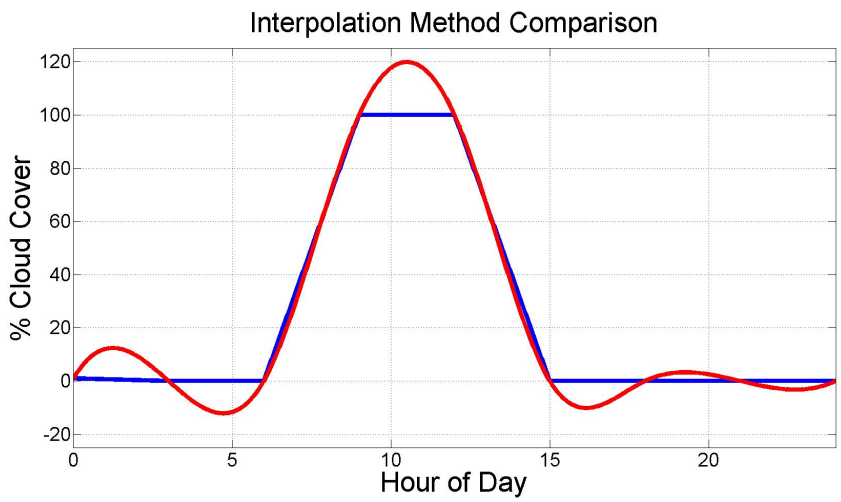

Figure 3.1: Sample data showing characteristics of linear (blue) and cubic spline (red) interpolation methods; note negative and greater than 100%CC using spline interpolation.

3.2 Historical Data

To validate the prediction methods, historical irradiance data from the Prosperity Energy Storage Site were used. The site is equipped with a currently modern SCADA (supervisory control and data acquisition) system to collect and store up to 220 data points per second [6].

To collect irradiance data, the site uses five plane-of-array (POA) Campbell Scientific L1200X photo diode pyranometers. Campbell Scientific claims a maximum absolute error of 5% in natural daylight and a typical absolute error of 3% [53]. Considering daily summer clear-sky insolation in Albuquerque, NM is about 8 kWh/m^2, this translates to a maximum clear-day insolation uncertainty of $\pm$ 0.4 kWh/m^2.

The pyranometers are located at each corner (North East, South East, South West, and North West) and at the center of the PV array. The five independent one-year data sets were then averaged to obtain the irradiance data for method optimization. A data average of multiple sensors within a sensor field is generally accepted as a better estimate of impinging irradiance as opposed to a single sensor [54]. This is because the instruments are point receivers and tend to exaggerate ramps experienced by an array [44].

The data used for the calibration and optimization of the prediction methods described in this study spanned from October 1st, 2011 to September 30th, 2012 at a one-minute time interval to provide an entire year of prediction comparison. The expectation was that the results would show varying prediction error from season to season. Early in testing, only two month's data were available for testing. While this allowed for early development, it was recognized that results could be biased toward the season and months tested.

Though finer time interval data were available from Prosperity, it was determined

that one-minute was sufficient to provide the accuracy desired. At a one-minute interval, clear-sky irradiance would vary by about 4 W/m^2 at most from one minute to the next which is roughly equivalent to the noise within the historical data itself which fluctuates by about $\pm$3 W/m^2 for one-second data.

Alternatively, intermittency caused by scattered clouds can create significant changes in irradiance at even sub-second frequency. This was addressed by collecting one-minute irradiance data which are the average of all data points within each the individual time stamp's one-minute window. For example, let there be N sub-second irradiance data points per minute. For a data point at time t, all data points from (t-30) seconds to (t+30) seconds are averaged. This allows the use of one-minute temporal resolution data which is computationally less expensive while maintaining a sufficient accuracy for calculating the total insolation.

3.2.1 Sliding Average

Historical PV irradiance data can be highly intermittent when scattered clouds are present. This intermittency makes it difficult to see correlation between predicted irradiance profiles and actual data. To aide in visual comparison, the higher frequency variability was filtered out using a centered one-hour sliding window average as seen in equation 3.1. A one-hour window was chosen for its ability to keep the basic form of the changing irradiance. Moreover, hourly error is shown in the results to help visualize hourly blocks of energy seeing increased error.

$$I_{avg}(t) = \frac{1}{t_w + 1} \sum_{i=t-t_w/2}^{t+t_w/2} I_{Historical}(i) \tag{3.1}$$

This one-hour time window is sized specifically to eliminate large spikes while maintaining hour-to-hour change in irradiance which is needed for hourly insolation

calculations. Application of sliding average irradiance data is illustrated in figure 3.2. The sliding average is also used in other plots shown in the results.

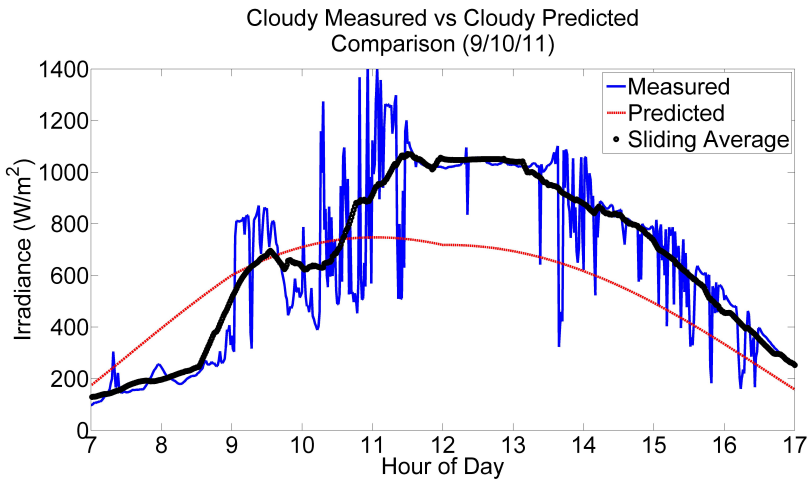

Figure 3.2: Sample irradiance profiles showing application of sliding window average of historical data.

3.3 Calculating Insolation

Because all of the data used in this study are in units of irradiance (W/m^2) and the goal is to develop a means of energy resource scalable for all array sizes, it was necessary to integrate the data for units of insolation (kWh/m^2). Equation 3.2 shows the calculation of insolation from irradiance.

$$H(a \leq t \leq b) = \int_a^b I(t)dt \tag{3.2}$$

There are many methods for numerically integrating data providing varying accuracy to the underlying function. A simple rectangle rule shown in equation 3.3 was used to calculate insolation for both predicted and measured irradiance data and provides sufficient accuracy for one-minute temporal resolution data.

$$H\left[\frac{\text{kWh}}{\text{m}^2}\right] = \sum_{t=a}^{b} I(t) \tag{3.3}$$

3.4 Early Methods

Since this study was begun, many aspects have changed to adopt improving methods for finding the best prediction of solar resource. At first, a linear correlation was explored using equation 3.4. Early on, the cloud weighting k was adjusted manually to visually center the irradiance and cumulative energy scattergram distributions.

$$I_{Prediction} = I_{ClearDay} * \left(1 - k * \left(\frac{\%CC}{100}\right)\right) \tag{3.4}$$

Later, relative percent error and numerical optimization were introduced to minimize the error with respect to either an irradiance prediction method or cumulative energy prediction method. Efforts for exploring the applicability of NWS cloud cover and relative humidity forecasts for irradiance prediction were abandoned once results yielded significantly worse error for insolation. Eventually the study expanded to investigate the potential accuracy of multiple correlations through numerical optimization to minimize insolation root mean square (RMS) error.

3.5 Correlations Evaluated

Though original attempts explored a linear correlation with percent cloud cover alone, other correlations and input data were investigated. This was to provide for degrees of freedom to the equation providing the potential for increased accuracy. The conditions to be varied include:

- Input data
  - Cloud cover only
  - Cloud cover and relative humidity
- Equation form
  - linear correlation
  - power and linear correlation
- Time period of optimization
  - Single annual value
  - Twelve monthly values

This yields four equations and a total of eight optimization scenarios. The equations tested are shown in equations 3.5 - 3.8.

Linear Correlation

$$I_{Prediction} = I_{ClearDay} * \left(1 - b * \left(\frac{\%CC}{100}\right)\right) \tag{3.5}$$

$$I_{Prediction} = I_{ClearDay} * \left(1 - b * \left(\frac{\%CC}{100}\right) * \left(\frac{\%RH}{100}\right)\right) \tag{3.6}$$

Power Correlation

$$I_{Prediction} = I_{ClearDay} * \left(1 - b * \left(\frac{\%CC}{100}\right)^{B}\right) \tag{3.7}$$

$$I_{Prediction} = I_{ClearDay} * \left(1 - b * \left(\frac{\%CC}{100}\right)^{B} * \left(\frac{\%RH}{100}\right)^{C}\right) \tag{3.8}$$

It is understood that with infinite degrees of freedom in an equation, one could forcibly create a perfect prediction for historical data, but it would not be repeatable from year to year, month to month, or day to day. This is why optimization was not performed to a finer temporal resolution than one month. Additionally, performance results should be understood to possess both temporal variability as climate and weather pattern changes occur regularly [19].

Using the equations 3.5 - 3.8, minute resolution predictions were calculated which would then resemble the altered curve in figure 3.3. One can see the effects of the scaled down clear sky irradiance profile shown in figure 2.2.

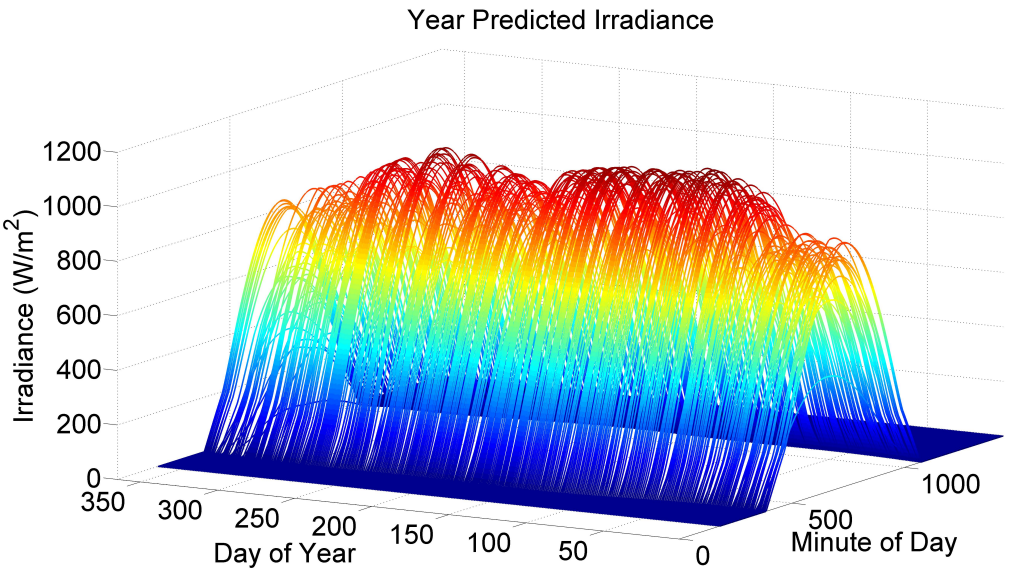

Figure 3.3: Prediction including cloud cover; characteristic for scaling down similar among equations 3.5 - 3.8.

Zooming in, the sample prediction for September 2011 is shown in figure 3.5 underneath the measured data in figure 3.4. Though the correlations described will vary in form, note how the prediction's lower profiles from September 5th to 10th correlate with the measured high intermittency days.

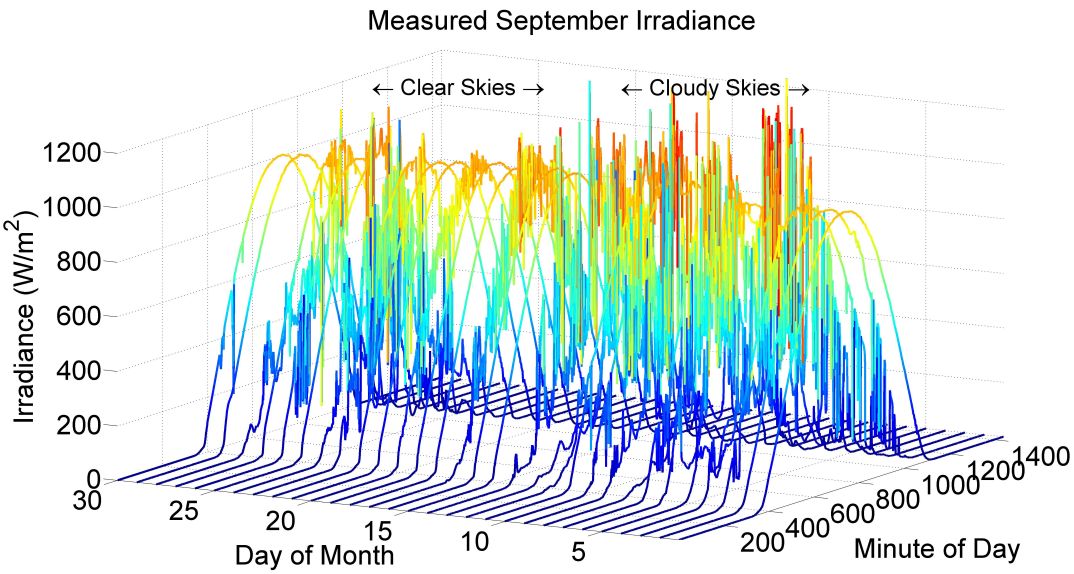

Figure 3.4: September's measured irradiance profile; note higher intermittency days

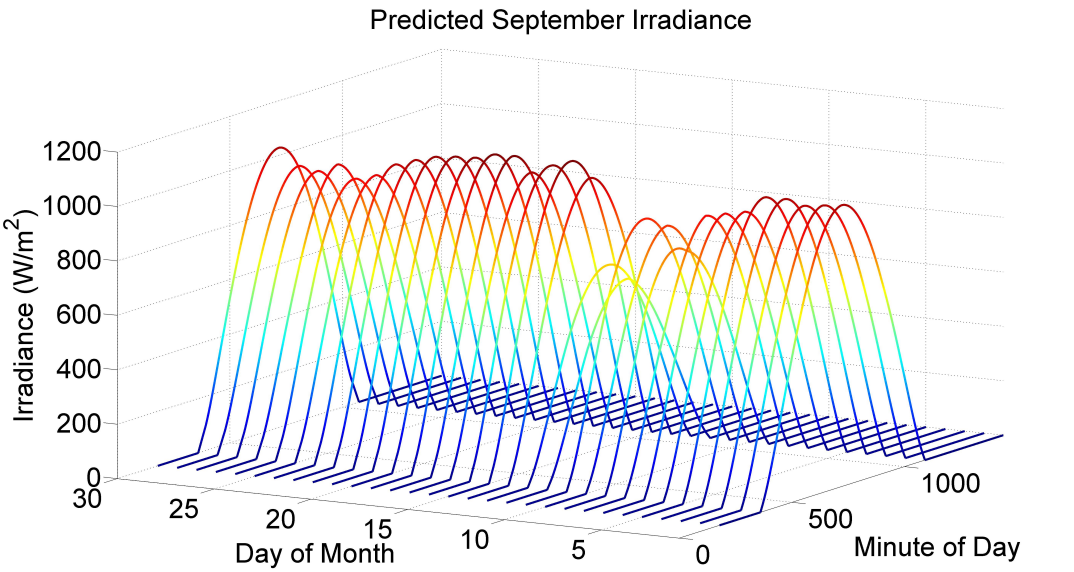

Figure 3.5: September's predicted irradiance profiles; compare spikes in figure 3.4 to lower curves.

3.6 Error Metrics

Each of the described methods had varying potentials for yielding an accurate prediction of daily insolation, but to compare each method to one another and, likewise, to other existing day-ahead resource predictions, an error metric was first defined then calculated. Several different error metrics have been used in the past such as mean absolute error (MAE), mean bias error (MBE) and relative mean bias error (rMBE) [49]. For evaluating the performance of this method, equation 3.9 which defines the root mean square error (RMSE; similar to least squares) was used because it reduces the effect of outliers caused by the occasional severe storm.

$$RMSE = \sqrt{\frac{1}{N}\sum_{i=1}^{N}\left(H_{Prediction} - H_{Measured}\right)^2} \tag{3.9}$$

Rare storms causing greater than typical reductions in insolation at 100% cloud cover will inappropriately affect other metrics such as mean percent error. This conclusion has been drawn in many other publications in evaluating irradiance and insolation predictions [26, 49]. While the annual total RMSE performance was evaluated for each method described, it was also calculated for annual RMSE for each significant daytime hour, monthly total RMSE, and monthly RMSE for each hour. In some cases, it is also useful to consider the relative root mean square error (rRMSE) which is defined in equation 3.10.

$$rRMSE = \sqrt{\frac{1}{N}\sum_{i=1}^{N}\left(\frac{H_{Prediction} - H_{Measured}}{H_{Measured}}\right)^2} \tag{3.10}$$

This metric shows how the prediction performs in reference to the measured data. As shown in the results chapter of this thesis, times with low absolute RMSE during

mornings and evenings (when clear-sky resource is low) have increased rRMSE values.

3.7 Optimization

In equations 3.5 - 3.8, the coefficients where optimized by calculating daily insolation predictions using a range of values. The linear coefficient b was restricted to be between zero and one to prevent negative irradiance values under any forecasted weather conditions. Considering all forecast values are between zero and one as well, the range of power values B and C were restricted to between zero and three though no values exceeded about 2.5. Note that powers greater than one will cause forecasts, which are always between 0 and 1, to reduce irradiance less. Together, these restrictions can be seen in table 3.3.

Table 3.3: Coefficients and value ranges for simple parametric optimization

Coefficient	Value	Step Size
b	$0 \leq b \geq 1$	
B	$0 \leq B \geq 3$	0.01
C	$0 \leq C \geq 3$	

Realizing the optimal coefficient values would be less accurate at some times of the year and more accurate at others, the coefficients were optimized for each of the four equations for both a single annual value and for twelve monthly values. This yielded eight unique sets of optimized coefficients, annual RMSE values, monthly RMSE values, annual RMSE values for each daytime hour, and monthly RMSE values for each daytime hour.

Chapter 4

Results

As addressed in the 'Methods and Evaluation' chapter of this thesis, early attempts to adjust equation coefficients were done manually. Though this method is obsolete and was replaced by parametric optimization, the process shed light on the general behavior of the correlation being tested. Because this process exemplifies the method's limitations and challenges, early images demonstrating correlation to historical data and lessons are covered prior to optimized figures and comparisons.

4.1 Visual Verification and Early Lessons

As seen in figure 3.3, the prediction generates a smooth curve with a frequency response of one day regardless of cloud cover. This is quite different from the intermittency evident in figure 3.4 which has oscillating spikes from minute to minute. Smooth behavior on a cloudy day is not realistic and should not be used for real-time control, but may be inevitable for day-ahead planning. Consider, for example, the irradiance data for September 10, 2011 shown in figure 4.1 which was a cloudy day with NWS forecasts to match.

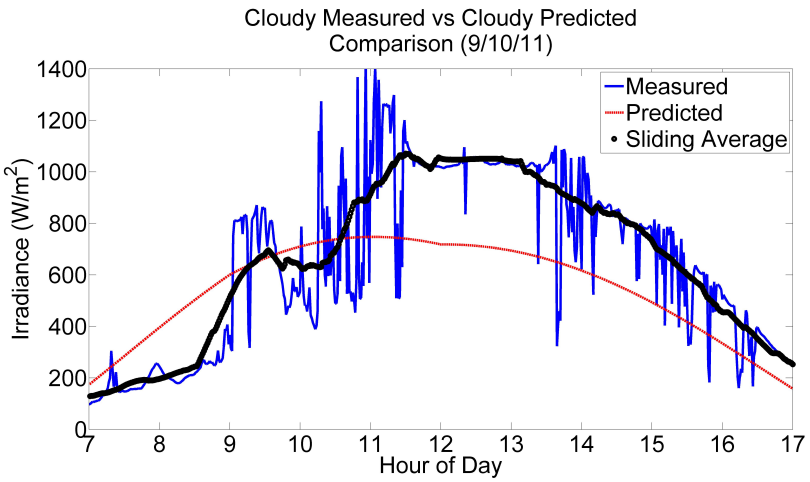

Figure 4.1: Irradiance over the course of a cloudy day (9/10/2011) and sliding average vs. prediction.

There is considerable difference between the prediction and sliding average curves. Even if this prediction is closely matched for cumulative energy, it may be misleading and cause a false assumption for afternoon peak shaving energy. As an overall comparison of the measured and predicted values, a one-to-one scattergram of irradiance values was generated as shown in figure 4.2. If compared to a perfect prediction method, all data points would be located on a line at 45° from the origin (i.e. $y = x$).

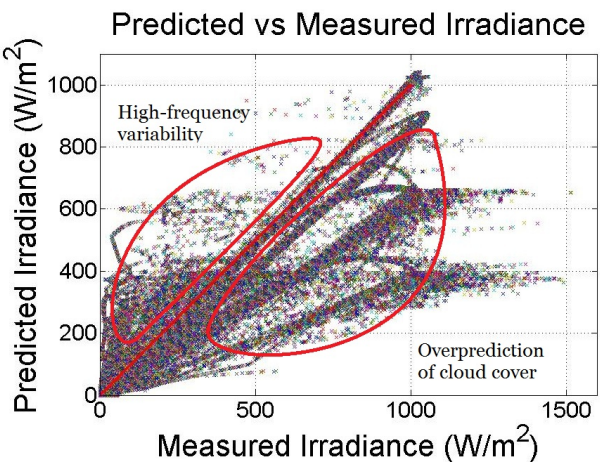

Figure 4.2: Initial Predicted vs. Measured Irradiance Plot; note patterns to right of red line.

The scattering around the $y = x$ line is due to cloud cover. The three line patterns, shown flowing below the $y = x$ line, are days where clouds were forecasted but did not occur. Moving away from $y = x$, the lines correspond to 20%, 50% and 80% cloud cover predictions. Note there is no trend line for 100% cloud cover. This is because the data set tested early in the analysis included no such cloud forecasts.

To aid in centering the scattergram, secondary lines were added out from the origin equating to a 50% error band. This means that for a predicted irradiance (e.g. 600 W/m^2) we have an equal range ($\pm$300 W/m^2) of irradiance above and below the predicted value. To show this graphically, consider the sample data in figure 4.3.

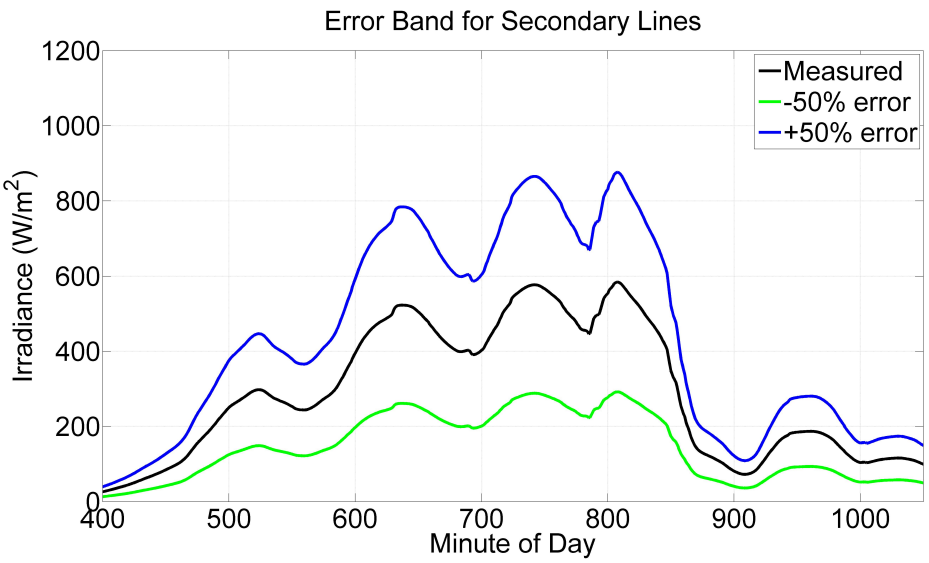

Figure 4.3: Centered Predicted vs. Measured Irradiance; average distribution of scatter.

The "measured" data in black runs between two different predictions, one at a positive 50% error (in blue) and the other at a negative 50% error (in green). The predictions are then plotted on a measured versus predicted irradiance scattergram yielding figure 4.4.

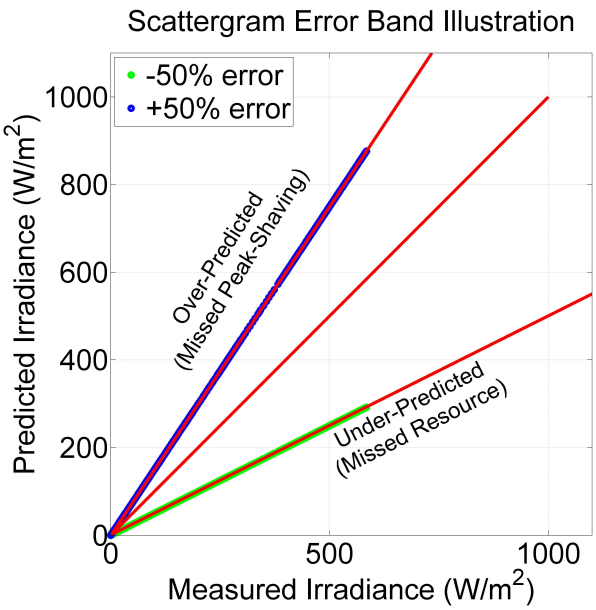

Figure 4.4: Centered Predicted vs. Measured Irradiance; average distribution of scatter.

Note were each curve is represented on the plot. These positions either above or below the $y = x$ line indicate either a over- or under-prediction, respectively. With the over-predicted energy resource in blue, a shifting schedule would not charge available energy storage capacity in order to take advantage of the anticipated insolation. However, when this insolation is actually lower, the available energy storage may not be sufficient for peak-shaving. Conversely, the green prediction curve would cause the planner to charge the storage during the night in order to accomodate the next-day peak. When greater than expected insolation is experienced, the PV system may not be able to take full advantage of the resource for peak-shaving. However, the PV system may be able to immediately dispatch this surplus power if utility companies desire. These guiding trendlines applied to the actual irradiance data which has been visually centered is shown in figure 4.5.

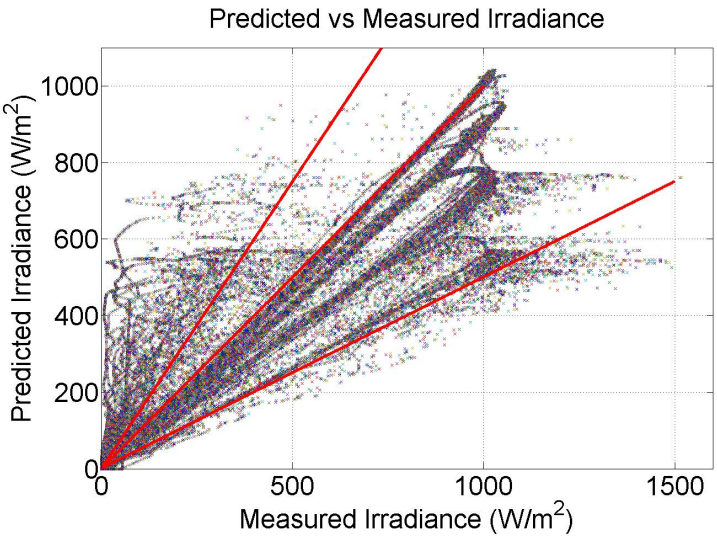

Figure 4.5: Centered Predicted vs. Measured Irradiance; average distribution of scatter.

The sliding average of the measured data provides further clean-up by removing many of the large high-frequency spikes seen in measured data. This also yields clear path lines for specific days' sliding average irradiance curves as shown in figure 4.6.

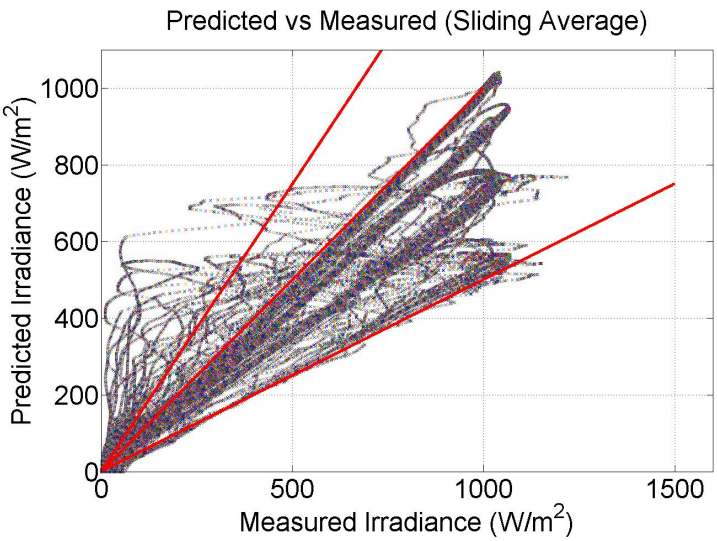

Figure 4.6: Predicted vs. sliding average of measured irradiance scattergram.

For a closer look, profiles for two days of irradiance are compared in figure 4.7. The line nearly coincident with the $y = x$ line is a clear day. The scattering black path and green looped path are respectively the measured and sliding average irradiance profiles for a cloudy day.

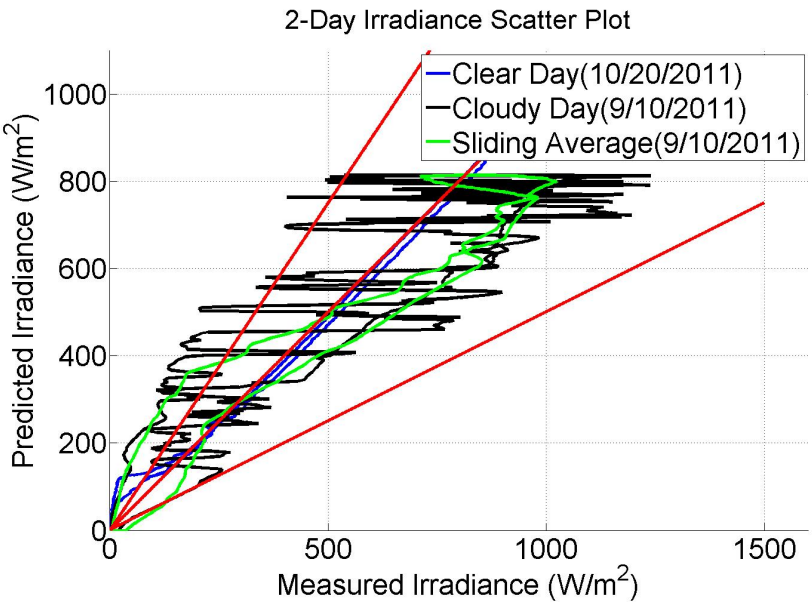

Figure 4.7: Measured vs. predicted irradiance scattergram for clear and cloudy day comparison.

At this point early in the study, the cloud cover coefficient was increased or decreased to center the total daily energy scattergram. A preliminary energy comparison is shown in figure 4.8. Based on the scatter below the $y = x$ line, it was determined that the cloud cover forecasts were conservatively higher than actual cloud cover. Data inspection also revieled cloud cover forecasted on clear days. This is in agreement with other studies and makes logical sense considering this forecast is intended as an estimate of visibility for aviation.

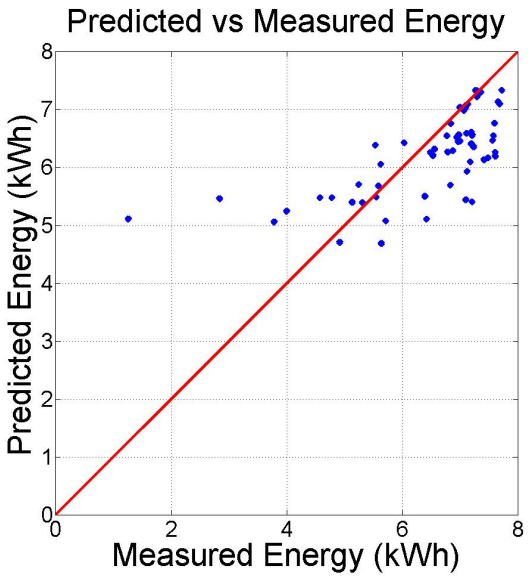

Figure 4.8: Measured vs. Predicted Energy per day; over-predicted cloud cover evident in the scattering below the $y = x$ line.

4.2 Optimization

After these lessons learned, the eight scenarios discussed were optimized over a full year's data. The results for each scenario are presented in order of degrees of freedom, first for equations 3.5 & 3.7 which include cloud cover forecasts alone and then followed by equations 3.6 & 3.8 which include both cloud cover and relative humidity. It is apparent that this order by rigor also presents results with improving annual (complete data set) RMS error.

4.2.1 Cloud Cover Only Correlation

Annual Optimization

The annually optimized cloud cover only correlation was the initial and simplest method attempted. As expected, the method's simplicity yielded the largest RMS error for both the linear and power law correlations. The energy scattergram for the linear equation (EQ. 3.5) is shown in figure 4.9.

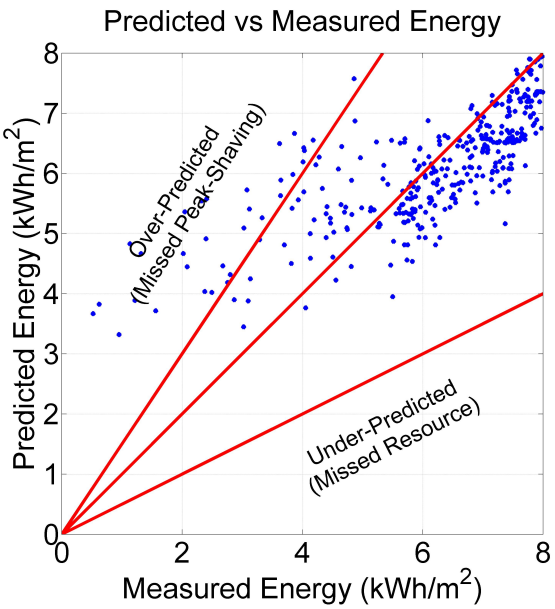

Figure 4.9: Measured vs. predicted daily insolation scattergram for annual optimization of EQ. 3.5

The scattergrams for each scenario change only gradually with each small change in RMS error. For the highest contrast comparison, only the best performing scenario, equation 3.8 under monthly optimization, will be shown in the results. Scattergrams for all remaining scenarios can be referenced in the appendix.

Though each scenario is optimized to minimize either annual or monthly RMS error, it is useful to look at the RMS error over the course of the day. This helps

one understand which times of the day experience a higher prediction error. Should a shifting plan depend on hourly blocks of energy throughout the day, this would provide added insight into potential deviation. The RMS error by hour is shown in figure 4.10.

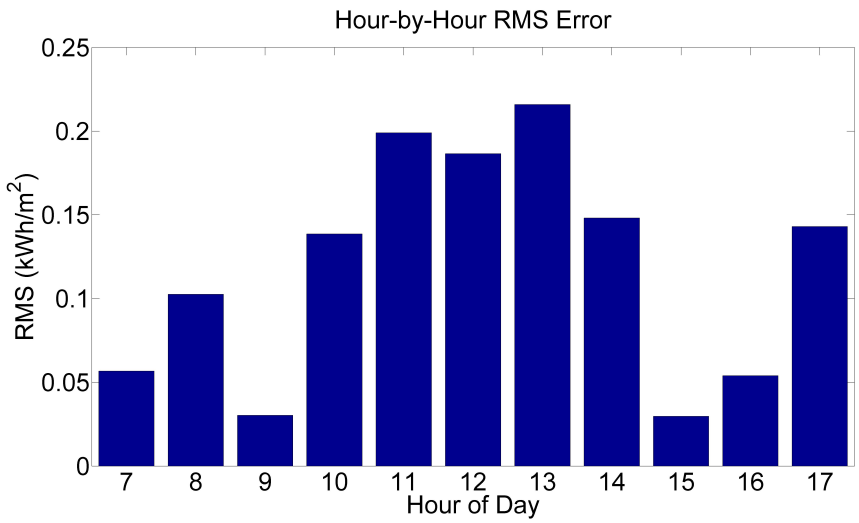

Figure 4.10: Hourly RMS error for daylight hours over entire year for annual optimization of EQ. 3.5

This plot shows hours of highest absolute error which is useful for determining which times of the day can affect a shifting schedule the most. This does not reflect how well the prediction is performing with respect to the measured insolation. The same chart for RMS error relative to measured insolation is shown in figure 4.11. Note that, relative to resource, the prediction performs best during the middle of the day but struggles in the morning and afternoon. This could be due to the increased attenuation of irradiance in the atmosphere due to increased airmass or cloud reflection.

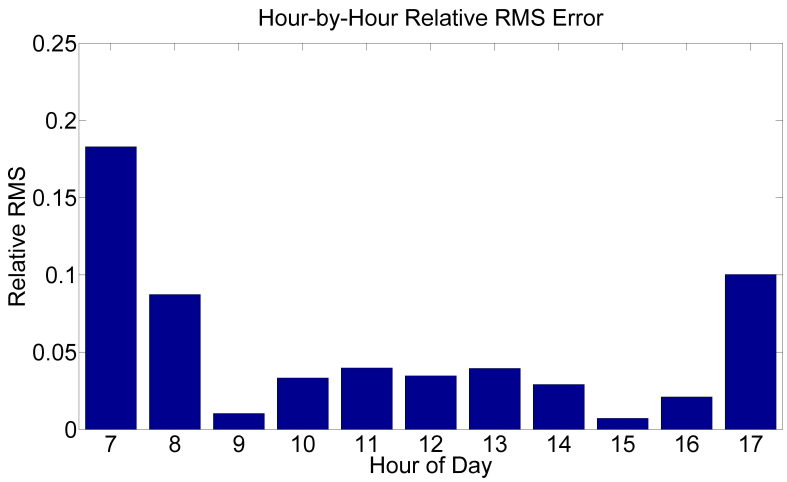

Figure 4.11: Hourly relative RMS error for daylight hours over entire year for annual optimization of EQ. 3.5

Utility customer load varies greatly from season to season as shown previously in figure 1.5. This varying load influences peak shaving planning further so it is beneficial to understand the monthly RMS error. Figure 4.12 suggests a higher RMSE in colder months than in warmer. This could be due to added PV losses from snow collecting on modules or increased diffuse irradiance reflected off of ground snow.

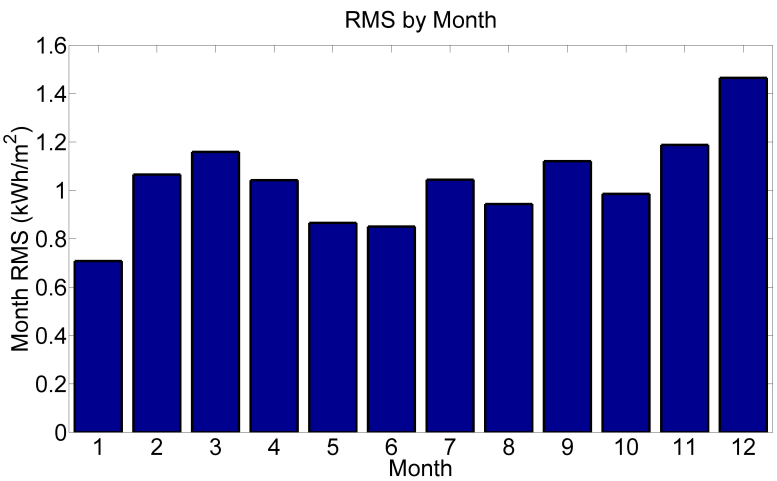

Figure 4.12: Daily RMS error during each month for annual optimization of EQ. 3.5

As with the hourly RMS error, it is important to understand the daily relative RMS error for particular months. It is apparent in figure 4.13 that the prediction performed very poorly with a relative RMS error for daily insolation at about 150%. Looking at past weather reports, December 2011 was the Albuquerque's 3rd wettest December (as of January 2012) on record in terms of precipitation [55]. Snowfall could have remained on modules causing a disproportionate decrease in insolation.

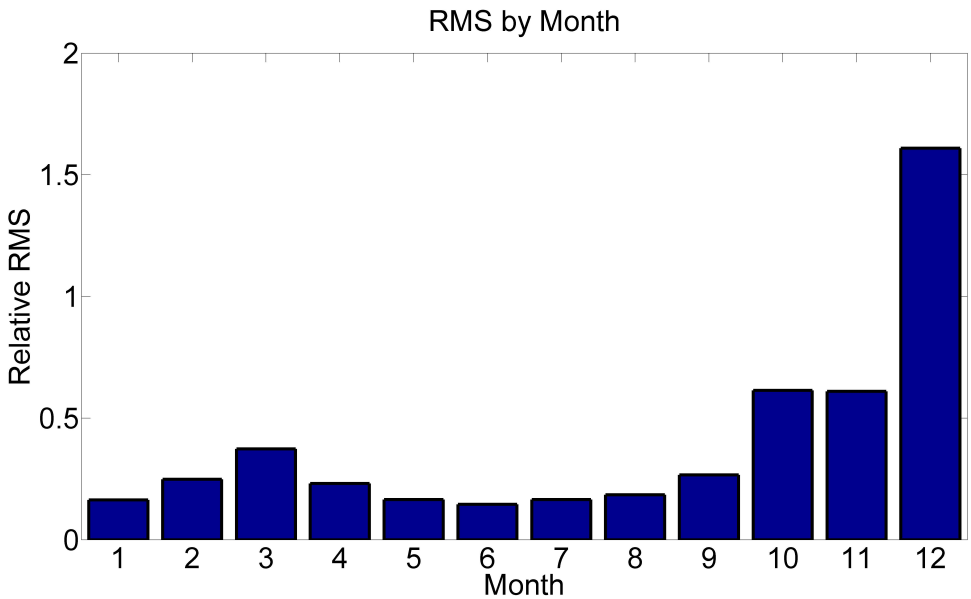

Figure 4.13: Daily relative RMS error during each month for annual optimization of EQ. 3.5

Coupling these two metrics together, we get the finer resolution in figure 4.14 showing hourly RMSE for each month individually. The error is consistently larger after solar noon which could be due to the near maximum potential resource along with a potentially higher uncertainty for the weather forecasts at the increased forecast horizon. Prevailing error from July to September could possibly be reflecting Albuquerque's particular afternoon monsoons. Unfortunately, as error viewing resolution increases, repeatability is also unlikely and distributions will change significantly due to varying weather patterns and droughts.

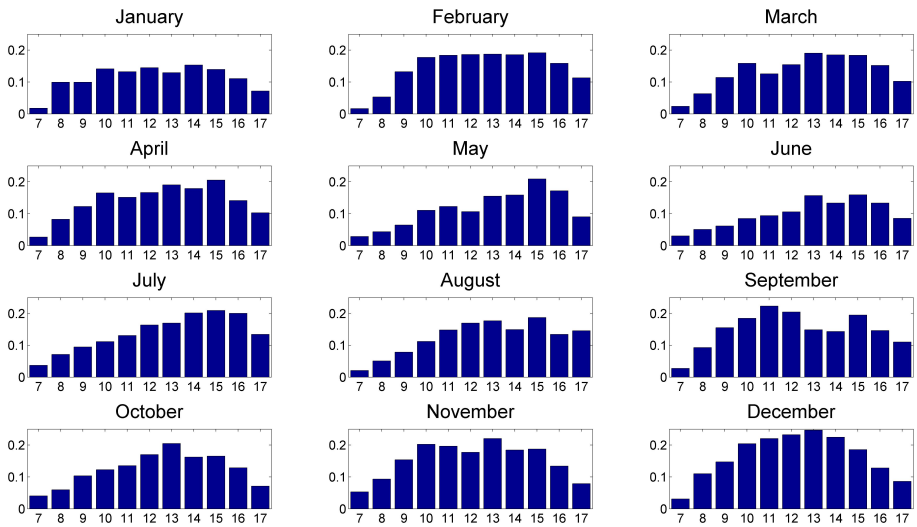

Figure 4.14: Hourly RMS error for daylight hours over each month for annual optimization of EQ. 3.5

The resulting annually optimized coefficients for both linear and power correlations (EQ. 3.5 & EQ. 3.7) are shown in table 4.1. The power coefficients are equal to one for linear correlation results. Between these two correlations alone it would appear the power law coefficient benefits performance.

Table 4.1: Optimized coefficients and RMS for annual correlation EQ. 3.5 & EQ. 3.7

Method	Month	b	B	Daily RMSE by Month (kWh/m^2)	Average Daily RMSE (kWh/m^2)
Linear	Jan.	0.43	-	0.7078	1.0528
	Feb.			1.0653	
	Mar.			1.1593	
	Apr.			1.0423	
	May			0.8657	
	June			0.8508	
	July			1.0439	
	Aug.			0.9437	
	Sept.			1.1209	
	Oct.			0.9854	
	Nov.			1.1879	
	Dec.			1.4654	
Power	Jan.	0.74	1.91	0.5805	0.9888
	Feb.			1.0429	
	Mar.			1.0653	
	Apr.			0.9714	
	May			0.8086	
	June			0.7146	
	July			1.1648	
	Aug.			0.9096	
	Sept.			1.1657	
	Oct.			0.8531	
	Nov.			1.1982	
	Dec.			1.1752	

Monthly Optimization

Monthly optimization yields unique coefficients which provide the best prediction for each month. This adds more degrees of freedom to the regression analysis which, as mentioned previously, could create the "illusion of predictability". One sign of this could be irregular or wildly varying coefficients from month to month. Both linear and power correlations show some signs of such behavior.

Some linear coefficients in the power correlation suggest the constrained maximum 100% correlation ($b = 1$) yielded the best results. In optimizations allowing linear coefficients to be larger than one, values for this and other scenarios increased to a maximum of about $b = 4$ causing power coefficients (if applicable) to change as well. These results were discarded once constraints were placed which prevented aphysical results under certain circumstances.

Table 4.2: Optimized coefficients and RMS for monthly correlation EQ. 3.5 & EQ. 3.7

Method	Month	b	B	Daily RMSE by Month (kWh/m^2)	Average Daily RMSE (kWh/m^2)
Linear	Jan.	0.42	-	0.7071	0.9733
	Feb.	0.43	-	1.0653	
	Mar.	0.50	-	1.1461	
	Apr.	0.40	-	1.0375	
	May	0.31	-	0.8111	
	June	0.24	-	0.7073	
	July	0.29	-	0.8418	
	Aug.	0.34	-	0.8863	
	Sept.	0.48	-	1.1061	
	Oct.	0.62	-	0.8651	
	Nov.	0.57	-	1.1327	
	Dec.	0.69	-	1.2095	
Power	Jan.	0.82	2.21	0.5744	0.9156
	Feb.	0.67	1.70	1.0410	
	Mar.	1.00	2.03	1.0149	
	Apr.	1.00	2.21	0.9508	
	May	0.53	1.66	0.7914	
	June	0.87	2.31	0.6985	
	July	0.32	1.20	0.8403	
	Aug.	0.54	1.69	0.8677	
	Sept.	0.51	1.08	1.1056	
	Oct.	1.00	1.85	0.6941	
	Nov.	0.67	1.25	1.1241	
	Dec.	0.87	1.74	1.1006	

4.2.2 Cloud Cover and Relative Humidity Correlation

Annual Optimization

In comparison to the previous annual optimization results in table 4.1, the linear coefficients for both the linear and power correlations increased to the maximum ($b = 1$) once the relative humidity multiplier was introduced. Though these values would have increased if unconstrained, the current result yielded improved annual and monthly RMSE values.

With relative humidity forecasts present, it is interesting to compare the power coefficients. In this case, the coefficients B and C suggest that relative humidity fractions have more of an effect because the fraction would decrease with increased power coefficient. This is counter-intuitive since cloud cover of any type can reflect far more radiation than water vapor can attenuate. It is possible that the relation between cloud cover and relative humidity offers some sort of cloud classification, but this cannot be verified.

Table 4.3: Optimized coefficients and RMS for annual correlation EQ. 3.6 & EQ. 3.8

Method	Month	b	B	C	Daily RMSE by Month (kWh/m^2)	Average Daily RMSE (kWh/m^2)
Linear	Jan.	1.00	-	-	0.6646	0.9806
	Feb.				1.0565	
	Mar.				1.0571	
	Apr.				1.1066	
	May				0.8317	
	June				0.7673	
	July				0.8503	
	Aug.				0.7804	
	Sept.				1.2225	
	Oct.				0.9636	
	Nov.				1.2522	
	Dec.				1.0410	
Power	Jan.	1.00	1.07	0.69	0.6762	0.9241
	Feb.				1.0224	
	Mar.				0.9303	
	Apr.				0.9709	
	May				0.8227	
	June				0.7190	
	July				0.9681	
	Aug.				0.7875	
	Sept.				1.0789	
	Oct.				0.8069	
	Nov.				1.1393	
	Dec.				1.0522	

Monthly Optimization

Much like the annual optimization for equation 3.6, the monthly optimization yielded many maximum linear coefficients. The RMSE changes only for the month of July giving a negligibly improved annual RMSE. Had this occurred with a coefficient less than the maximum, this could be interpreted as consistency in the prediction. However, it is likely that this resulted purely from the constraints set.

As expected, the scenario providing the most degrees of freedom performed the best. At an average daily RMSE of 0.8631 kWh/m^2, this method far outperforms the others tested. However, attention should be paid to the consistency of the coefficients. It is apparent that there is more fluctuation in coefficients in this method than the others.

Table 4.4: Optimized coefficients and RMS for monthly correlation EQ. 3.6 & EQ. 3.8

Method	Month	b	B	C	Daily RMSE by Month (kWh/m^2)	Average Daily RMSE (kWh/m^2)
Linear	Jan.	1.00	-	-	0.6646	0.9806
	Feb.	1.00	-	-	1.0565	
	Mar.	1.00	-	-	1.0571	
	Apr.	1.00	-	-	1.1066	
	May	1.00	-	-	0.8317	
	June	1.00	-	-	0.7673	
	July	0.99	-	-	0.8502	
	Aug.	1.00	-	-	0.7804	
	Sept.	1.00	-	-	1.2225	
	Oct.	1.00	-	-	0.9636	
	Nov.	1.00	-	-	1.2522	
	Dec.	1.00	-	-	1.0410	
Power	Jan.	0.92	2.10	0.18	0.5715	0.8631
	Feb.	1.00	1.27	0.62	1.0181	
	Mar.	1.00	0.74	0.69	0.8804	
	Apr.	1.00	1.23	0.46	0.9350	
	May	0.52	1.61	0.01	0.7913	
	June	1.00	2.29	0.02	0.6985	
	July	0.50	0.85	0.49	0.8259	
	Aug.	1.00	0.00	1.39	0.7089	
	Sept.	0.99	0.01	1.08	0.9684	
	Oct.	1.00	1.85	0.00	0.6941	
	Nov.	1.00	0.93	0.53	1.0877	
	Dec.	1.00	1.19	0.78	1.0345	

Though the best scenario results are questionable, it is interesting to view the resulting figure comparisons. Figure 4.15 shows considerable improvement for low

insolation days. Comparing to figure 4.9, note the movement in points for lower measured insolation. Points originally in the "over-predicted" region of the plot have dropped into the set of secondary lines. Days with more insolation change relatively little, which suggests the increased degrees of freedom are compensating for the prediction's inability to accurately predict for excessively cloudy days.

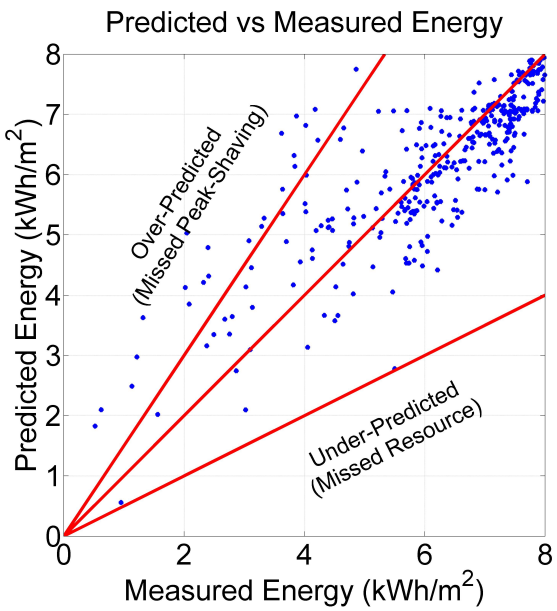

Figure 4.15: Measured vs. predicted daily insolation scattergram for monthly optimization of EQ. 3.8; compare to figure 4.9 noting movement of points with low measured insolation

The hourly RMSE shown in figure 4.16 also improves greatly. Comparing to figure 4.10, hours of the day associated with the lowest RMSE remain relatively unchanged, but hour blocks previously experiencing the highest RMSE are significantly reduced. As before, the hourly relative RMS error is shown in figure 4.17. Again, performance relative to measured resource is worst in morning and afternoon hours suggesting limitations during times of increased air mass.

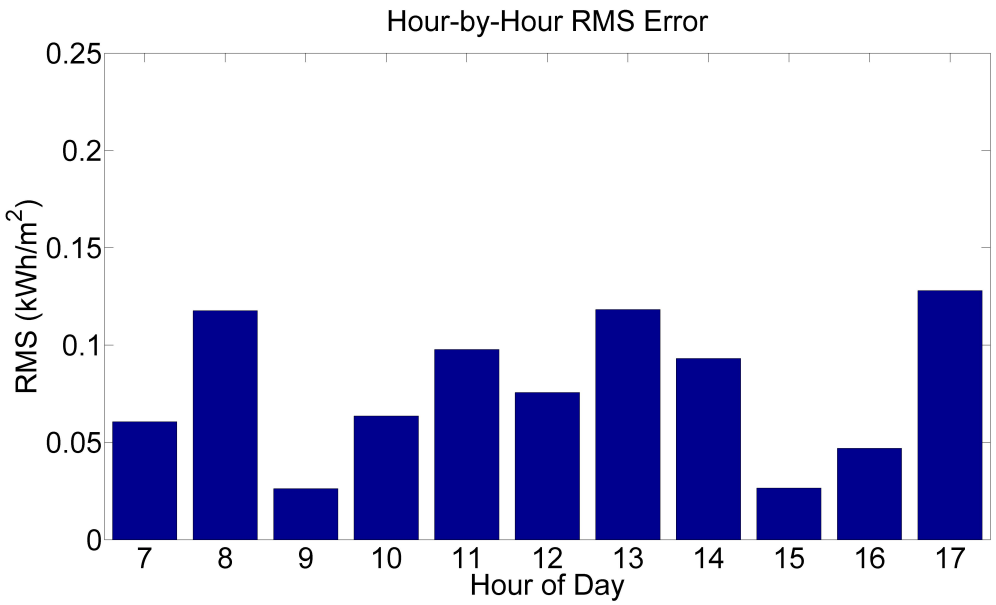

Figure 4.16: Hourly RMS error for daylight hours over entire year for monthly optimization of EQ. 3.8; compare to figure 4.10

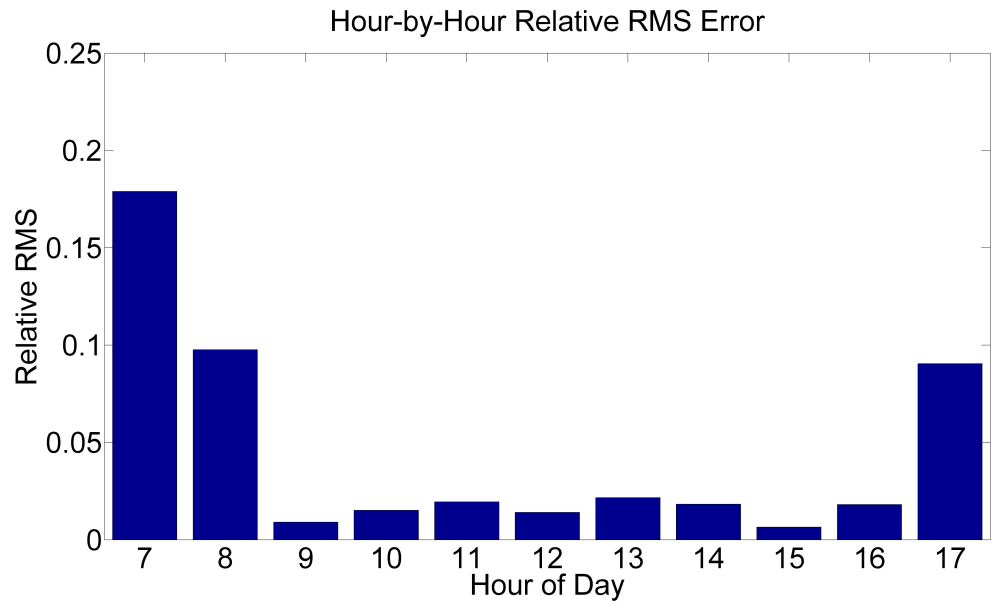

Figure 4.17: Hourly relative RMS error for daylight hours over entire year for monthly optimization of EQ. 3.8; compare to figure 4.11

The monthly RMSE plot also experienced some of this leveling as seen in figure 4.18. December saw the greatest improvement with other winter months seeing reduced RMSE as well. Seasonally, the increased degrees of freedom could be compensating for snow cover on sensors.

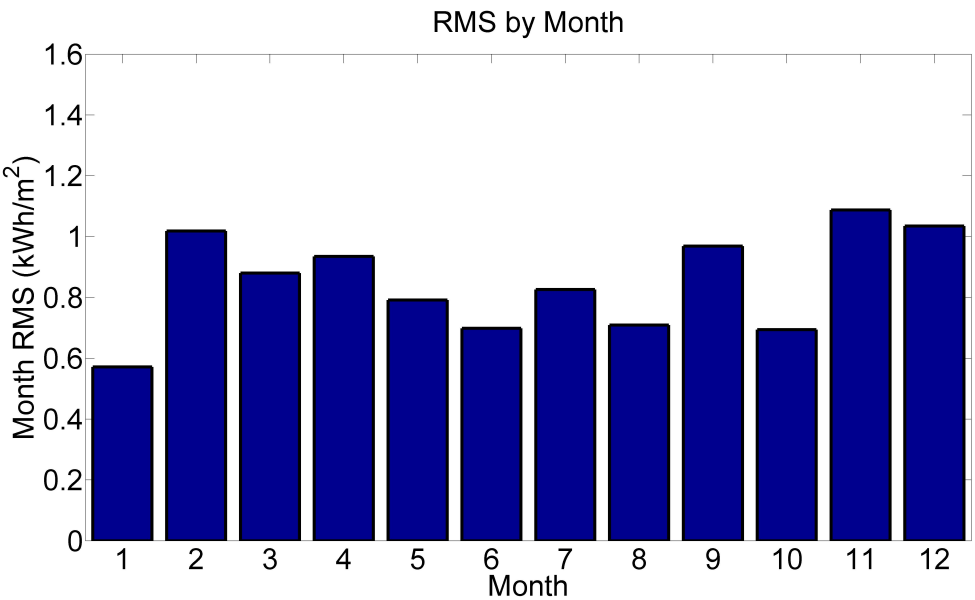

Figure 4.18: Daily RMS error during each month for monthly optimization of EQ. 3.8; compare to figure 4.12

Looking at the daily relative RMS errors for each month in figure 4.19, there is significant improvement in colder months. This improvement is undoubtedly due to the added degrees of freedom introduced by monthly optimization. However, it appears the snowfall experienced in December 2011 limits prediction performance despite added degrees of freedom.

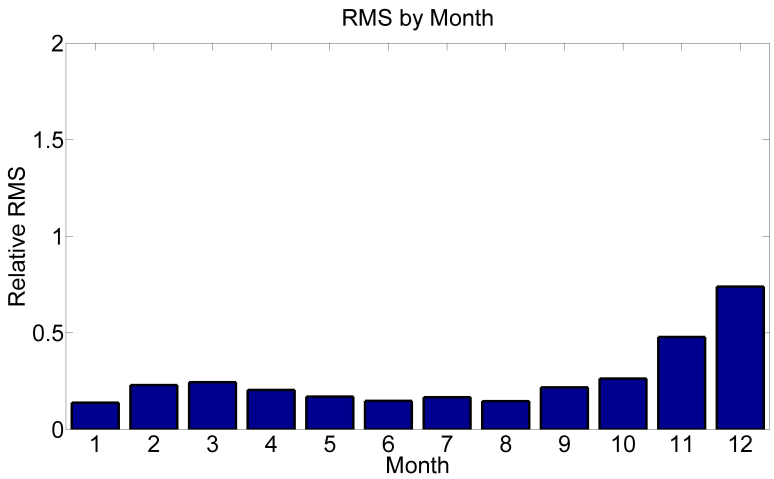

Figure 4.19: Daily relative RMS error during each month for monthly optimization of EQ. 3.8; compare to figure 4.13

This theory, however, would be most evident in the last figure showing hourly RMSE by month in figure 4.20. Significant improvement in the morning when snow and frost could covering the sensors collecting irradiance data is not apparent.

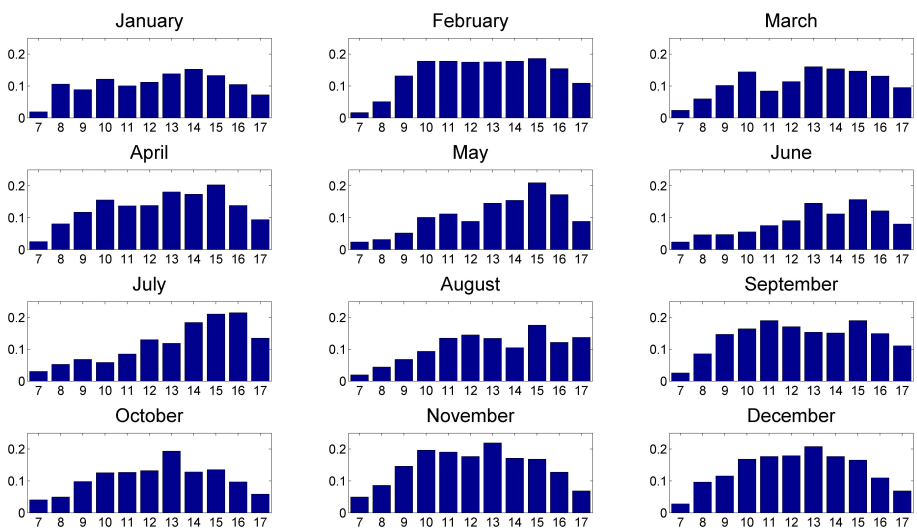

Figure 4.20: Hourly RMS error for daylight hours over each month for monthly optimization of EQ. 3.8; compare to figure 4.14

4.3 Coefficient Accuracy and Model Significance

Some of the results, particularly with respect to coefficient consistency, suggest the possibility of an unstable correlation. When performing numerical optimization, it is possible to converge on local minimums as opposed to the true minimum. One way to make sure the true optimized coefficients are obtained is to three dimensionally plot the error against the range of possible power coefficient values. Once represented graphically, one can visually inspect the nature of the error with respect to the regression. Figure 4.21 shows this for the scenario presented in table 4.3.

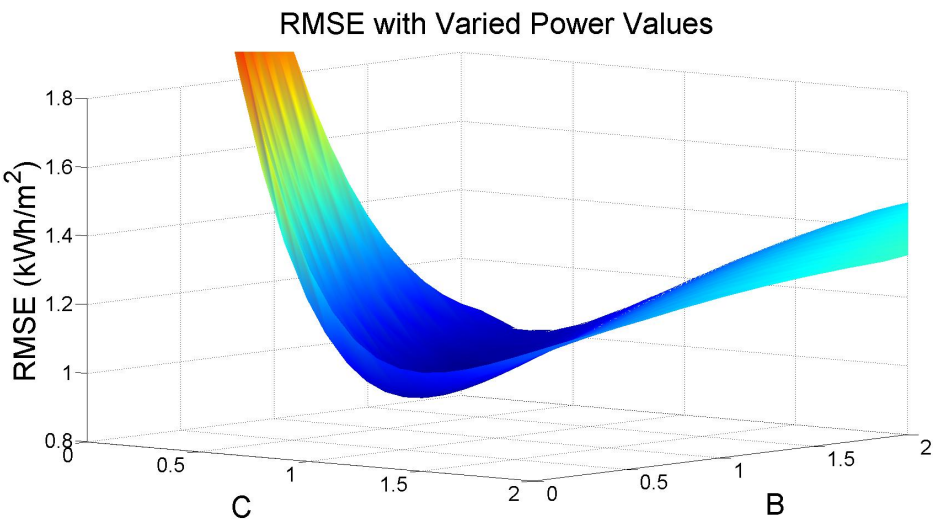

Figure 4.21: RMSE for span of B and C power coefficient values; note that optimal coefficient values occur at an absolute and not local minimum.

If ripples or a wavy surface were present, this would be a sign of an unstable relationship and also cause reason to doubt results. This plot, however, shows a true minimum and suggests a stable model.

It is also important to check whether or not the prediction is yielding statistically significant results or not. It is possible that the prediction method is providing results which are close to observed data purely by chance. For comparison, a prediction

based on randomly generated clear sky index was created and checked for RMS errors. The random prediction performed with an irradiance RMSE of 413 W/m^2 and an insolation RMSE of 2.9423 kWh/m^2. The significant advantage of all eight scenarios presented here over a random prediction shows the results yielded are statistically significant.

4.4 Comparison to Persistence

As stated in the "sample methods" section, persistence is an inexpensive, easy to implement method for predicting next day resource, though it has varied performance depending on location and season. Nonetheless, persistence offers a means of comparison to the methods here. For the same time period of irradiance data used for the regression analysis, the persistence forecasted insolation scattergram is shown in figure 4.22.

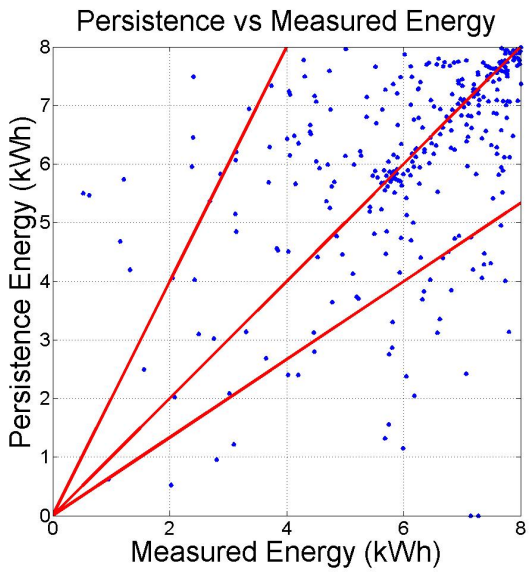

Figure 4.22: Persistence forecast energy scattergram Oct. 1, 2011 - Sept. 30, 2012

The scattergram is much more dispersed than even the least accurate scenario tested here which shows the high day to day variability of surface radiation in Albuquerque, NM. The resulting average daily insolation RMSE from this prediction was 1.5371 kWh/m^2.

4.5 Comparison to Other Methods

Despite being the intended use of day-ahead (or more) resource predictions for an estimate of energy, most if not all of the best known prediction methods measure their performance in MBE, RMSE or relative root mean square error (rRMSE) of irradiance. Though the correlations described here are optimized to minimize the RMSE of the predicted insolation, comparison can be made to these other methods in terms of irradiance RMSE as shown in table 4.5. These results from a study previous mentioned cover performance statistics for the National Digital Forecast Database (NDFD), European Centre for Medium-Range Weather Forecasts (ECMWF) and Global Forecast System (GFS) irradiance predictions. Because performance metrics for the *Solar Anywhere* forecast were available for the same locations, they are also presented.

Table 4.5: Irradiance prediction RMSE (W/m^2) for various other methods [56]

Site	NDFD	ECMWF	GFS/WRF	Solar Anywhere
Desert Rock, NV	96	87	105	139
Boulder, CO	167	162	223	189
Goodwin Creek, MS	149	136	190	164

Presented in the same order as the insolation RMS error results shown previously, the irradiance RMS errors are shown in table 4.6. Considering the climate type in Albuquerque, NM is somewhere between Desert Rock and Boulder, it would seem that the methods described in this study are obsolete with exception, possibly, to

the GFS/WRF method. However, these are irradiance RMS errors for coefficients optimized for insolation prediction. If irradiance optimization was performed, better irradiance RMS errors would undoubtedly be possible, but insolation predictions calculated from these data would be less accurate.

Table 4.6: Resulting annual irradiance RMSEs for eight scenarios

Input Data	Optimization Resolution	Correlation Type	Annual Irradiance RMSE (W/m^2)
%CC Only	Annual	Linear	183
		Power	180
	Monthly	Linear	179
		Power	176
%CC & RH	Annual	Linear	177
		Power	174
	Monthly	Linear	177
		Power	172
-	-	Persistence	261

Overall, these values suggest inferior performance in comparison to the methods in table 4.5. This is expected partly because the method described in this study does not consider added factors such as aerosols and other atmospheric constituents. Moreover, the optimization for insolation allows deviation in the minute-resolution irradiance prediction.

4.6 Performance for Varying Cloudiness

As can be seen in figures 4.9 and 4.15, the scenarios presented display reduced performance for days with lower recorded resource. To aid in determining the method's ability to predict insolation for varying degrees of cloudiness, days were separated based on recorded insolation as a percentage of clear day resource. The average daily insolation RMSE for each percentage category is shown in table 4.7.

Table 4.7: RMSE for days experiencing stated percent of clear day resource; note decreased performance with decrease in measured resource.

		%CC Only				%CC & RH			
		Annual		Monthly		Annual		Monthly	
%	days	Linear	Power	Linear	Power	Linear	Power	Linear	Power
0-20	4	3.1396	2.0889	1.9215	1.3224	2.1140	1.7383	2.1140	1.2129
20-40	13	2.6394	2.3790	2.1914	2.0203	2.4180	2.0506	2.4180	1.8419
40-60	27	1.8418	1.9004	1.8469	1.8973	2.1363	1.8134	2.1374	1.7802
60-80	56	0.8073	1.0112	0.8573	0.9237	1.1923	0.9696	1.1927	0.8754
80-100	211	0.7642	0.6941	0.7124	0.6449	0.4659	0.6501	0.4650	0.6059

The table makes several notable characteristics visible. First, each scenario's performance is significantly reduced with cloudier days but is typically worst for days experiencing 20-40% of clear day insolation. Next, with the exception of the monthly linear scenario using percent cloud cover and relative humidity (column second from right), the prediction improves with the added weather forecast, power correlation, and monthly optimization. Note that the exception scenario was also limited by the constraints set for coefficients (as seen in table 4.4) making it nearly identical to the annual linear scenario (column fourth from right, table 4.3). Finally, the table's data reveal why the optimization was biased toward clearer days. The number of days experiencing a particular percentage of resource decreases with decreased resource and, therefore, increased cloud cover. Nearly two-thirds of the days experience close to clear day insolation.

The over-abundant clear days may be altering interpretation of the scattergrams particularly, so the lowest and highest performing scenarios' scattergrams are shown in figure 4.23 with days experiencing 80-100% of clear day insolation removed. Similarly, figure 4.24 shows the persistence prediction with days experiencing 80-100% of clear day insolation removed. Note the significant advantage of either scenario of persistence in predicting cloudy day insolation.

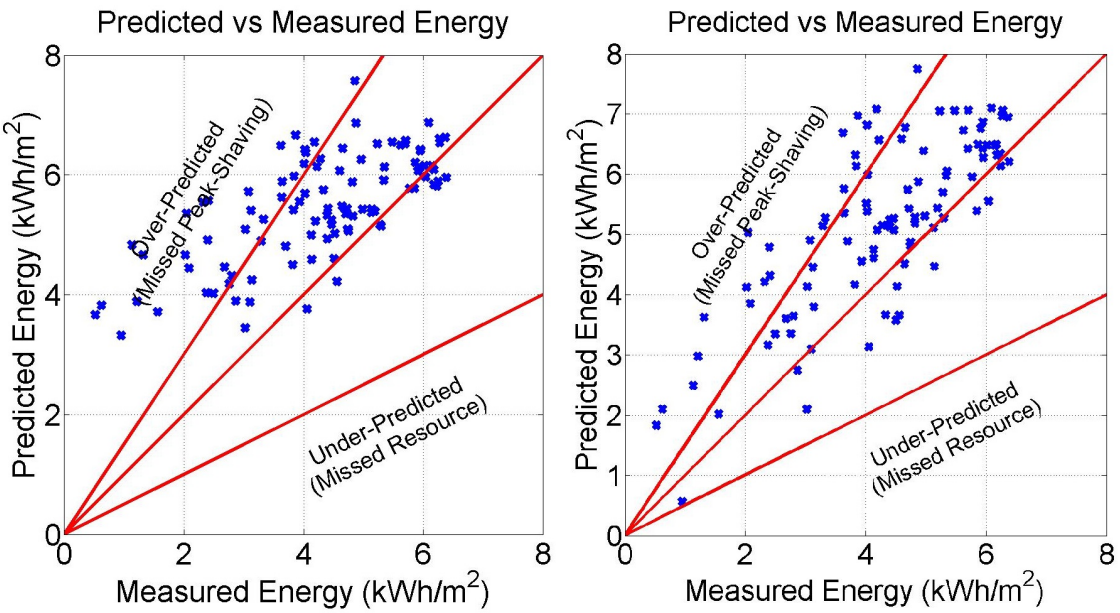

Figure 4.23: Measured vs. predicted insolation scattergrams for the lowest (left) and highest (right) performing scenarios with days experiencing 80-100% clear day insolation removed.

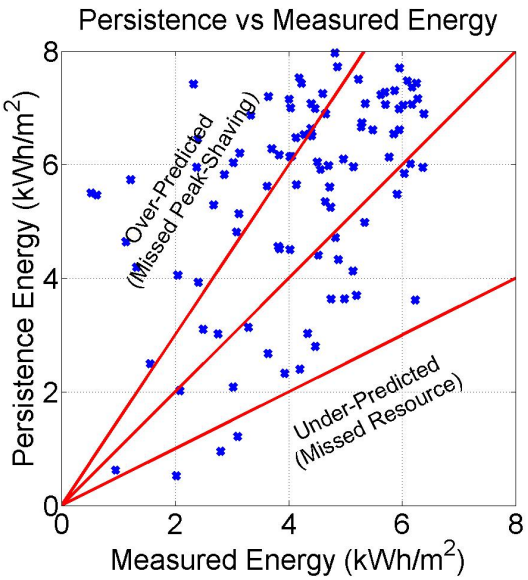

Figure 4.24: Measured vs. predicted insolation scattergram for persistence prediction with days experiencing 80-100% clear day insolation removed.

Comparing to table 4.7, table 4.8 shows the average daily insolation RMSE for the same percentage category days for the persistence prediction. As with the eight scenarios shown in table 4.7, the prediction performance decreases with increased cloud cover resulting in decreased percentage of clear day resource.

Table 4.8: Persistence forecast RMSE for days experiencing stated percent of clear day resource; note decreased performance compared to all scenarios shown in table 4.7.

%	days	Persistence
0-20	4	3.8948
20-40	13	2.9400
40-60	27	2.4199
60-80	56	1.4678
80-100	211	1.3696

Chapter 5

Conclusions and Suggested Future Work

Based on the results obtained for the scenarios described, all correlations presented here can provide a day-ahead insolation prediction better than what is probable using a persistence prediction. Additionally, one correlation yielded an average daily insolation RMSE of 0.8631 kWh/m^2 though it is suspected this is due to increased degrees of freedom and may not be repeatable for subsequent years.

Utilities demand a high level of certainty for resource availability, making even the best-case performance unacceptable. To ensure firm resource peak shaving, the day-ahead forecast could be compensated by its known error, providing a factor of safety making it more likely that the energy storage resource will be available. Applying this factor of safety would result in a tendency for the energy storage system to be charged more than necessary, possibly losing next-day solar resource. Further improvement upon this and other day-ahead prediction methods would, thus, minimize resource loss for the sake of firming and maximize the benefits of PV power generation with battery energy storage.

It is also important to note that all performance metrics stated are the best-case scenarios for the correlations tested and will vary in accuracy from year to year. Therefore, possible future work includes applying the methods described here to other years' data to better understand the consistency of performance.

In real-time practice, one could see improved results if predicted hourly energy blocks are updated according to updated NWS forecasts for the current day. This would remove some uncertainty in the forecasts themselves (from increased forecast horizon) and make it possible to create a better shifting plan as needed.

There may also be room for improvement upon the best performance found here by implementing other NWS forecasts. For example, precipitation and temperature could be used to foresee next-day snow cover on the modules. This should be done with caution, however, since it would introduce even more degrees of freedom for the correlation and could potentially yield false results.

Finally, the results suggest the methods tested struggled most during the evenings when atmospheric attenuation is greatest. There may be potential for increased accuracy by performing regression analysis to optimize coefficients affecting clear-sky direct beam and diffuse irradiance components independently. It is hypothesized that diffuse irradiance would show far different behavior than direct beam with increased cloud cover.

References

[1] NERC NERC. Operating manual,glossary of terms used in reliability standards,[en línea].

[2] B Liscouski and W Elliot. Final report on the august 14, 2003 blackout in the united states and canada: Causes and recommendations. *A report to US Department of Energy*, 40:4, 2004.

[3] `http://www.kepler-engineering.com/kepler/business.html`.

[4] A Jimenez and J Deluane. A case study of the dispatchable photovoltaic peak shaving system at the shopko facility in green bay, wisconsin. Technical report, Electric Power Research Institute, Inc, 2004.

[5] Hussein Ibrahim and Adrian Ilinca. Techno-economic analysis of different energy storage technologies. 2013.

[6] `http://www.pnm.com/systems/docs/prosperity_energy_storage_factsheet2013.pdf`.

[7] Feng Cheng, Steve Willard, Jonathan Hawkins, Brian Arellano, Olga Lavrova, and Andrea Mammoli. Applying battery energy storage to enhance the benefits of photovoltaics. In *Energytech, 2012 IEEE*, pages 1–5. IEEE, 2012.

[8] Hussein Ibrahim, Adrian Ilinca, and Jean Perron. Energy storage system-scharacteristics and comparisons. *Renewable and Sustainable Energy Reviews*, 12(5):1221–1250, 2008.

[9] M Ortiz, H Barsun, H He, P Vorobieff, and A Mammoli. Modeling of a solar-assisted hvac system with thermal storage. *Energy and buildings*, 42(4):500–509, 2010.

[10] Ioannis Hadjipaschalis, Andreas Poullikkas, and Venizelos Efthimiou. Overview of current and future energy storage technologies for electric power applications. *Renewable and Sustainable Energy Reviews*, 13(6):1513–1522, 2009.

[11] Frank Kreith. *Principles of sustainable Energy*, volume 46. CRC Press, 2011.

[12] David MacKay. *Sustainable Energy-without the hot air*. UIT Cambridge, 2008.

[13] `http://www.efda.org/wpcms/wp-content/uploads/2011/07/CP81j-1677c-10-720x260.jpg`.

[14] `http://www.tva.gov/heritage/mountaintop/tempimages/pumpstor2.jpg`.

[15] D Manolakos, G Papadakis, D Papantonis, and S Kyritsis. A stand-alone photovoltaic power system for remote villages using pumped water energy storage. *Energy*, 29(1):57–69, 2004.

[16] OA Jaramillo, MA Borja, and JM Huacuz. Using hydropower to complement wind energy: a hybrid system to provide firm power. *Renewable Energy*, 29(11):1887–1909, 2004.

[17] Jay Johnson, Abraham Ellis, Atsushi Denda, Kimio Morino, Takao Shinji, Takao Ogata, and Masayuki Tadokoro. Pv output smoothing using a battery and natural gas-engine generator. Technical report, Sandia National Laboratories (SNL-NM), Albuquerque, NM (United States), 2013.

[18] Matthew Lave, Jan Kleissl, and Ery Arias-Castro. High-frequency irradiance fluctuations and geographic smoothing. *Solar Energy*, 86(8):2190–2199, 2012.

[19] Stephen Wilcox and C Gueymard. Spatial and temporal variability of the solar resource in the united states. *Washington, DC: NREL/DoE [National Renewable Energy Laboratory/Department of Energy]*, 2010.

[20] Detlev Heinemann, Elke Lorenz, and Marco Girodo. Forecasting of solar radiation. *) Solar energy resource management for electricity generation from local level to global scale. Nova Science Publishers, New York*, 2006.

[21] Edwin Louis Crow, Frances A Davis, and Margaret Waugh Maxfield. *Statistics manual: with examples taken from ordnance development*, volume 3369. Dover-Publications. com, 1960.

[22] J Armstrong. Illusions in regression analysis. *Available at SSRN 1969740*, 2011.

[23] Emre Soyer and Robin M Hogarth. The illusion of predictability: How regression statistics mislead experts. *International Journal of Forecasting*, 28(3):695–711, 2012.

[24] Harry R Glahn and Dale A Lowry. The use of model output statistics (mos) in objective weather forecasting. *Journal of applied meteorology*, 11(8):1203–1211, 1972.

[25] JS Jensenius and GF Cotton. The development and testing of automated solar energy forecasts based on the model output statistics (mos) technique. In *1st Workshop on terrestrial solar resource forecasting and on use of satellites for terrestrial solar resource assessment, Washington, DC*, 1981.

[26] Elke Lorenz, Johannes Hurka, Detlev Heinemann, and Hans Georg Beyer. Irradiance forecasting for the power prediction of grid-connected photovoltaic sys-

tems. *Selected Topics in Applied Earth Observations and Remote Sensing, IEEE Journal of*, 2(1):2–10, 2009.

[27] Richard Perez, Kathleen Moore, Steve Wilcox, David Renné, and Antoine Zelenka. Forecasting solar radiation–preliminary evaluation of an approach based upon the national forecast database. *Solar Energy*, 81(6):809–812, 2007.

[28] Hanne Breitkreuz, Marion Schroedter-Homscheidt, Thomas Holzer-Popp, and Stefan Dech. Short-range direct and diffuse irradiance forecasts for solar energy applications based on aerosol chemical transport and numerical weather modeling. *Journal of Applied Meteorology and Climatology*, 48(9):1766–1779, 2009.

[29] Fernando Ramos Martins, Enio Bueno Pereira, and Ricardo André Guarnieri. Solar radiation forecast using artificial neural networks.

[30] Soteris A Kalogirou. Artificial neural networks in renewable energy systems applications: a review. *Renewable and sustainable energy reviews*, 5(4):373–401, 2001.

[31] David Elizondo, Gerrit Hoogenboom, and RW McClendon. Development of a neural network model to predict daily solar radiation. *Agricultural and Forest Meteorology*, 71(1):115–132, 1994.

[32] Richard Perez, Sergey Kivalov, James Schlemmer, Karl Hemker Jr, David Renné, and Thomas E Hoff. Validation of short and medium term operational solar radiation forecasts in the us. *Solar Energy*, 84(12):2161–2172, 2010.

[33] `https://www.solaranywhere.com/Public/About.aspx`.

[34] Tom Stoffel, Dave Renné, Daryl Myers, Steve Wilcox, Manajit Sengupta, Ray George, and Craig Turchi. Concentrating solar power: Best practices handbook

for the collection and use of solar resource data (csp). Technical report, National Renewable Energy Laboratory (NREL), Golden, CO., 2010.

[35] John A Duffie and William A Beckman. *Solar engineering of thermal processes*. John Wiley & Sons, 2013.

[36] Richard E Bird and Roland L Hulstrom. Simplified clear sky model for direct and diffuse insolation on horizontal surfaces. Technical report, Solar Energy Research Inst., Golden, CO (USA), 1981.

[37] Stephen Wilcox. National solar radiation database 1991-2005 update: User's manual. Technical report, National Renewable Energy Laboratory (NREL), Golden, CO., 2007.

[38] `http://rredc.nrel.gov/solar/models/clearsky/`.

[39] Pierre Ineichen and Richard Perez. A new airmass independent formulation for the linke turbidity coefficient. *Solar Energy*, 73(3):151–157, 2002.

[40] JERRY AUTOR VENTRE et al. *Photovoltaic systems engineering*. CRC press, 2004.

[41] `http://www.novalynx.com/240-8101.html`.

[42] `http://www.powerfromthesun.net/Book/chapter02/chapter02.html`.

[43] C Fröhlich. History of solar radiometry and the world radiometric reference. *Metrologia*, 28(3):111, 1991.

[44] M Sengupta. Measurement and modeling of solar and pv output variability. In *Proc. Solar*, 2011.

[45] Dirk C Jordan and Sarah R Kurtz. Photovoltaic degradation ratesan analytical review. *Progress in Photovoltaics: Research and Applications*, 21(1):12–29, 2013.

[46] A Massi Pavan, A Mellit, and D De Pieri. The effect of soiling on energy production for large-scale photovoltaic plants. *Solar energy*, 85(5):1128–1136, 2011.

[47] Felipe A. Mejia and Jan Kleissl. Soiling losses for solar photovoltaic systems in california. *Solar Energy*, 95(0):357 – 363, 2013.

[48] William C Skamarock, Joseph B Klemp, Jimy Dudhia, David O Gill, Dale M Barker, Wei Wang, and Jordan G Powers. A description of the advanced research wrf version 2. Technical report, DTIC Document, 2005.

[49] Patrick Mathiesen and Jan Kleissl. Evaluation of numerical weather prediction for intra-day solar forecasting in the continental united states. *Solar Energy*, 85(5):967–977, 2011.

[50] Chi Wai Chow, Bryan Urquhart, Matthew Lave, Anthony Dominguez, Jan Kleissl, Janet Shields, and Byron Washom. Intra-hour forecasting with a total sky imager at the uc san diego solar energy testbed. *Solar Energy*, 85(11):2881–2893, 2011.

[51] Ting Chen, William B Rossow, and Yuanchong Zhang. Radiative effects of cloud-type variations. *Journal of climate*, 13(1):264–286, 2000.

[52] Michael J Moran, Howard N Shapiro, Daisie D Boettner, and Margaret Bailey. *Fundamentals of engineering thermodynamics*. Wiley. com, 2010.

[53] `http://s.campbellsci.com/documents/us/manuals/li200x.pdf`.

[54] Scott Kuszamaul, Abraham Ellis, Joshua Stein, and Lars Johnson. Lanai high-density irradiance sensor network for characterizing solar resource variability of mw-scale pv system. In *Photovoltaic Specialists Conference (PVSC), 2010 35th IEEE*, pages 000283–000288. IEEE, 2010.

[55] `http://www.srh.noaa.gov/abq/?n=climonhigh2011annual-tempprecipabq`.

[56] J Remund, R Perez, and E Lorenz. Comparison of solar radiation forecasts for the usa. In *Proc. of the 23rd European PV Conference*, pages 1–9, 2008.

Appendix A

Appendix

A.1 RMSE figures for alternate scenarios

A.1.1 CC Only Annual Optimization for Power Correlation

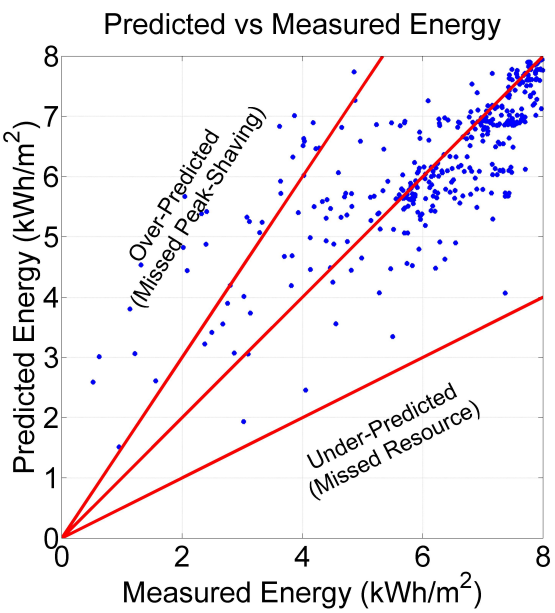

Figure A.1: Measured vs. predicted daily insolation scattergram for annual optimization of EQ. 3.7

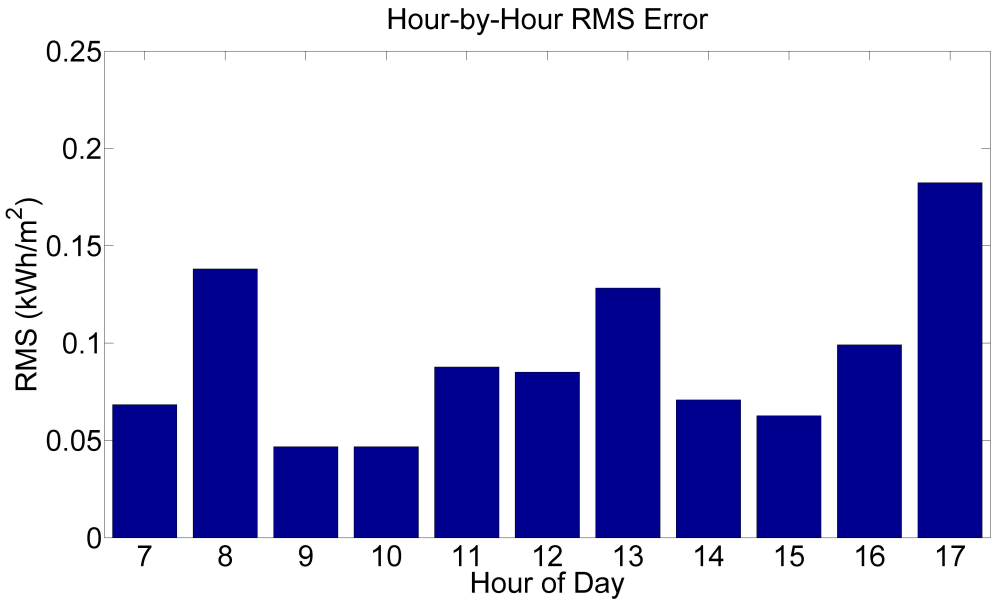

Figure A.2: Hourly RMS error for daylight hours over entire year for annual optimization of EQ. 3.7

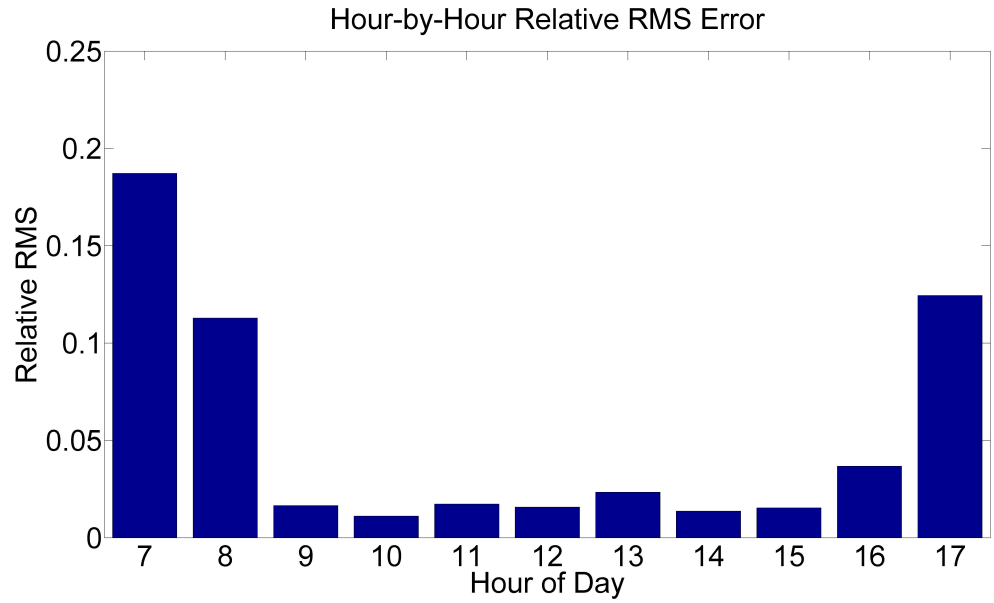

Figure A.3: Hourly relative RMS error for daylight hours over entire year for annual optimization of EQ. 3.7

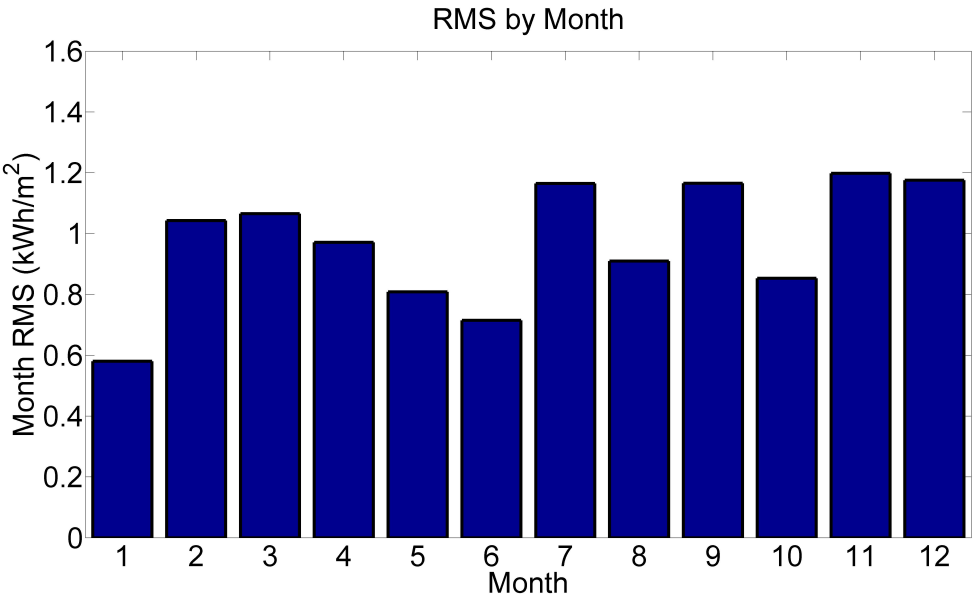

Figure A.4: Daily RMS error during each month for annual optimization of EQ. 3.7

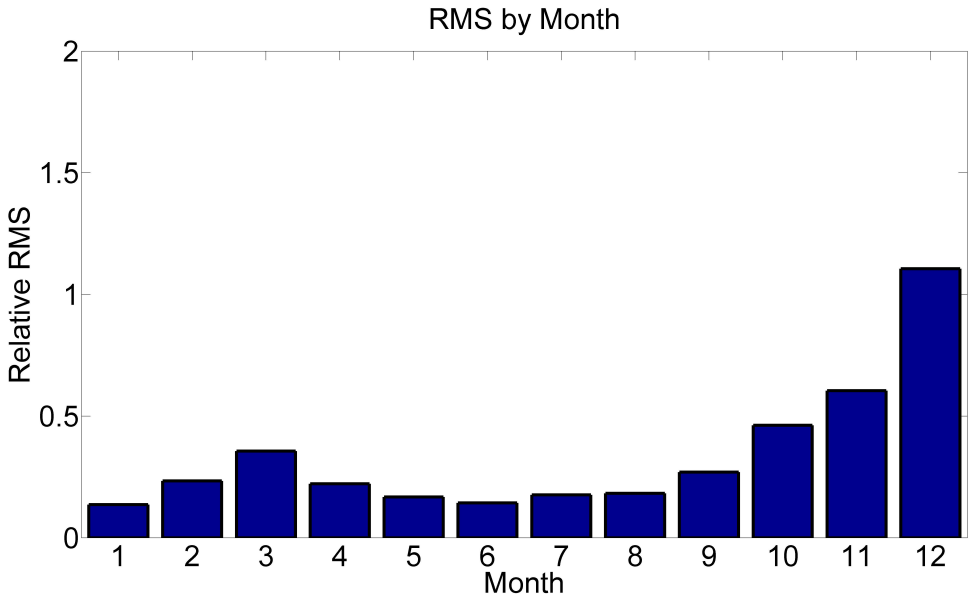

Figure A.5: Daily relative RMS error during each month for annual optimization of EQ. 3.7

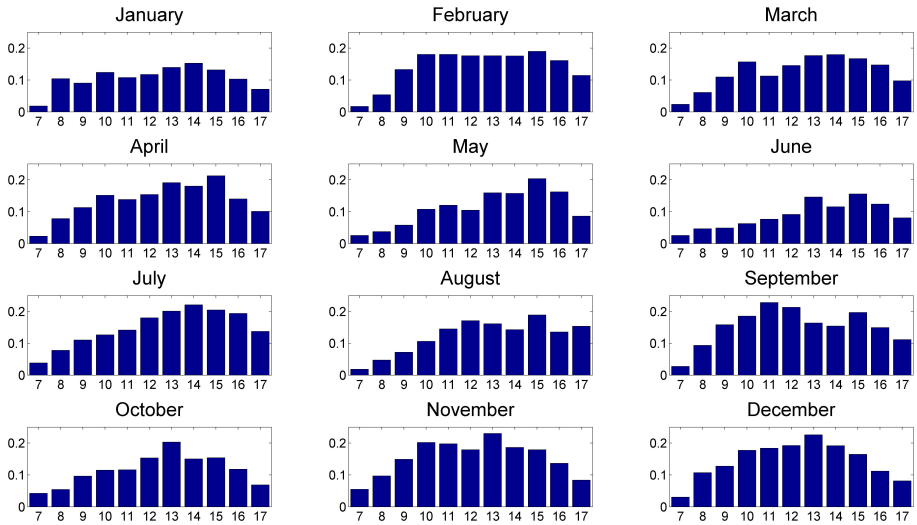

Figure A.6: Hourly RMS error for daylight hours over each month for annual optimization of EQ. 3.7

A.1.2 CC Only Monthly Optimization for Linear Correlation

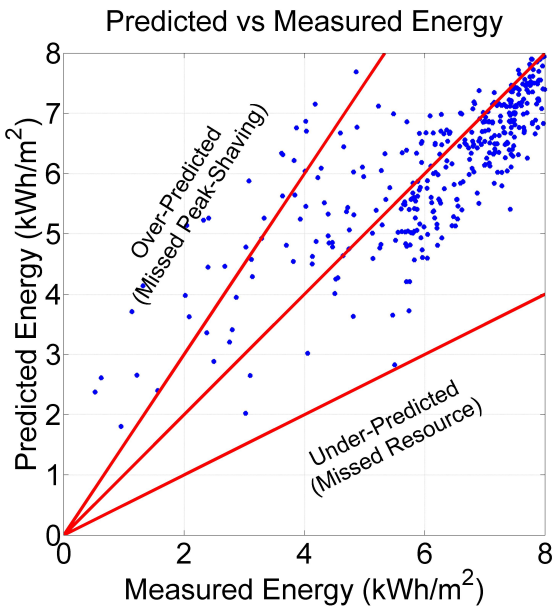

Figure A.7: Measured vs. predicted daily insolation scattergram for monthly optimization of EQ. 3.5

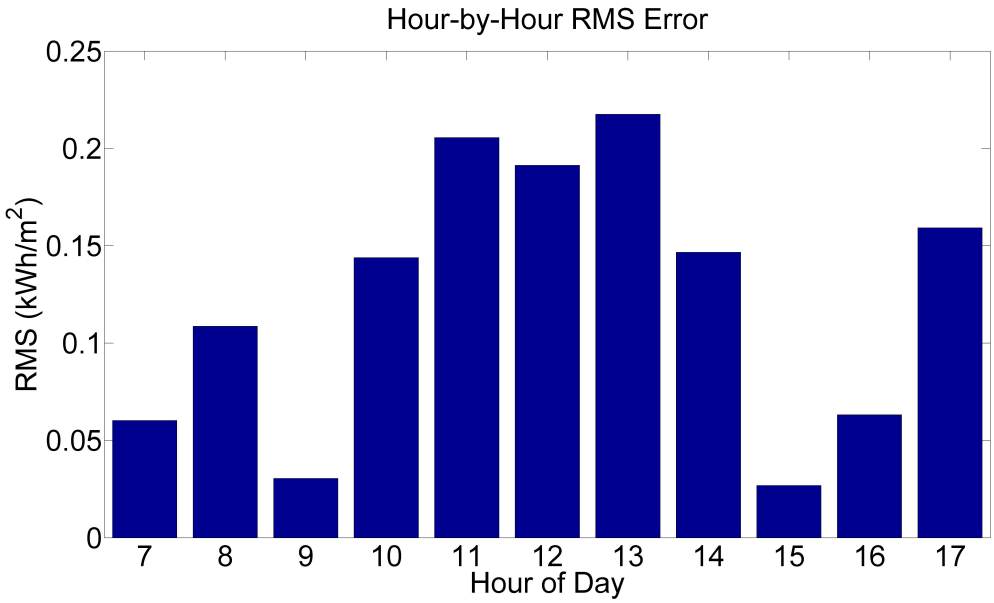

Figure A.8: Hourly RMS error for daylight hours over entire year for monthly optimization of EQ. 3.5

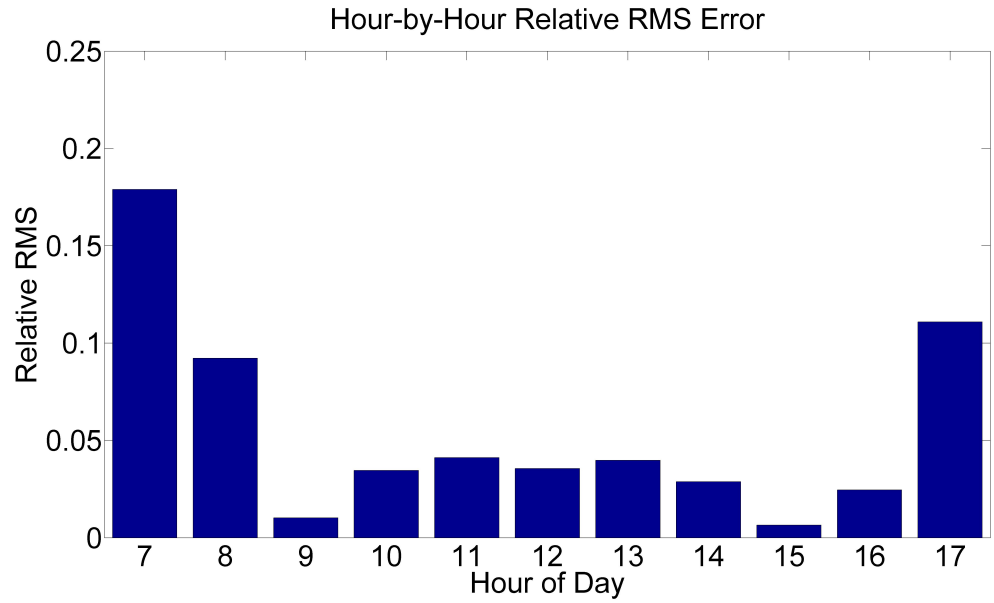

Figure A.9: Hourly relative RMS error for daylight hours over entire year for monthly optimization of EQ. 3.5

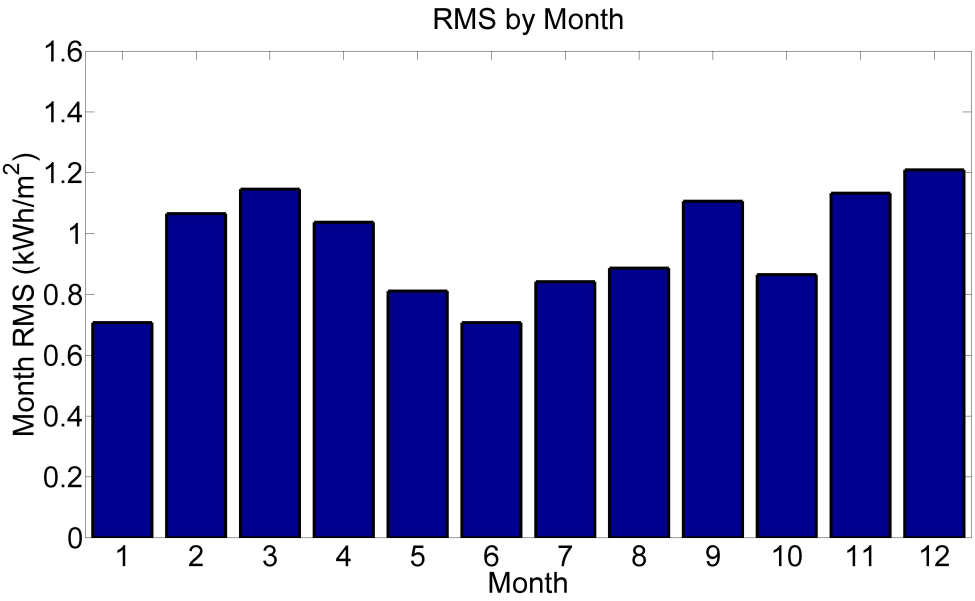

Figure A.10: Daily RMS error during each month for monthly optimization of EQ. 3.5

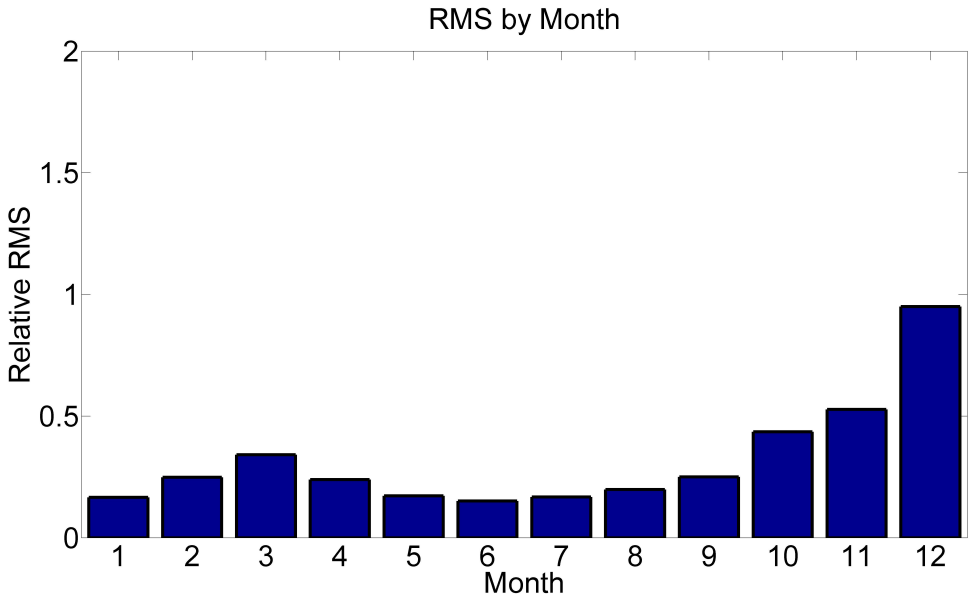

Figure A.11: Daily relative RMS error during each month for monthly optimization of EQ. 3.5

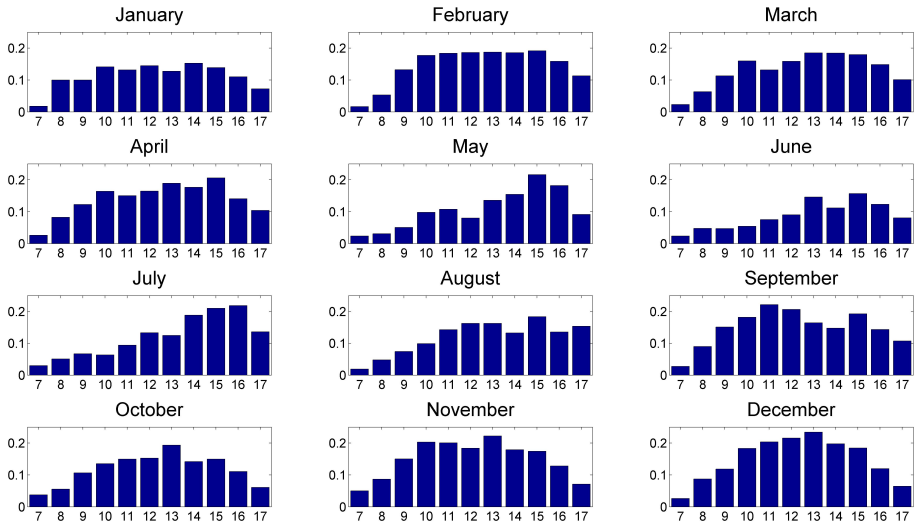

Figure A.12: Hourly RMS error for daylight hours over each month for monthly optimization of EQ. 3.5

A.1.3 CC Only Monthly Optimization for Power Correlation

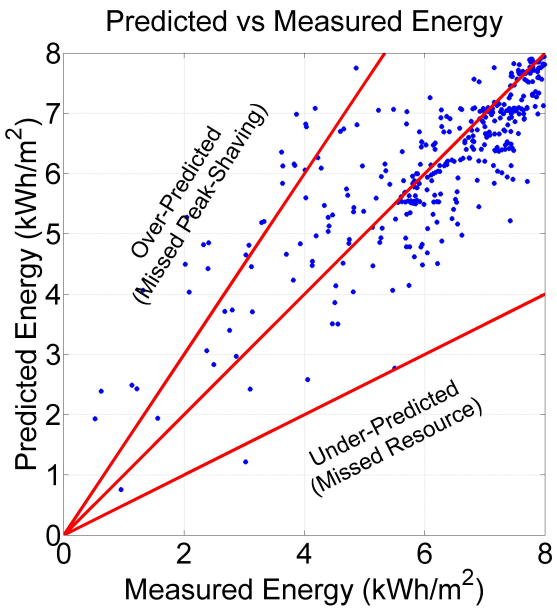

Figure A.13: Measured vs. predicted daily insolation scattergram for monthly optimization of EQ. 3.7

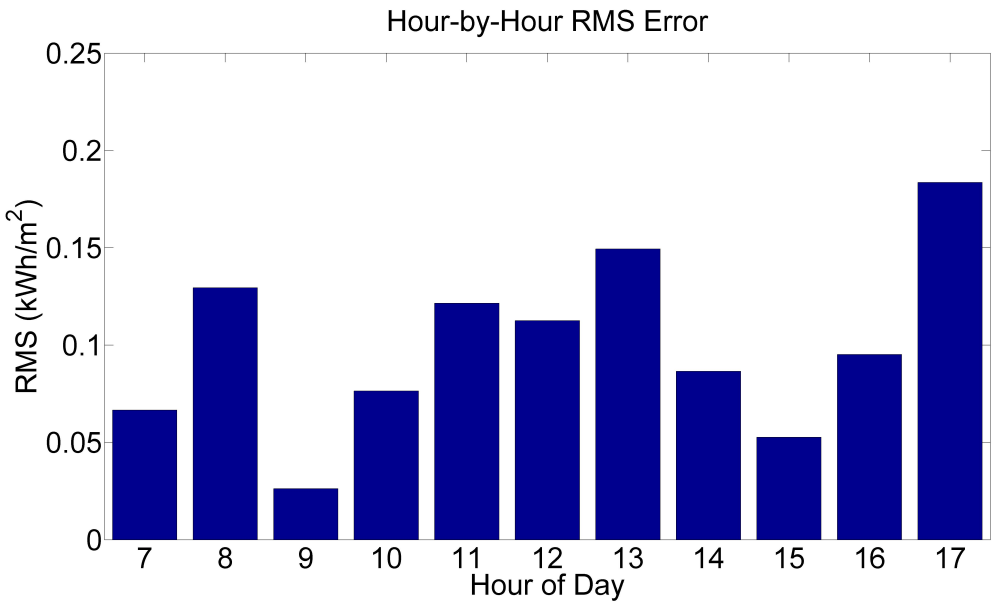

Figure A.14: Hourly RMS error for daylight hours over entire year for monthly optimization of EQ. 3.7

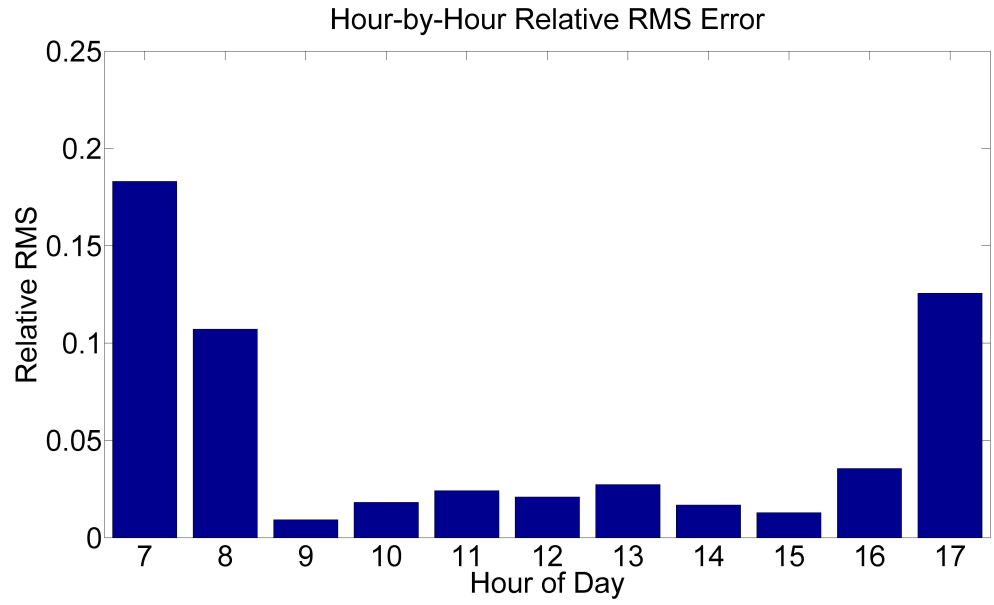

Figure A.15: Hourly relative RMS error for daylight hours over entire year for monthly optimization of EQ. 3.7

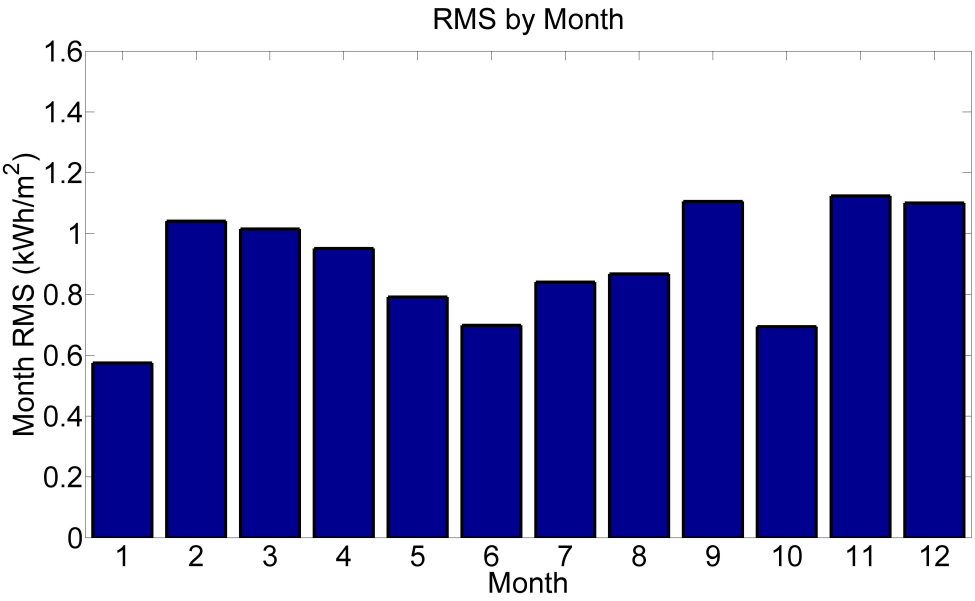

Figure A.16: Daily RMS error during each month for monthly optimization of EQ. 3.7

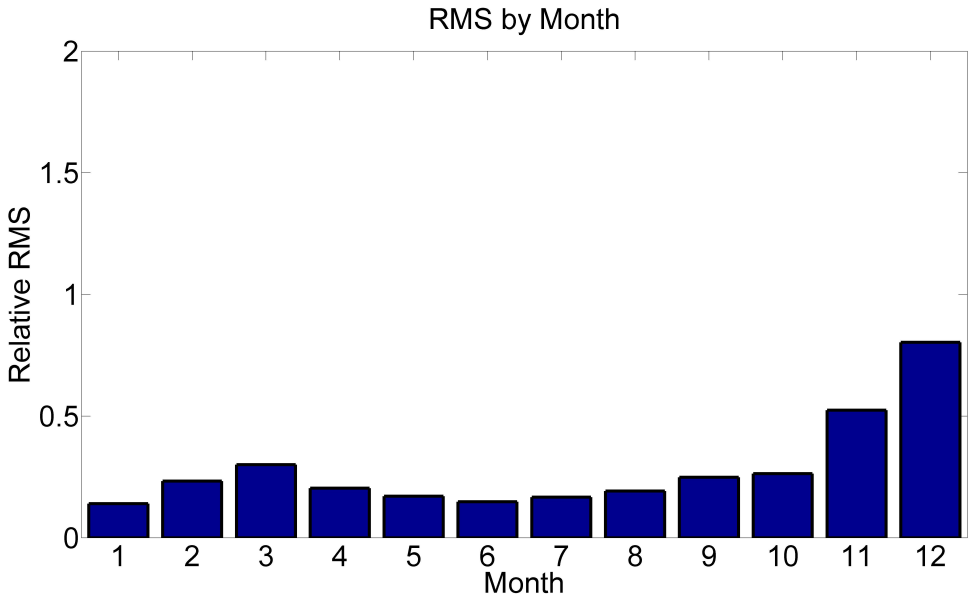

Figure A.17: Daily relative RMS error during each month for monthly optimization of EQ. 3.7

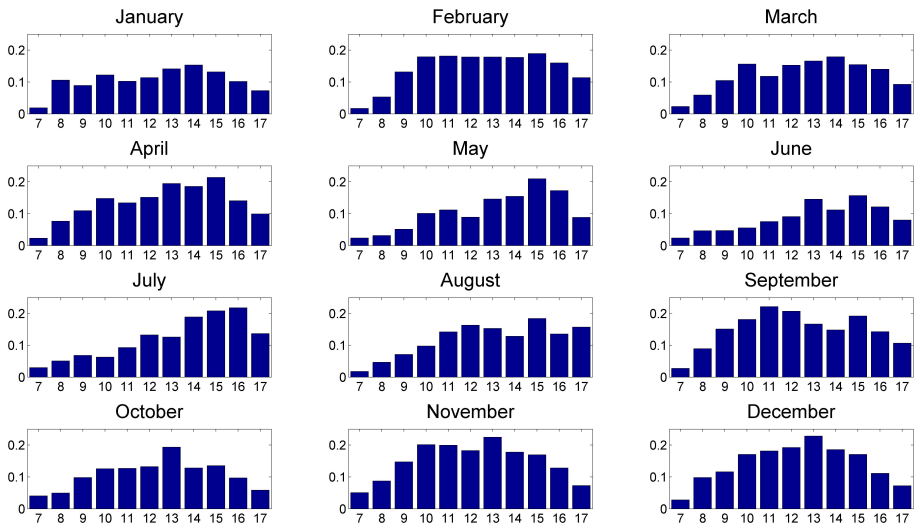

Figure A.18: Hourly RMS error for daylight hours over each month for monthly optimization of EQ. 3.7

A.1.4 CC and RH Annual Optimization for Linear Correlation

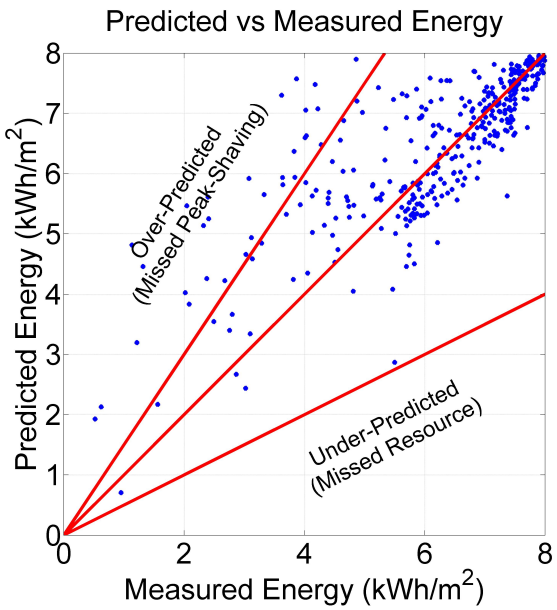

Figure A.19: Measured vs. predicted daily insolation scattergram for annual optimization of EQ. 3.6

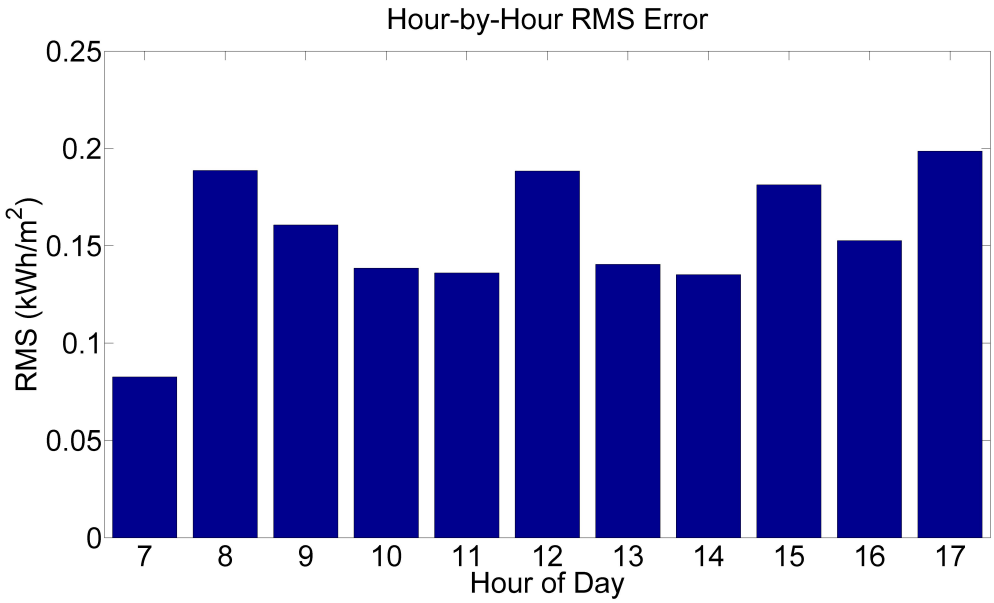

Figure A.20: Hourly RMS error for daylight hours over entire year for annual optimization of EQ. 3.6

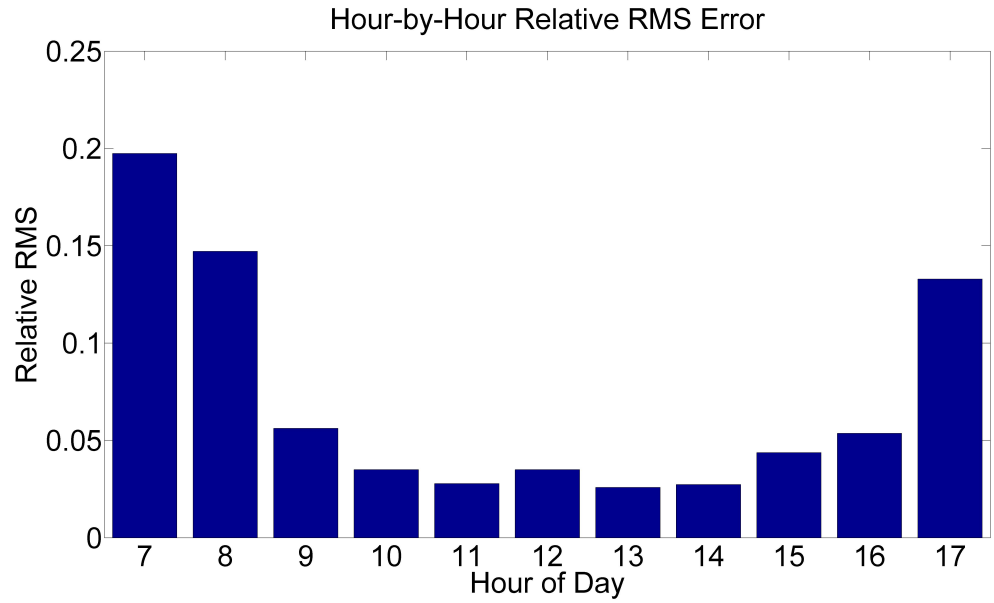

Figure A.21: Hourly relative RMS error for daylight hours over entire year for annual optimization of EQ. 3.6

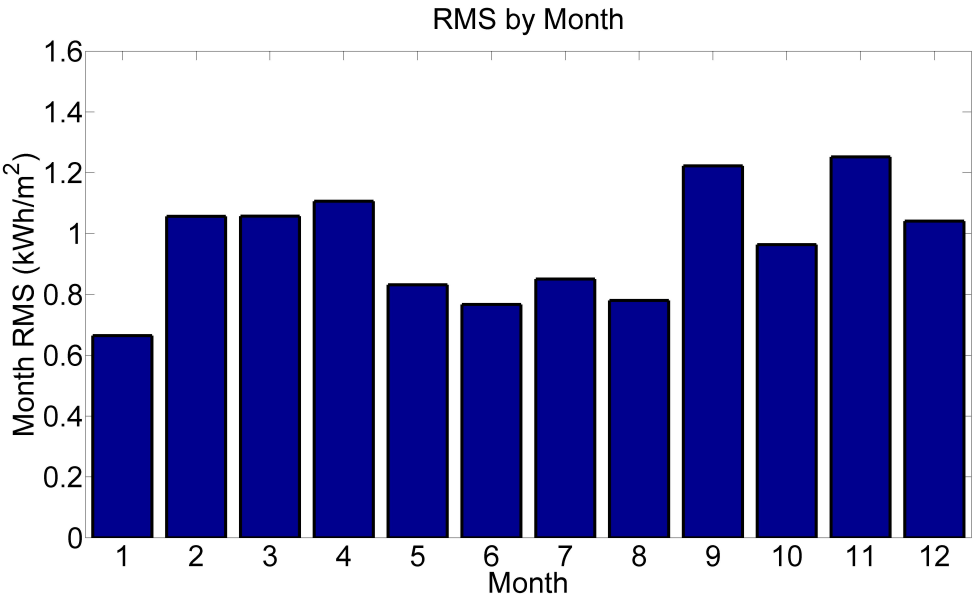

Figure A.22: Daily RMS error during each month for annual optimization of EQ. 3.6

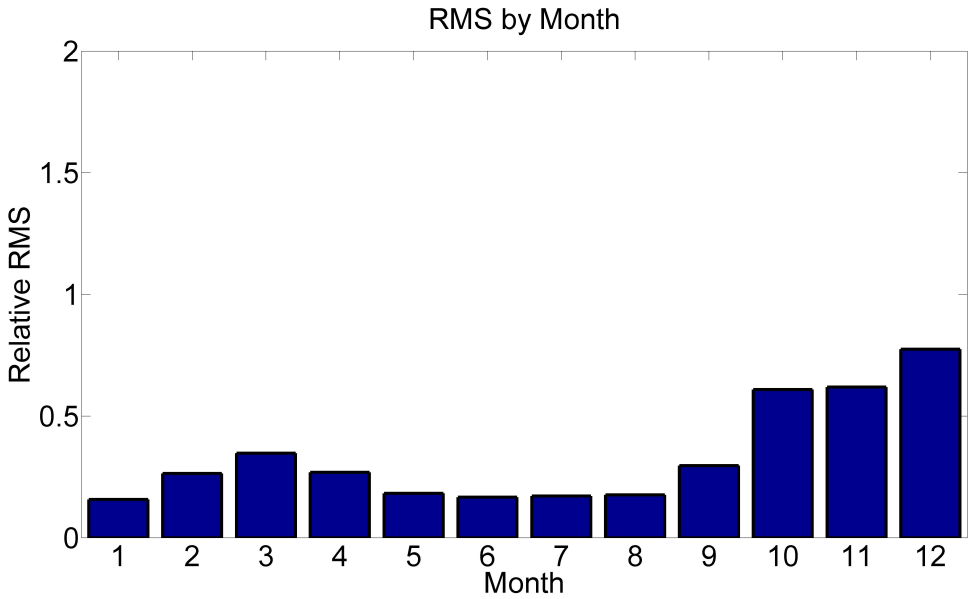

Figure A.23: Daily relative RMS error during each month for annual optimization of EQ. 3.6

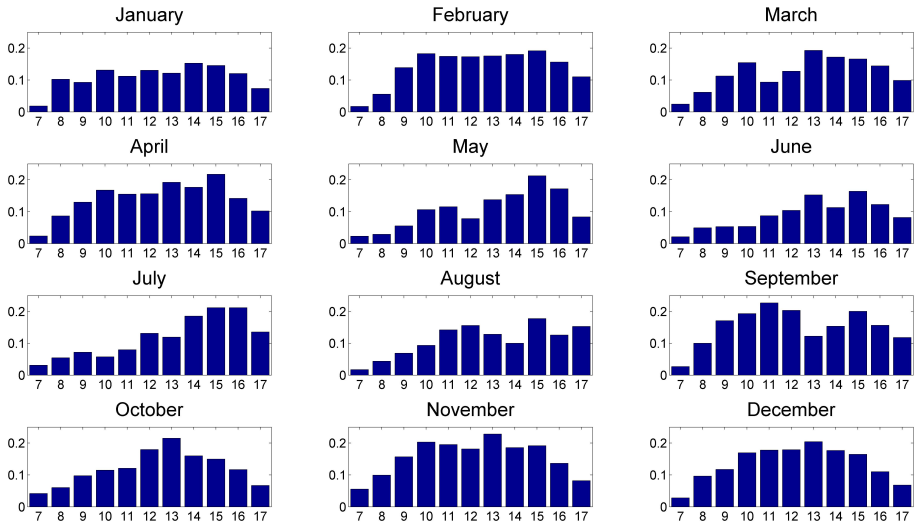

Figure A.24: Hourly RMS error for daylight hours over each month for annual optimization of EQ. 3.6

A.1.5 CC and RH Annual Optimization for Power Correlation

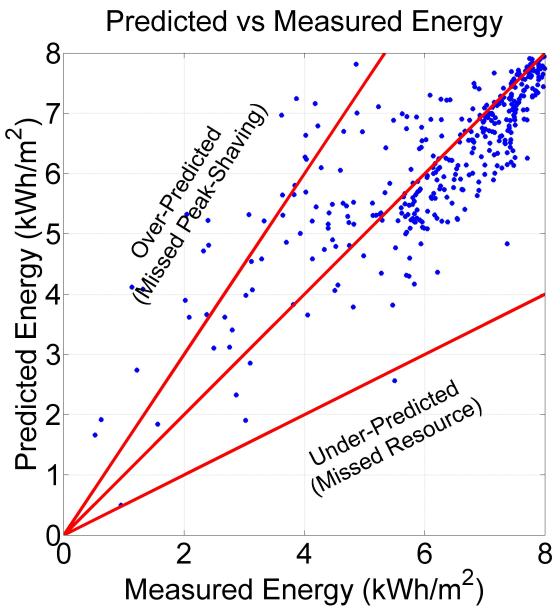

Figure A.25: Measured vs. predicted daily insolation scattergram for annual optimization of EQ. 3.8

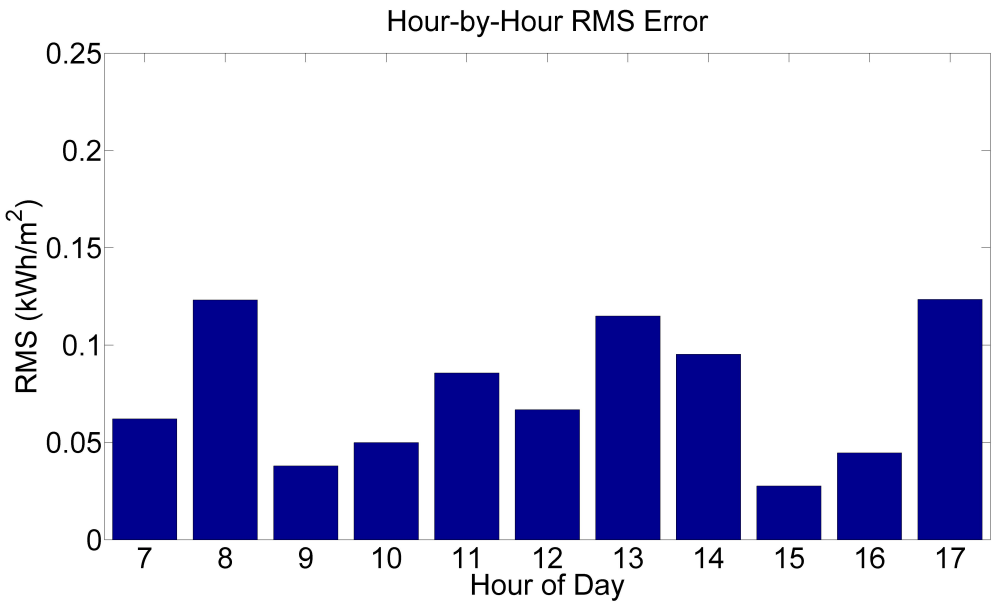

Figure A.26: Hourly RMS error for daylight hours over entire year for annual optimization of EQ. 3.8

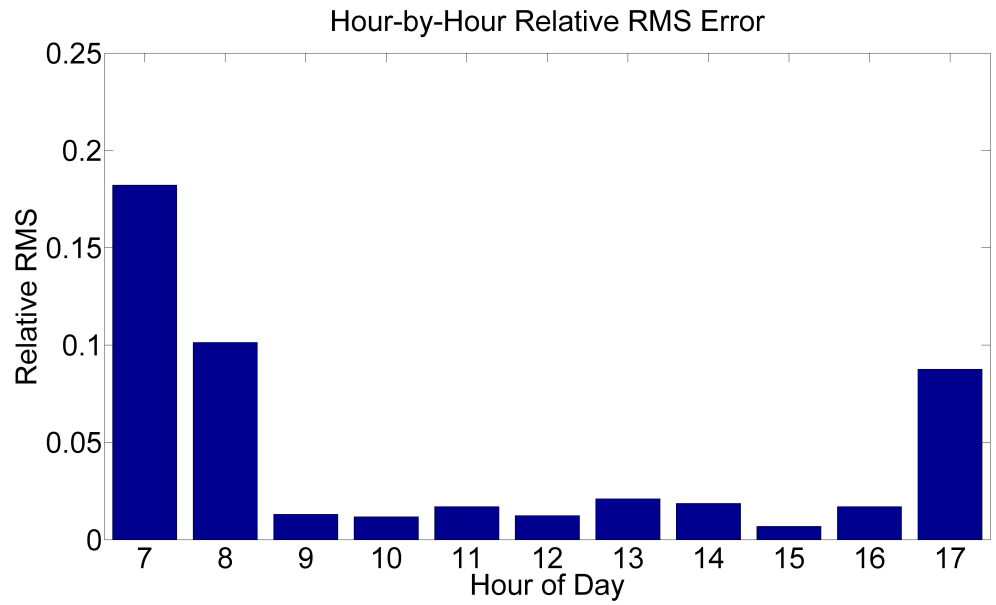

Figure A.27: Hourly relative RMS error for daylight hours over entire year for annual optimization of EQ. 3.8

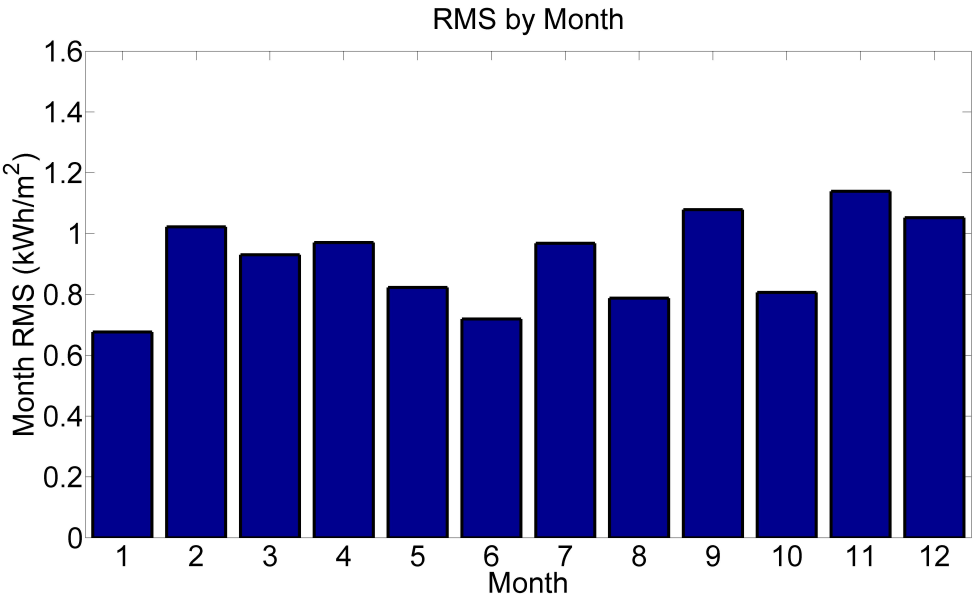

Figure A.28: Daily RMS error during each month for annual optimization of EQ. 3.8

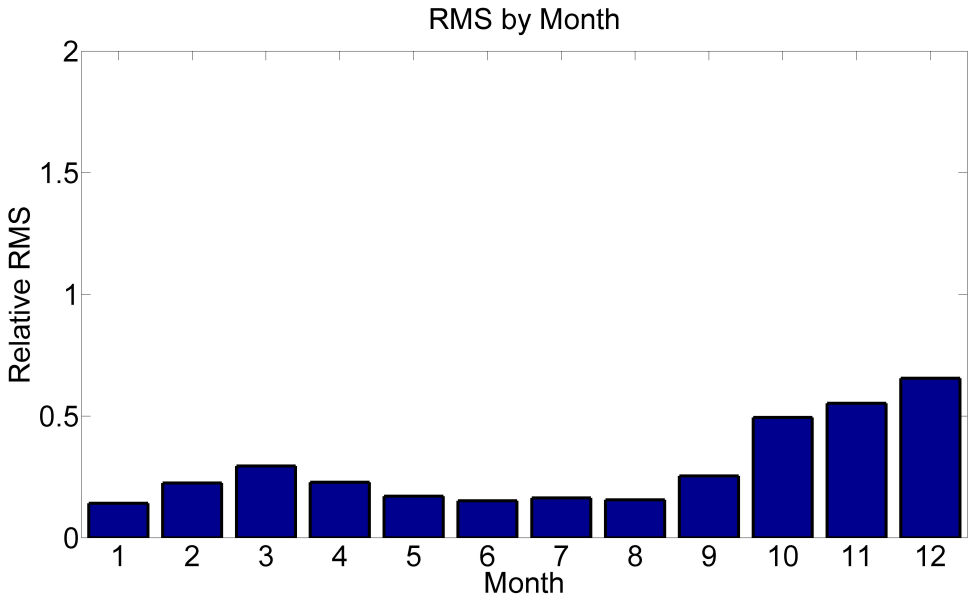

Figure A.29: Daily relative RMS error during each month for annual optimization of EQ. 3.8

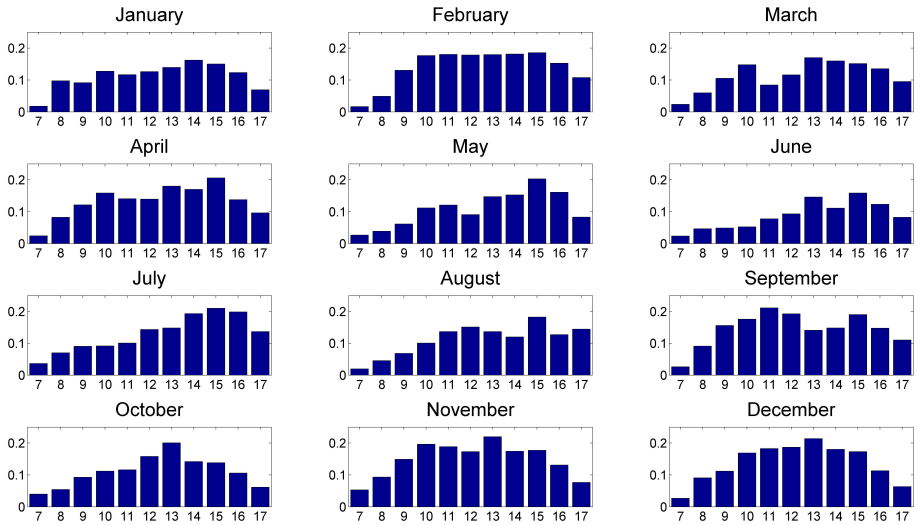

Figure A.30: Hourly RMS error for daylight hours over each month for annual optimization of EQ. 3.8

A.1.6 CC and RH Monthly Optimization for Linear Correlation

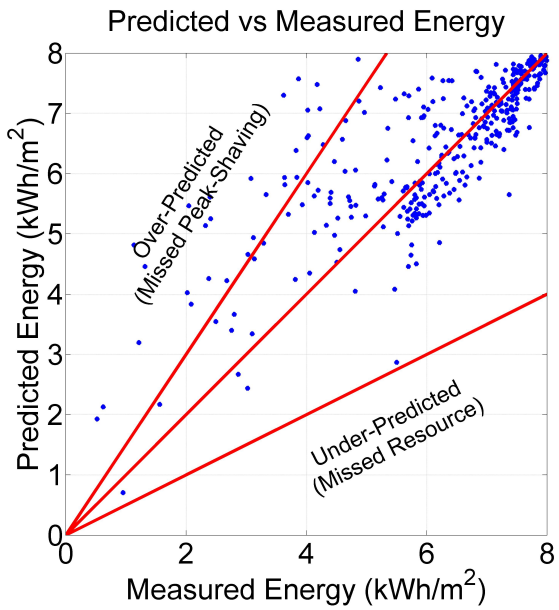

Figure A.31: Measured vs. predicted daily insolation scattergram for monthly optimization of EQ. 3.6

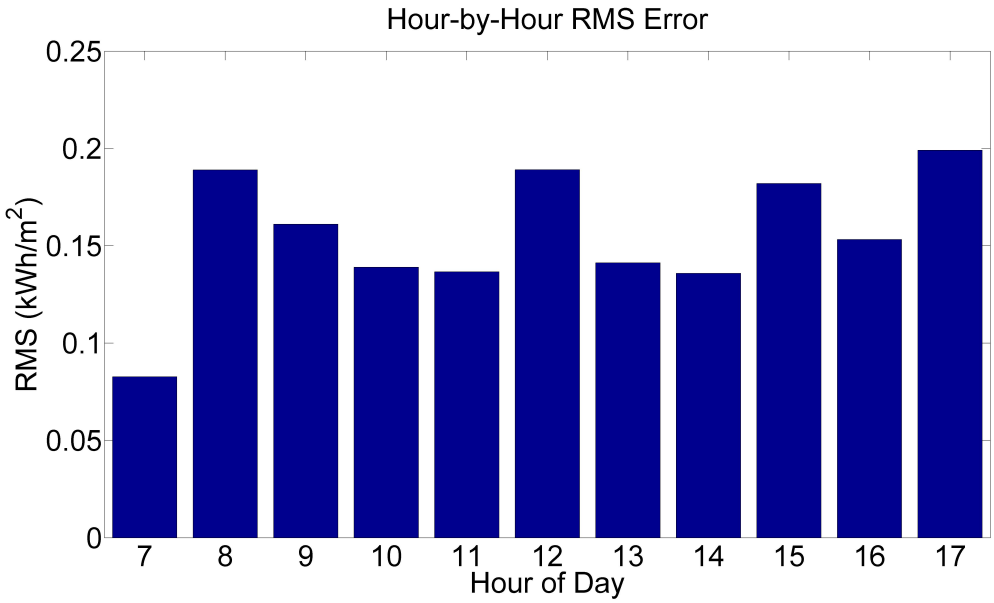

Figure A.32: Hourly RMS error for daylight hours over entire year for monthly optimization of EQ. 3.6

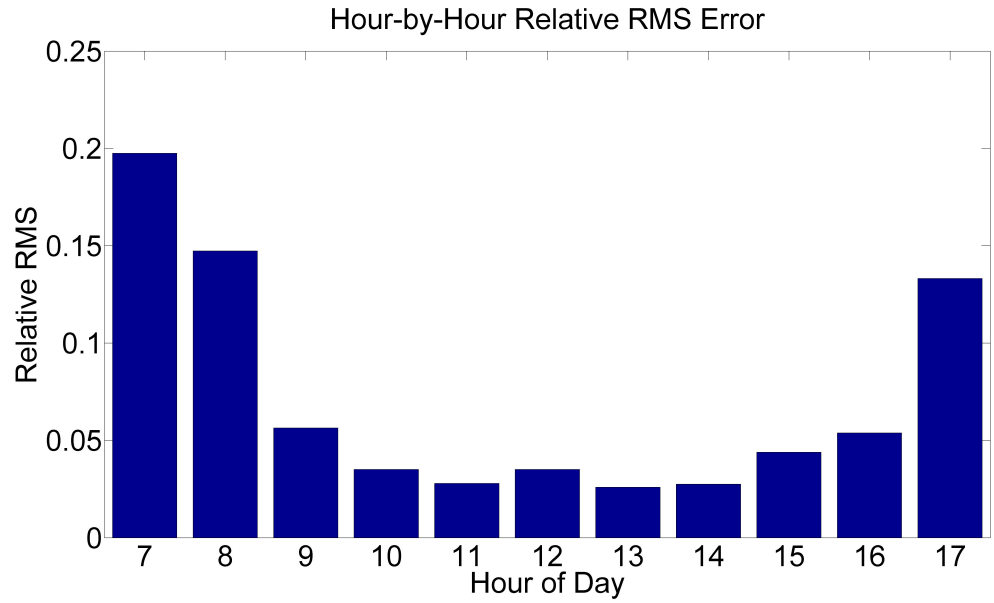

Figure A.33: Hourly relative RMS error for daylight hours over entire year for monthly optimization of EQ. 3.6

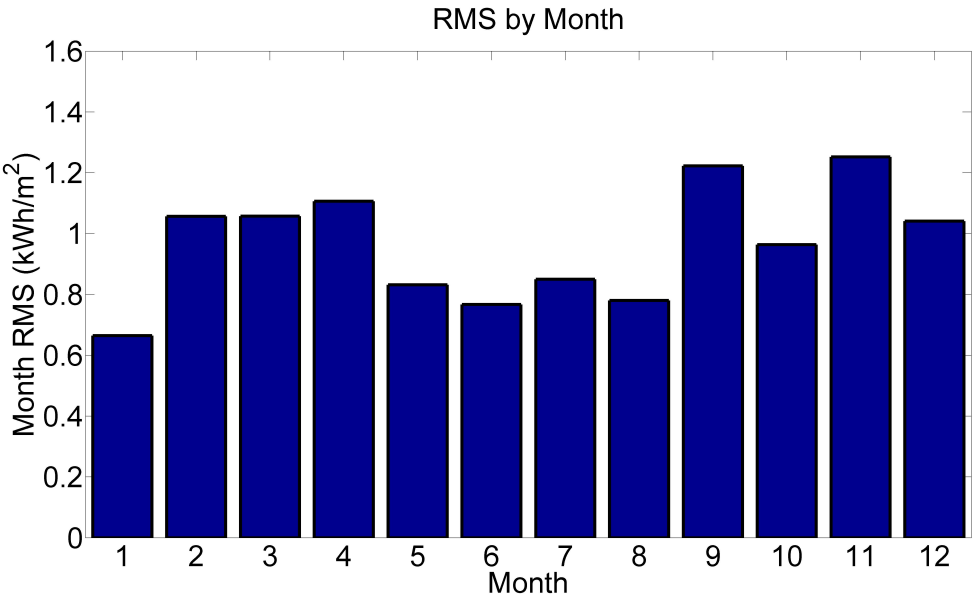

Figure A.34: Daily RMS error during each month for monthly optimization of EQ. 3.6

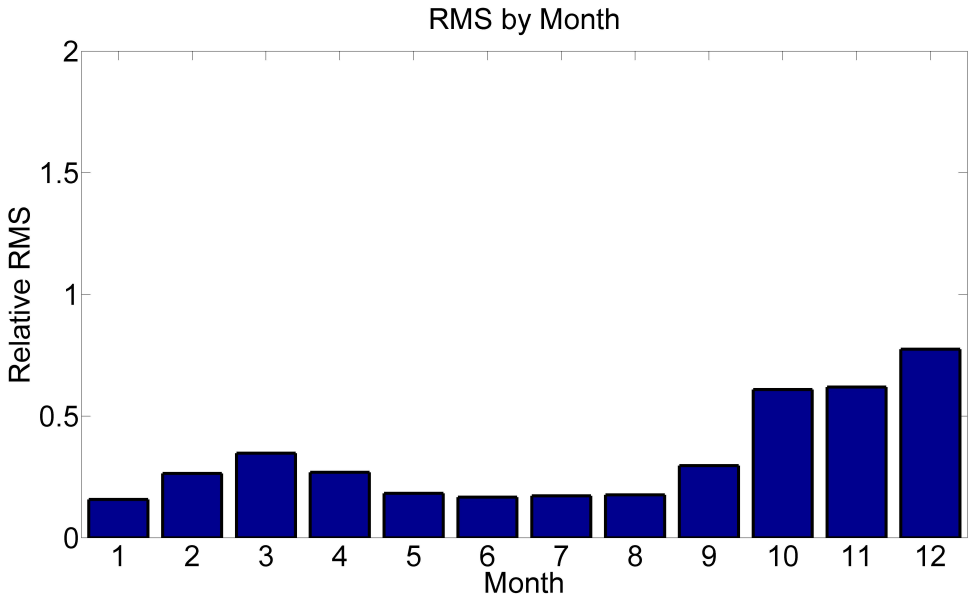

Figure A.35: Daily relative RMS error during each month for monthly optimization of EQ. 3.6

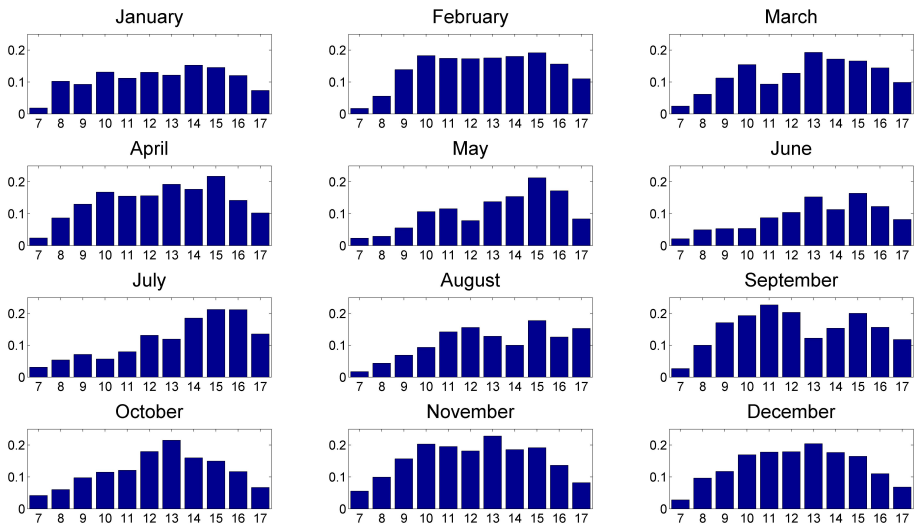

Figure A.36: Hourly RMS error for daylight hours over each month for monthly optimization of EQ. 3.6